The Development of Self-interference of Split HOLZ (SIS-HOLZ) lines for Measuring z-dependent Atomic Displacement in Crystals

by

Mana Norouzpour

M.Sc., Science and Research University of Tehran, 2007

B.Sc., University of Tehran, 2004

A Dissertation Submitted in Partial Fulfillment

of the Requirements for the Degree of

DOCTOR OF PHILOSOPHY

in the Department of Mechanical Engineering

University of Victoria

The Development of Self-interference of Split HOLZ (SIS-HOLZ) line for Measuring z-dependent Atomic Displacement in Crystals

by

Mana Norouzpour

M.Sc., Science and Research University of Tehran, 2007

B.Sc., University of Tehran, 2004

Supervisory Committee

Dr. Rodney Herring, Supervisor
(Department of Mechanical Engineering)

Mr. Brian Lent, Departmental Member
(Department of Mechanical Engineering)

Dr. Thomas Tiedje, Outside Member
(Department of Electrical and Computer Engineering)

Dr. Matthew G. Moffitt, Outside Member
(Department of Chemistry)

Abstract

Measuring atomic displacement inside crystals has been an important field of interest for decades especially in semiconductor industry for its effect on the crystal structure and symmetry, subsequently on the bandgap structure. There are three different image based, diffraction based, and electron holography based techniques using transmission electron microscope (TEM). These methods enable measuring atomic displacement inside specimen. However, among all TEM techniques offering nano-scale resolution measurements, convergent beam electron diffraction (CBED) patterns show the highest sensitivity to the atomic displacement. Higher order Laue zone (HOLZ) lines split by small variations of lattice constant allowing the atomic displacement measurement through the crystal. However it is a cumbersome measurement and it can only reveal the atomic displacement in two dimensions. Therefore, the atomic displacement information at each depth through the specimen thickness is still missing. This information can be obtained by recovering the phase information across the split HOLZ line. The phase profile across the split HOLZ line can be retrieved by the electron interferometry method. The phase of the diffracted beam is the required information to reconstruct the atomic displacement profile through the specimen thickness.

In this work, we first propose a novel technique of self-interference of split HOLZ line based on the diffracted beam interferometry which recovers the phase information across the split HOLZ line. The experimental details of the technique have been examined to report the parameters in order to implement the method. Regarding the novelty of the technique and the lack of the of a reference phase profile to discuss the results, phase profile simulation was a main contribution. For simulating the phase profile across the split HOLZ line the Howie-Whelan formula supporting the kinematical theory of diffraction is used. Accordingly, the analytical approach to simulate the phase profiles across the split HOLZ line for three various suggested atomic displacements are studied. Also, the effect of some parameters such as the atomic displacement amplitude, the specimen thickness, and the **g** reflection is investigated on the phase profile. This study leads to an equation used for fitting the experimental results with the simulated phase profile.

Consequently, self-interference of split HOLZ line (SIS-HOLZ) is studied as a method of reconstructing the phase profile across the split HOLZ line which carries the information of atomic displacement through the specimen thickness.

Honors and Awards

This work has been the winner of two awards:

1- The student poster award in the physical science session of the electron microscopy annual conference, Microscopy and Microanalysis (M&M) 2015, Portland- Oregon- USA.

2- The student poster award in the Pacific Centre for Advanced Materials and Microstructures (PCAMM) 2016, UBC- Vancouver-Canada.

Table of Contents

List of Tables

List of Figures

Acronyms

BF	Bright Field
BFP	Back Focal Plane
CBED	Convergent Beam Electron Diffraction
CCD	Charge Coupled Device
DBI	Diffracted Beam Interferometry
DF	Dark Field
DFEH	Dark Field Electron Holography
EELS	Electron Energy Loss Spectroscopy
EH	Electron Holography
EST	Equal Slope Tomography
ET	Electron Tomography
FEM	Finite Element Method
FIB	Focused Ion Beam
FOLZ	First Order Laue Zone
FT	Fourier Transform
HOLZ	Higher Order Laue Zone
HRTEM	High Resolution Transmission Electron Microscope
LED	Light Emitting Diode
MBE	Molecular Beam Epitaxy
NBD/NBED	Nano Beam Electron Diffraction
SAD	Selected Area Diffraction

SEM	Scanning Electron Microscope
SOLZ	Second Order Laue Zone
STEHM	Scanning Transmission Electron Holography Microscope
ROI	Region Of Interest
TEM	Transmission Electron Microscope
ZA	Zone Axis

Dedication

This thesis is lovingly dedicated to the memory of my father, Faramarz. Baba I miss you every day, but I am glad I made your dream come true.

To my mom, Minoo, for her encouragement, prayers and constant love have sustained me throughout my life. Maman, thanks for tying up many important loose ends while I was thousands miles away doing my PhD.

To Ramtin ♥, for his sincere love and devotion through my ups and downs. Ramtin, over these years you have helped me find my way and get to the point. I know 2016 was a sad tough year for you but you did not withhold your support.

Acknowledgments

It is my pleasure to appreciate my supervisor Dr. Rodney Herring for the support, guidance and insightful comments he has provided throughout my PhD. It was a privilege and an honor for me to share of his exceptional scientific knowledge and his extraordinary humanities.

I also wish to extend my thanks to UVic's Advanced Microscopy Facility (AMF) members. Dr. Elaine Humphry, AMF lab manager, and Dr. Arthur Blackburn, AMF lab research scientist, thanks for your precious role in conducting my experimental work.

I am truly grateful to Dr. Ramtin Rakhsha for his valuable suggestions and help, mostly through Chapter 3.

I would like to make a special reference to Dr. Giulio Pozzi, for his time and excellent guidance answering my questions promptly from Italy.

Many thanks to our research group members, especially Mr. Brian Lent for sharing his extensive knowledge with us and bringing fruitful discussions to our group meetings.

Friends usually come the last in the acknowledgment list, although their support always has a huge impact on one's success. I wish to thank Karolina and Armita and people whose names are not mentioned here but this does not mean that I have forgotten their support.

Chapter 1

Introduction

Strain has been an interesting topic in semiconductor research since 1950s. In semiconductors strain originates from phonon-induced lattice vibrations, lattice mismatched film growth, and applied external stress. Strain is either beneficial or detrimental to the semiconductor operation. Strain has unfavourable effects on the lifetime of the devices. It can also increase the mobility of the charge carriers by the band gap reduction. Reference [1] has widely explained the effect of strain on the band structure in semiconductors. Based on the deformation potential theory developed by Bardeen and Shockley [2], the strain-induced band edge shift is proportional to the strain tensor, $\Delta E = \sum_{ij} \Xi_{ij} e_{ij}$, where e_{ij} is the strain tensor and Ξ_{ij} are deformation potentials. Deformation potential theory is the primary method of modeling the strained semiconductor and has proved to be successful in explaining experimentally observed changes in strained device behavior. Strain changes the relative positions of atoms in the crystals resulting the spatial interaction between atoms being affected. The potential energy in Hamiltonian of the system depends strongly on the configuration of the system which will be affected by the symmetry of crystal. Advantageous strain reduces crystal symmetry. Additionally the bandgap energy is inversely related to the lattice constant and strain is defined as the percentage change of material's lattice constant [3]. Therefore, due to the large influence of strain on the physical properties, the electronic structure of materials and functionality of the devices, the accurate and precise measurement of strain in semiconductors is an active field of research since the semiconductor technology was established. As a result of the continuous reduction of feature sizes in semiconductor devices, it becomes more valuable to measure strain at the nanometer scale in which the reliability can be achieved with a high spatial resolution [4, 5, 6]. X-ray diffraction and Raman spectroscopy are two common techniques which offer high precision in strain measurement but they offer limited spatial resolution ($\simeq 500$ nm). This makes them unsuitable for characterizing the next generation of nano-scaled devices. Presently, the only tool capable of measuring strain at the nanometer scale with the spatial resolution below 5 nm is Transmission Electron Microscopy (TEM). Generally, TEM techniques to measure strain inside semiconductors are categorized into three main types as follows;

- Image based techniques including HRTEM (High Resolution Transmission Electron Microscopy).

- Diffraction based techniques including NBD/NBED (Nano Beam Electron Diffraction) and CBED (Convergent Beam Electron Diffraction).
- Electron Holography (EH) including DFEH (Dark Field Electron Holography).

In Table 1, all TEM strain measurement techniques are compared in terms of spatial resolution, precision and some of their features such as providing a two-dimensional (2D) measurement.

All techniques in Table 1 provide 2D information of atomic displacement, however DFEH and CBED show the highest strain sensitivity with reasonable spatial resolution. In the obtained information using these techniques, there is one missing dimension unmeasured, which is the atomic displacement through the thickness of the specimen along the beam direction. This direction is parallel with the optical axis typically considered as the *z*-axis.

Recently, a TEM technique of electron tomography (ET) has been reported to determine the 3D coordinates of thousands of individual atoms and their displacement with high resolution of 1 nm^3 and precision of $\sim$19 pm. Equal slope tomography (EST) has allowed measuring the precise 3D atomic coordination of 3,767 atoms involved in 9 atomic layers of a tungsten needle sample [7]. Goris et al. performed electron tomography to determine 3D atomic position and displacement of 90,000 individual atoms in a pentagol bipyramid of Au nano particle [8]. This method needs a tilt series of a significant number of projections to reconstruct the raw data which provides an estimate of the intensity distribution inside the sample. However, the later filtering and denoising steps, analysis and refining the data need heavy mathematics and simulation methods to determine the atomic position and displacement with respect to an ideal model. Besides, the method is quite sensitive to the dynamical scattering which requires multiple scattering corrections, same as other TEM techniques mentioned in Table 1. This method can be categorized in the image based techniques, so an aberration corrected TEM is an obligation to have a high resolution measurement. Looking at the spatial resolution and the precision of the techniques, the best candidates for strain measurement at the nano-scale are the CBED and DFEH methods. CBED diffraction patterns comprise of elastically Bragg diffracted electrons from the high index lattice atomic planes called higher order Laue zone (HOLZ) lines.

Table 1- TEM techniques compared in terms of features important for the current work **[9, 1, 10, 11, 12, 13, 14, 15, 16, 17]**

	Spatial Resolution (nm)	Sensitivity	Features
HRTEM	2-4	1×10^{-3}	1. Shows poor image quality at the interfaces. 2. Shows sensitive image contrast to the specimen thickness, composition variation, and surface contamination. 3. Provides 2D maps of strain across a $150 \times 150\ \mathrm{nm}^2$ field of view rather than the isolated points. 4. Requires a uniform specimen thickness ≤ 50 nm. 5. Requires a reference region which is not strained. 6. Requires simulations. 7. Requires aberration correctors.
NBED	2-10	1×10^{-3}	1. Requires less than 10 μm condenser apertures (convergent angle is below 1 mrad). 2. Precision fluctuates significantly in different regions of the sample. 3. Requires high acquisition time. 4. Requires energy filtering for the specimens thicker than 150 nm. 5. Requires simulation.
CBED	1-3	1×10^{-4}	1. Requires heavy calculations. 2. Provides 2D maps of strain across a $500 \times 500\ \mathrm{nm}^2$ field of view. 3. Requires energy filtering for the specimens thicker than 600 nm. 4. The convergent angle range is 5-20 mrad. 5. Requires simulation.
DFEH	4-6	2.5×10^{-4}	1. Provides 2D maps of strain across a large field of view, $1 \times 2.5\ \mu\mathrm{m}^2$. 2. Requires an electron biprism and a Lorentz lens. 3. Requires a specimen with a uniform thickness, composition and a large defect free area in the specimen a reference. 4. Requires simulation.
ET/EST	1 (nm^3)	$\sim 10^{-3}$	1. Provides 3D atomic position information. 2. Needs an electron tomography holder, 180^{o} tilt. 3. Requires heavy mathematics, refinement, simulation, and multiple scattering corrections. 4. Requires aberration correctors. 5. Est requires precise equal slope tilts

Since the HOLZ lines come from the crystalline planes with very large Bragg angles, they are very sensitive to the atomic displacement. The atomic displacements appear as the position change, broadening or splitting of the diffraction patterns. The most promising diffraction pattern to give the accurate information of the strain field is HOLZ line, which measures the strain as small as 0.01 % when compared to the HOLZ lines of an unstrained crystal. HOLZ line formation on the diffraction plane can be comprehensively described by the Bragg law explained in Chapter 2.

Many approaches are used to measure the atomic displacements using HOLZ lines. In the uniform strained region of the crystal the HOLZ line shifts in the CBED bright disk while in the non-uniform strained regions they split into two high intensity peaks and some lower intensity internal fringes. The shift or the split width of the HOLZ line is directly related to the atomic displacement in the specimen [18]. In the diffraction based techniques such as CBED, the intensity images of the diffracted beam are used to determine the strain. Generally in the diffraction based techniques, the intensity distribution in the diffraction pattern is compared in both strained and unstrained regions of the specimen to determine the average atomic displacement. The intensity of the diffracted beam is influenced by many parameters such as dynamical diffraction where the beam diffracts multiple times by the crystal's lattice planes that interfere with the strain measurement, or by the effective accelerating voltage.

The strain information is contained in the phase of the diffracted beam, which is lost by recording the beam with detectors such as a charge coupled device (CCD) camera. Among TEM techniques, EH is a method that can recover the phase information of the beam. EH is invented by Dennis Gabor in 1948, however it has been introduced into the strain measurement field only in the last decade. DFEH is an EH technique which reconstructs the phase information by interfering a diffracted wave from a non-strained region of the crystal, a reference beam, with the diffracted wave from a strained region of the specimen or a region of interest (ROI), an object wave. The retrieved phase difference between the diffracted beams is directly related to the atomic displacement. Both CBED and DFEH have their challenges presented in the next section.

1.1 Challenges

Although CBED and DFEH show the highest spatial resolution and strain sensitivity among all TEM techniques, there are challenges in their experimental procedure and interpreting the results.

DFEH objections are briefly presented as follows.

- *Specimen fabrication*: The reconstructed phase information is very sensitive to the specimen thickness variation and the compositional change. So, DFEH needs a uniform specimen in terms of thickness and composition in both reference region and ROI.
- *TEM equipment*: One main advantage of DFEH over the other techniques is its large field of view, however for this purpose the microscope needs to be equipped with a Lorentz lens, which is rare for TEMs.
- *2D strain map*: DFEH gives the 2D strain maps and the third dimension along the specimen thickness is still missing.

The challenges with the CBED technique are as follows;

- *Phase loss:* The atomic displacement information is in the phase of the beam which is lost when the diffraction intensity is recorded.
- *Heavy calculations:* The reported techniques in Table 1 require simulation however, the CBED technique calculations are cumbersome especially in thick specimens when the dynamical diffraction (multiple scattering) effect is taken into account.
- *2D strain information:* The planar atomic displacement is measured as the average value of the atomic displacements through the thickness of the crystal. The displacement profile through the thickness of the specimen is unknown.

Accordingly, the common missing information in both DFEH and CBED is the third dimension of the atomic displacement through the specimen thickness. This information is necessary for a 3D strain measurement or determining the full tensor of strain, e_{ij}. Recovering the third dimension of strain has been always a challenge in electron microscopy techniques. It exists in the phase of the diffracted beam from a strained crystal. Since HOLZ lines are the most sensitive diffraction patterns to the atomic

displacement, they are the best candidate among the diffraction patterns. The split HOLZ line with its internal intensities carry the displacement profile information through the thickness of the crystal, however this information is lost in the CBED technique. Several attempts have been done to simulate the z-dependent displacement profile using the recovered phase information via DFEH, although it has not been convincingly achieved. Thus, there was no experimental method to directly measure the z-dependent displacement profile in the phase of the diffracted beam. The main motivation of this work is to develop a technique to measure the z-dependent atomic displacement profile by recovering the phase profile across the split HOLZ line.

1.2 Objectives

The goal of this research is to establish a new TEM technique which gives the atomic displacement profile along the z-axis of a crystal specimen by recovering the phase information from the split HOLZ line. The development of the experimental details, the analytical, and the parameter sensitivity of the method (SIS-HOLZ) have been pursued successfully accomplishing this goal.

1.3 Contributions

The contributions of this thesis are twofold:

- *A mathematical routine to simulate the phase profile*: As it is mentioned in sections 1.1 and 1.2 the focus of this research is to seek for a novel technique to retrieve the phase information inside the split HOLZ line. The phase change carries the z-dependent displacement profile. Regarding Table **1**, all TEM techniques require simulation to fit with the experimental results. The analytical approach to achieve the phase profile for three z-dependent atomic displacement profiles is presented in Chapter 3.
- *The development of the experimental details*: In order to establish the method the experimental procedure and considerations, the sample preparation requirements and details are investigated. This is presented in Chapter 3 and Chapter 4.

1.4 Outline

A literature review of the relevant works is presented in Chapter 2. One of the major difficulties in the work was interpreting the data due to the lack of references. The phase profile across the split HOLZ line has been never retrieved. So, a method for calculating and simulating the phase profile across the split HOLZ line is developed. In Chapter 3 the theoretical details of the analytical approach to plot the phase change for some suggested displacement profiles are presented. The experimental procedure, the results, and evaluating the experimental data using the analytical procedure are reported in Chapter 4. Finally, the conclusion and the future work are presented in Chapter 5.

Chapter 2

TEM Techniques to Measure the Atomic Displacement – Literature Review

The diffraction based techniques rely on interpreting the intensity of the diffracted beam. First, a review on the diffraction intensity used to characterize the imperfections in crystals is presented in the following section.

2.1 Diffraction Intensity

One of the main common steps in all diffraction based techniques is calculating the intensity of the diffracted beam, for instance at point "p" in Fig. 1.

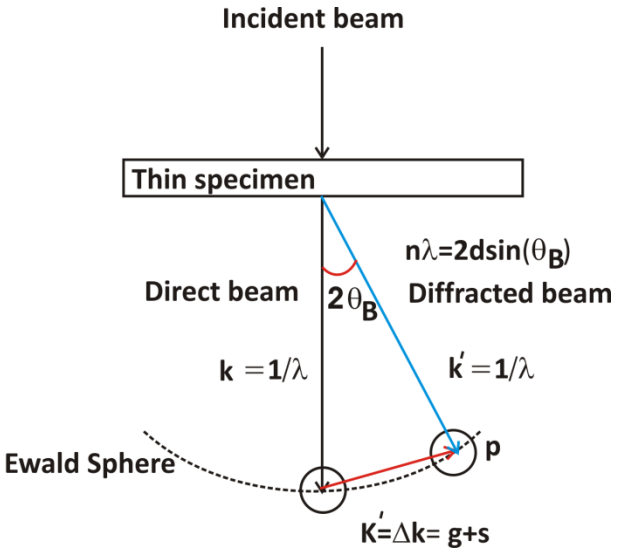

Fig. 1- The incident beam is diffracted by the specimen. It intersects the Ewald's sphere (appendix A. I) at point p. **k** is the transmitted wave vector, **k'** is the diffracted beam wave vector and **K'** is the diffraction vector or the reciprocal lattice vector **[19, 20]**. n is an integer showing the order of diffraction, **λ** is the electron wavelength, **d** is the interplanar atomic spacing and $\boldsymbol{\theta_B}$ is the angle of Bragg.

The incident beam undergoes transmission directly through the specimen and diffraction at an angle, θ_B, given by its wave vector, **k'**. The amplitude of the transmitted beam and the diffracted beam are constantly changing by multiple scattering from the atomic planes. In dynamical diffraction event both transmitted and diffracted beams transfer to each other's amplitude as they pass through the crystal (appendix A. II).

Hirsch et al. [20] suggested a pair of equations to calculate the intensity of the transmitted and the diffracted beams at the exit surface of the specimen. Instead of considering the condition of multiple beams involved in dynamical diffraction, they give the amplitude of just two beams, a diffracted beam and the transmitted beam. This is called the kinematical theory of diffraction. The derived equations are referred to as the Howie-Whelan equations, which are often the basis of interpreting the diffraction patterns of imperfect crystals. Since the focus of this work is only on the diffracted beam, the Howie-Whelan equation of the diffracted beam is presented.

The diffraction maxima happens when $\Delta K = g$ which is the exact Bragg diffraction orientation. However, there is always some deviation from the exact Bragg angle happening over a range of angles, $\Delta\theta_B$. The deviation from the exact Bragg angle creates a Gaussian distribution of intensity rather than sharp spots or lines in the diffraction patterns, Fig. 2 . Suppose $\Delta K = g + s$, where vector "**s**" represents the deviation from the reciprocal lattice point and is called the excitation error or the deviation parameter. The complex amplitude of diffraction by a non-distorted crystal is then [19, 20, 21];

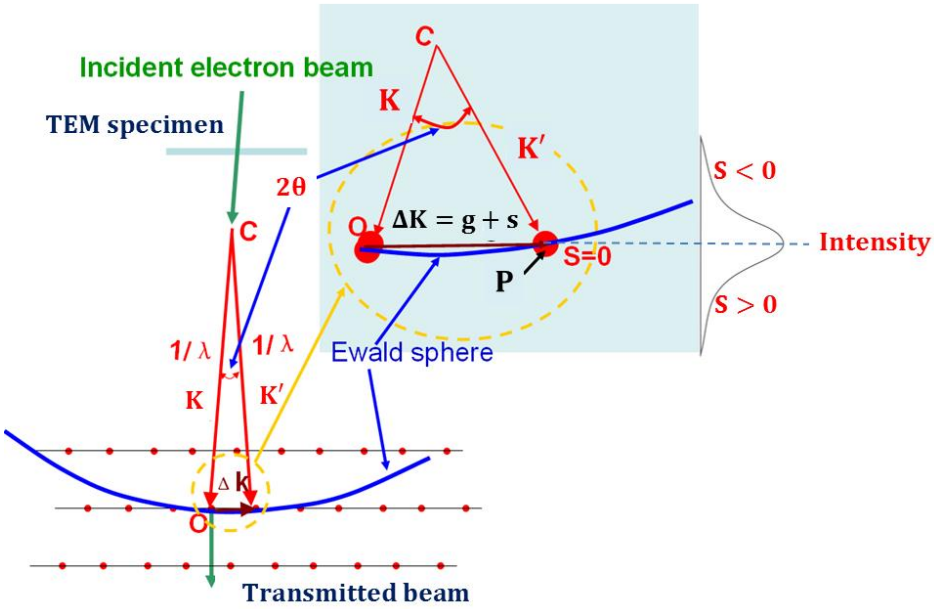

Fig. 2- Depending on the intersection of Ewald sphere with the reciprocal lattice point (relrod) the deviation parameter, s, can be zero (exact Bragg condition) or non- zero.

$$\Phi_g = \Sigma_n F_g \exp(-2\pi i(\mathbf{g}+\mathbf{s}).\mathbf{r_n}) \quad (1)$$

where F_g is the structure factor (appendix A. III) for the g reflection, and $\mathbf{r}_n$ is the position of the n^{th} lattice point. Since "**s**" is small, the phase changes gradually from the exact Bragg and the summation can be represented by an integral. For a non-distorted crystal, Eq. 1 can be rearranged into Eq. 2,

$$\Phi_g = \frac{F_g}{V_g}\int_{crystal} \exp(-2\pi i\mathbf{s}.\mathbf{r})dr \quad (2)$$

where V_g is the volume of the unit cell. Eq. 2 represents the Fourier transform (FT) of the crystal. In the CBED patterns of a perfect crystal, the intensity of individual HOLZ lines is $I_g = \Phi_g\Phi_g^* = |\Phi_g|^2$, where * denotes the complex conjugate operation.

In the case of a distorted crystal, the position of n^{th} lattice point is $\mathbf{r_n'} = \mathbf{r}_n + \mathbf{R}_n$, where $\mathbf{R}_n$ is the displacement vector of the unit cell from its unstrained position. Therefore;

$$\Phi_g = \frac{F_g}{V_g}\int \exp\big(-2\pi i(\mathbf{g}+\mathbf{s}).(\mathbf{r_n}+\mathbf{R_n})\big)\,dr \quad (3)$$

Simplifying Eq. 3 gives the complex amplitude of the diffracted beam from a distorted crystal as;

$$\Phi_g = \frac{F_g}{V_g}\int \exp(-2\pi i\mathbf{g}.\mathbf{R_n})\exp(-2\pi i s r_n)dr \quad (4)$$

Comparing Eq. 4 and Eq. 2 shows that by introducing imperfections into the crystal, an extra phase factor of $\exp(-2\pi i\mathbf{g}.\mathbf{R_n})$ is added to the diffracted beam. We can further simplify Eq. 4 into;

$$\Phi_g = \frac{i\pi}{\xi_g}\int_0^t \exp(-2\pi i\mathbf{g}.\mathbf{R_n})\exp(-2\pi i s z)dz \quad (5)$$

In order to rearrange Eq. 4 to Eq. 5 some approximations are needed, i.e. **r** and **s** are both parallel to the beam direction, z. Hence, the components of s not parallel to z are ignored

and $|\mathbf{s}| = s_z$. In Eq. 5, ξ_g is the extinction distance, which is a characteristic length for the diffraction vector, **g**. Its magnitude is given by

$$\xi_g = \frac{\pi V_c \cos\theta_B}{\lambda F_g}. \quad (6)$$

The value of ξ_g is very important for the intensity calculation as it contributes to the contrast of the intensities within diffraction patterns. ξ_g's accurate value cannot be calculated using Eq. 6 since the structure factor is zero for specific g reflections. However in this work the theoretical value of ξ_g is used to calculate the thickness limit for considering the kinematical theory of diffraction. In the TEM techniques, the Howie-Whelan equation, Eq. 5, plays an important role to interpret the CBED patterns of a distorted crystal. In the following, the previous CBED works to measure the atomic displacement in crystals are presented. Additionally some attempts are done to simulate the z-dependent displacement profile using DFEH. This is reported after CBED fulfilled approaches.

2.2 Convergent Beam Electron Diffraction (CBED)

2.2.1 CBED Patterns

Unlike selected area diffraction (SAD) which uses a planar incident beam, CBED makes use of a convergent electron beam having a convergence angle of α (appendix A. IV). The beam can be considered as a number of parallel electron beams with a range of incident angle from $+\alpha_i$ to $-\alpha_i$ while i is an integer. In the CBED technique the area of diffraction from the specimen is chosen by focusing the probe on a very fine spot (≤ 50 nm) [22] on a region of interest (ROI), Fig. 3.

Generally in CBED, the beam on the specimen is a small spot of a few nanometers in diameter and the beam on the diffraction plane is a disk of a few milliradians, depending on the angle of convergence. The zero order disk shown in Fig. 3 is also called the transmitted disk or 000 CBED disk. The 000 CBED disk is intersected by HOLZ lines (Fig. 4 and Fig. 5), which can be used to map the orientation of the Bragg diffraction for a particular atomic plane. HOLZ lines come in pairs. The HOLZ line in the 000 CBED disk is deficient or dark as its intensity is diffracted into the diffracted beam

and the HOLZ line has excess intensity is bright, Fig. 5, in its diffracted disk. A schematic showing HOLZ line formation is shown in Fig. 4.

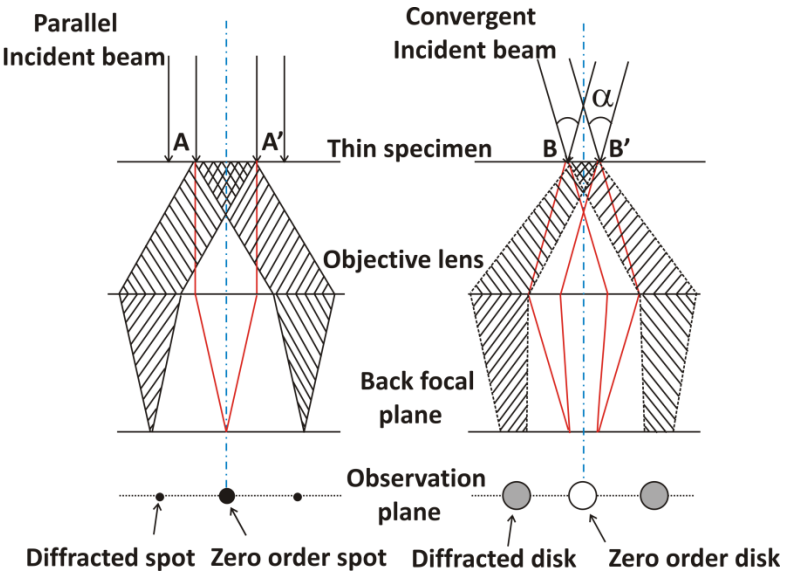

Fig. 3- The formation of a SAD and CBED patterns. In SAD, the **AA'** area is selected by an aperture in the first image plane of the objective lens. The planar beam produces a spot diffraction pattern on the back focal plane of the objective lens. In CBED, there is the convergent beam impinging the specimen having the area **BB'** determined by the probe size. This produces disks of diffraction related to the convergence angle, **α [19, 22]**.

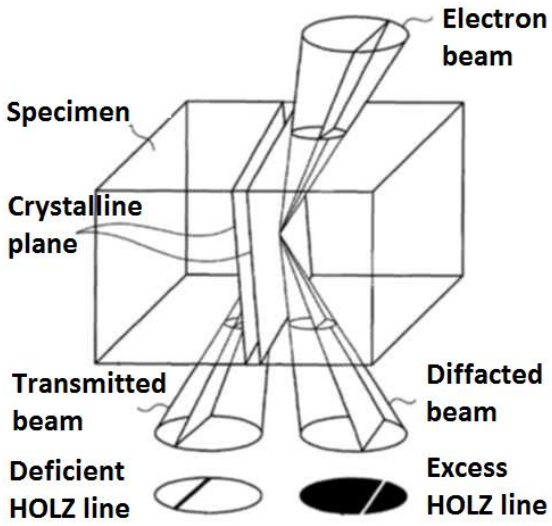

Fig. 4- The schematic of HOLZ line formation **[18]**.

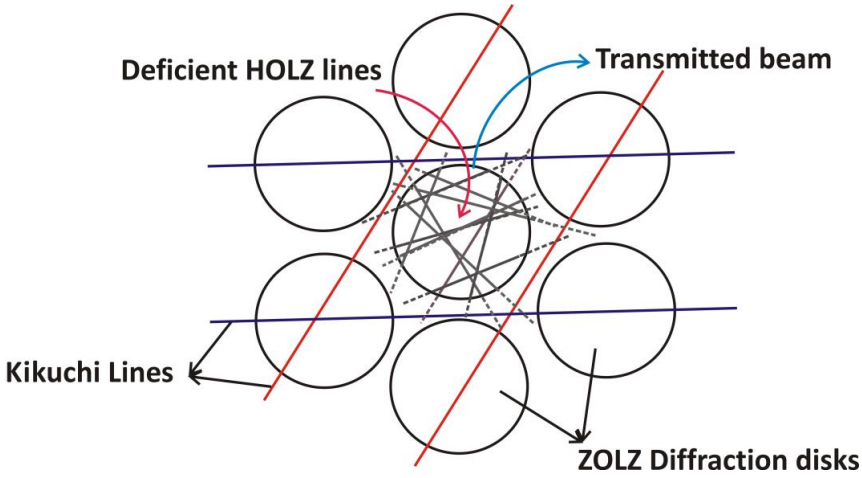

Fig. 5- The schematic of the deficient HOLZ lines intersected the 000 CBED disk **[19]**. Zero Order Laue Zone (ZOLZ) disks are shown around the 000 CBED disk.

The HOLZ lines are individual lines in the non-strained regions of the specimen. They come from the high index lattice planes having high Bragg angles, θ_B, that show a high sensitivity to any lattice plane bending. This is expressed in Eq. 7.

$$|\mathbf{g}| = \frac{1}{d}, \qquad |\Delta\mathbf{g}| = -\frac{\Delta d}{d^2}, \qquad \frac{\Delta d}{d} = -\frac{\Delta\theta_B}{\tan\theta_B} \tag{7}$$

For the smaller values of d, the value of $|\Delta\mathbf{g}|$ is larger for the same Δd. Also high angle diffracted beam decreases the absolute value of error, $|\Delta d/d|$, assuming the error of the Bragg angle, $\Delta\theta_B$, is the same for all reflections [19, 23]. In TEM techniques $\Delta d/d$ is commonly called the precision or the sensitivity of the measurement. Any uniform strain in the illuminated volume of the specimen will shift the HOLZ lines with respect to the center of the pattern (or the HOLZ line ideal position in 000 CBED disk). In non-uniform strained regions, the diffraction planes become curved causing the HOLZ line to split into an intensity band having a width. The band width depends on the size of the curvature and orientation of the electron beam with respect to the bent planes. Some HOLZ lines will not split as the bending axis is parallel to the path of the electron beam passing through the crystal specimen. This is conventionally called the invisible strain [24, 25, 26]. Fig. 6 shows a split HOLZ line created by the bent atomic planes of the specimen. When the beam impinges on the bent region of the specimen and the bending axis is not

parallel to the beam direction, the Bragg diffracted electrons intersect the Ewald's sphere on the diffraction plane over a range of positions instead of just one. So, the intensity band or a split is formed. The HOLZ line shift and split width have been usually used to study the 2D atomic displacements in crystals. In the following section a summary of the reported works is presented.

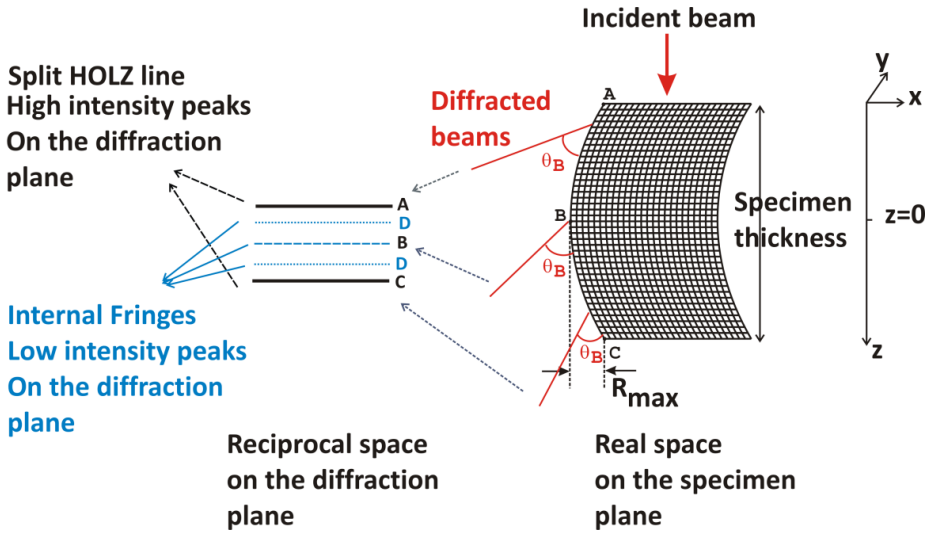

Fig. 6- A schematic of a hypothetical z-dependent strain profile of a bent crystal that Bragg diffracts the electron beam by the Bragg angle. $\mathbf{R_{max}}$ is the maximum atomic displacement. A and C are the main peaks B and D are the internal fringes **[27]**.

2.2.2 Atomic Displacement Measurement Using HOLZ lines

The strain effect on HOLZ lines was first used in 1980 to study the strain field around the dislocations and stacking faults [21]. The stacking faults lower the symmetry of HOLZ lines, split some reflections, and shift their position. The unsplit HOLZ lines are used as a reference to measure the stacking fault displacement vector, R. Dislocation, which produces non uniform strain fields, split the HOLZ reflections. The width of the HOLZ lines was used to measure the burger vector. Generally, a curvature about an axis parallel with the beam causes the HOLZ lines to bend whereas the curvature about an axis perpendicular to the beam direction splits the HOLZ line [24, 25]. The application of the CBED pattern to determine the lattice strain for the first time has been established in 1982 [28]. The angular position of the HOLZ lines is very sensitive to the lattice

parameter. Many researchers such as Rozeveld et al. [29], Deininger et al. [30], Wittmann et al. [31], Toda et al. [32], Karmer et al. [33], and Armigliato et al. [34, 35] used the HOLZ lines shift, their intersections shift or the ratio of the areas they form by comparing the experimental data with simulated patterns. Multiple CBED patterns are needed to determine the lattice parameters. This method is limited by the multiple scattering effects, the symmetry of the CBED pattern, the specimen thickness, the composition, the effective accelerating voltage and the image distortions. All mentioned factors effect on the HOLZ line position. Additionally, calculating HOLZ positions in the image using various algorithms introduced by different people, fitting them with the simulated HOLZ lines is time consuming and cumbersome. This is one of the main drawbacks of this technique. Besides, HOLZ lines are not straight lines at their intersections. Therefore, these regions need to be removed in calculating the HOLZ lines position using the experiments. Although many people followed the same routine to obtain the strain information out of the HOLZ line position variation, there were some differences in the implementation of the studies as follows.

- Using different simulation programs and routines to develop the precision of the technique.
- Applying the dynamical scattering correction on the kinematical simulation or neglecting the multiple scattering effects on the HOLZ line position.
- Detecting the HOLZ line position using computer-based algorithms.
- Developing TEMs to minimize the image distortions.
- Filtering the inelastically scattered electrons (late 80s) which enhances the contrast of the HOLZ lines. Poor contrast complicates their positional calculations.
- Studying different material systems.

As previously shown, the non-uniform strain field splits the HOLZ line. Some studies referred to the split of HOLZ line as a barrier hindering the measurement of the precise position of HOLZ line [36]. Vincent et al. [24] were first to simulate the intensity distribution across the split HOLZ line, referred to as rocking curve, from a strained

AgBrI particle. They used the kinematical theory of diffraction. They concluded that the split width of the HOLZ line depends on the maximum atomic displacement value,R_{max}, but insensitive to the atomic displacement distribution in the direction parallel to the beam or the z-axis, R(z). The interpretation of the split width, the HOLZ line bending, and quantifying the diffraction pattern have always been complicated since it required heavy calculations. Hence, many researchers maintained analysing the HOLZ line shift and not the split width to quantify the atomic displacement. In 2004, Clement et al. [37] used the split HOLZ line to study the surface relaxation in a 20 nm NiSi layer in a MOS (Metal oxide semiconductor) transistor structure. They compared the kinematical simulated rocking curves of the split HOLZ lines with a predicted model of strain. Chuvilin et al. [38] used the qualitative analysis of a split HOLZ line to show the evolution of the HOLZ line when moving from an unstrained to a non-uniform strained region showing that the split width increases. Although the Howie-Whelan integration for an imperfect crystal along the beam direction (z-axis) carries the z-dependent atomic displacement (Eq. 5), trying to quantify the z-dependent displacement field was cumbersome [38]. In 2006, Rouviere et al. [39] presented the first quantitative interpretation of the strain field using the split HOLZ lines at different distances from the interface of $Si/Si_{0.8}Ge_{0.2}$ which is followed by Benedetti et al. [40] and Houlellier et al. [41] for studying the heterogeneous strain field at the interfaces of epilayers. In order to use the split HOLZ line for strain quantification, there are common steps between all the implemented studies.

- Preparing a TEM cross section specimen.
- Modeling strain state using various tools and methods such as the finite element (FE) modeling. The output is the input of the next step.
- Using an accurate method of CBED simulation in order to simulate the CBED pattern in the strained regions of material.
- Optimizing the experimental condition to obtain the CBED pattern.
- Fitting the simulation and the experiment in order to measure the lattice constants.

Although some efforts have been done to interpret the split HOLZ lines, there were still some difficulties in data quantification. The kinematical simulation of the CBED pattern was done using the Howie-Whelan equation along the beam direction; however

the main difficulty was to fit the simulation with the experiment. Not only did the separation between the simulated main peaks not fit the experiment properly, but also the intensity distribution across the split differed significantly. Sharp experimental HOLZ lines, which fit the simulated HOLZ lines were only observed very far from the interface. Prior to Saitoh et al. [42] and Alfonso et al. [43], who comprehensively studied the effect of different displacement models on the fine fringes inside the split HOLZ line, the difference between the simulations and the experiments was justified as the lack of the dynamical diffraction correction in the CBED simulation.

Houdellier et al. [41] and Spessot et al. [44] developed a complex CBED simulation process which requires the structure factor and the exact experimental conditions such as the specimen thickness, the probe position, the effective accelerating voltage and the camera length to correct the dynamical interaction with HOLZ line. Correcting the dynamical effects in the CBED simulations resolved the difference for the separation of the intensity peaks seen at the top and bottom of the split, especially for the thick specimens. Although the fine intensity structure inside the split was still different between the simulations and experiments. Generally, the intensity distribution in a CBED pattern depends on many physical and geometrical parameters, which need to be taken into account when simulating the pattern. Even after all the modifications were taken into account in the simulations, the quantified data was still the projection of the atomic displacement change along the z axis on the xy plane and the z-dependent displacement distribution was still unknown.

The split HOLZ line with its subsidiary, low frequency fringes can be explained with optical Fraunhofer diffraction perspective. In 1988 Vincent et al. [24] showed this analogy by inserting a wedge shape prism and a concave prism separately in the object plane within their corresponding diffraction patterns. The prism resembled a rotated lattice plane or a bent lattice plane about an axis normal to the beam. As a result, the Fraunhofer pattern changed into a Fresnel type fringe system (appendix A. V). Almost two decades later, this interpretation was demonstrated analytically by Saitoh et al. [23], Alfonso et al. [43] and Spessot et al. [44]. Hence, the main component of the bending responsible for the split HOLZ line and its internal fine fringe structure is **R(**z**),** which is

the z-dependent atomic displacement. Therefore in Eq. 5, **g**·**R** can be replaced by **g**·**R(**z**)** [20, 24, 44]**.**

Finally, due to the CBED pattern simulation complications, researchers started thinking about reconstructing the phase information of the electron beam. Although the phase of the diffracted beam is not achievable from the intensity images of the diffraction patterns, it directly carries the strain information. EH is the only technique, which can recover the phase information of the beam. The only EH based method which has been found suitable to study the strain field in materials, is dark field electron holography (DFEH). This method is presented in the next section.

2.3 Phase Reconstruction Technique

The phase of the electron is sensitive to the electrostatic, magnetic and strain field, however it is lost by recording the electron beam. EH is a very powerful technique that can reconstruct the phase information in order to study the electrostatic, the magnetic and the strain field of the specimen. Before expressing the EH based method to study strain in materials, the required principles of EH are summarized in Section 2.3.1.

2.3.1 Electron Holography

EH is a unique technique which can reconstruct the complete image wave, including both amplitude and phase images. The first step in EH is recording an interference pattern/hologram (fringes) between a reference wave, Φ_{Ref}, and a wave coming from an object, $\Phi_{(\mathrm{ROI})}$. Then the intensity of the recorded pattern is $\mathrm{I} = |\Phi_{\mathrm{Ref}} + \Phi_{\mathrm{ROI}}|^2$.

In order to form an electron hologram, the primary requirement is a coherent source of electrons. Although the coherency in reality is never perfect, the degree of coherency must be enough to obtain an interference pattern with high contrast fringes. Then an electron biprism is required to interfere the beams and form a hologram on a CCD camera. An electron biprism is normally made from a quartz fibre which has been drawn in a hydrogen–oxygen flame to a diameter of 1 μm or less [45, 46]. The action of the biprism in forming the hologram is shown schematically in Fig. 7.

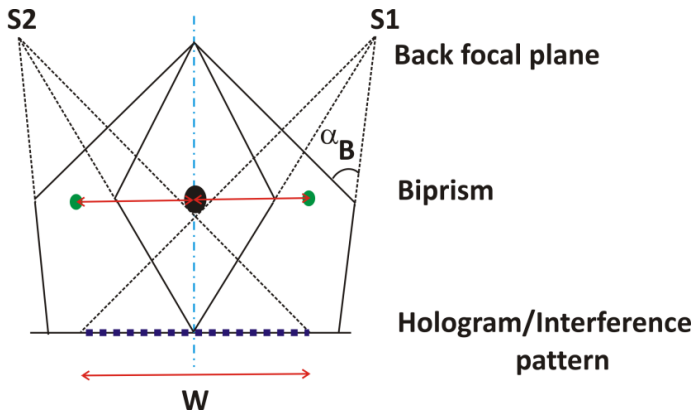

Fig. 7- A schematic diagram of forming a hologram. The biprism voltage controls the angle of deflection, $\boldsymbol{\alpha_B}$, subsequently the width of hologram, W. The spacing between the two sources S1 and S2 (interfering beams) is also a factor in determining the fringe spacing of the hologram **[45, 47]**.

The information in a CCD camera is recorded digitally. The second step is to reconstruct the phase image out of the hologram. To reconstruct the phase image digitally, the electron hologram is Fourier transformed (FT), using a FFT algorithm. The related mathematical equations are given in section 2.3.1.1. The FT of the hologram is composed of three terms, a center band and two side bands. The center band has no phase information while the side bands carry the same phase information. Therefore, the next step is to select one of the side bands with a proper filter and transfer it to the original space by the inverse FT. Now the phase and the amplitude images are obtained separately [45, 47].

In order to obtain the strain information using electron holography, instead of a reference beam passing through the vacuum and the object beam passing through an object, the interfered diffracted beams come from an unstrained region of the crystal specimen and the strained region. It is already discussed in deriving the Howie-Whelan equation that the diffracted beam of a strained crystal has an extra phase factor of $\exp(-2\pi \mathbf{g}.\mathbf{R})$ comparing with the diffracted beam from a perfect crystal. In the next section, it is briefly explained how DFEH is used to measure the atomic displacement.

2.3.1.1 Dark Field Electron Holography

DFEH is a recent method reported to measure the difference between the local **g**-vectors of the ROI, i.e., the strained, and the reference regions of the specimen [48]. Regarding Fig. 8, we choose a reference wave coming from the reference region of the specimen,Φ_{Ref}, and passes on the left side of the biprism and an object wave, Φ_{ROI}, coming from the strained region passes the right side of the biprism. By applying a positive voltage on the biprism the waves deflect towards each other and interfere. It should be noted that in DFEH by inserting an objective aperture on the back focal plane (BFP) of the objective lens, the direct 000 beam is blocked and only the diffracted beams can transmit to interfere. According to Fig. 8, the mathematical expression of the beams in the image plane is [48, 49, 50, 51, 47]

$$\Phi_{\mathrm{Ref}}(\mathbf{r}) = \mathrm{A}_{\mathrm{Ref}} \exp\big(\mathrm{i}(2\pi \mathbf{g}_{\mathrm{Ref}}.\ \mathbf{r} + 2\pi \mathbf{k_0}.\mathbf{r} + \phi_{\mathrm{Ref}})\big) \tag{8}$$

$$\Phi_{\mathrm{ROI}}(\mathbf{r}) = \mathrm{A}_{\mathrm{ROI}} \exp\big(\mathrm{i}(2\pi \mathbf{g}_{\mathrm{ROI}}.\mathbf{r} + 2\pi \mathbf{k_0}.\mathbf{r} + \phi_{\mathrm{ROI}})\big) \tag{9}$$

where $\mathbf{r}$ is the position vector in the image plane, $\mathbf{k_0}$ is the incident beam wave vector which is related to the electron beam wavelength, λ, by $|\mathbf{k_0}| = 1/\lambda$. $\mathrm{A_i}$ and ϕ_i are respectively the amplitude and the phase of the interfering diffracted beams, $\mathbf{g_i}$. By superposing the beams, the biprism adds respectively extra phase shifts of $2\pi \mathrm{i}\, \mathrm{k}_0 \alpha_\mathrm{B} \mathbf{r}.\mathbf{b}$ and $-2\pi \mathrm{i}\, \mathrm{k}_0 \alpha_\mathrm{B} \mathbf{r}.\mathbf{b}$ to the beams passing the right side and the left side of the biprism, where α_B is the deflection angle (Fig. 8) and $\mathbf{b}$ is the unit vector of the biprism perpendicular to the biprism axis. Therefore, the typical expression of the interference pattern intensity is

$$\begin{aligned} \mathrm{I}_{\mathrm{fringes}} &= (\Phi_{\mathrm{Ref}}(\mathbf{r}) \exp(2\pi \mathrm{i} 2\mathrm{k}_0 \alpha_\mathrm{B} \mathbf{b}.\mathbf{r}) \Phi^*{}_{\mathrm{ROI}}(\mathbf{r}) \exp(+2\pi \mathrm{i}\ 2\mathrm{k}_0 \alpha_\mathrm{B} \mathbf{b}.\mathbf{r})) \\ &\quad + \Phi_{\mathrm{ROI}}(\mathbf{r}) \exp(-2\pi \mathrm{i}\ 2\mathrm{k}_0 \alpha_\mathrm{B} \mathbf{b}.\mathbf{r}))\ (\Phi^*_{\mathrm{Ref}}(\mathbf{r}) \exp(-2\pi \mathrm{i}\ 2\mathrm{k}_0 \alpha_\mathrm{B} \mathbf{b}.\mathbf{r}) \\ &= \mathrm{A}^2_{\mathrm{Ref}} + \mathrm{A}^2_{\mathrm{ROI}} + 2\mathrm{V}\mathrm{A}_{\mathrm{Ref}}\mathrm{A}_{\mathrm{ROI}} \cos(2\pi\, (\mathbf{q_c} + \mathbf{\Delta g}).\mathbf{r} + \Delta\phi)) \end{aligned} \tag{10}$$

where $\mathbf{q_c} = 2\mathrm{k}_0 \alpha_\mathrm{B} \mathbf{b}$ is the spatial carrier frequency which defines two side bands in the Fourier space, $\mathbf{\Delta g} = \mathbf{g}_{\mathrm{Ref}} - \mathbf{g}_{\mathrm{ROI}}$,V is the contrast of the hologram fringes and

$\Delta\phi = \phi_{Ref} - \phi_{ROI}$. The fringe spacing, Δ, is inversely related to the carrier frequency, $\Delta = 1/q_C$. Therefore, by increasing the deflection angle,α_B, the carrier frequency increases and the fringe spacing decreases. The deflection angle is directly related to the biprism voltage. It can be said by increasing the biprism voltage, finer fringes can be obtained resulting in higher carrier frequency and higher lateral resolution.

The recovered phase associated with the carrier frequency in DFEH is $\phi = 2\pi\Delta\mathbf{g}.\mathbf{r} + \Delta\phi$. The term $\phi_g = 2\pi\Delta\mathbf{g}.\mathbf{r} = -2\pi\mathbf{g}.\mathbf{R}(r)$ is called the geometric phase directly related to the atomic displacement, $\mathbf{R}(r)$, and $\Delta\phi$ is the contribution of the electrostatic, magnetic and crystalline phase which need to be constant for both the reference and ROI regions. Since the phase is sensitive to the magnetic field and the electrostatic field, the compositional variation is not suitable in the ROI and the reference region. Furthermore, the reference region needs to be defect free and perfect and the specimen thickness needs to be uniform along both the ROI and the reference. Therefore, the reconstructed phase will be only dependent upon the strain field and other contributions in $\Delta\phi$ can be removed.

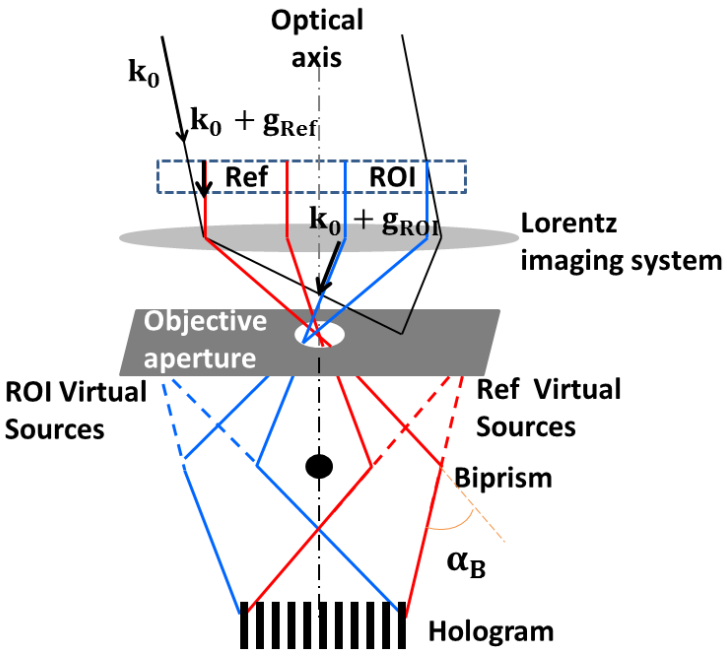

Fig. 8- The schematic of DFEH technique. $\mathbf{k_0}$ is the wave vector, $\mathbf{g_{Ref}}$ is the diffracted wave vector from a reference region and $\mathbf{g_{ROI}}$ is the diffraction vector from the region of interest **[15]**. The purpose of using a Lorentz lens is to extend the holographic field of view.

Finally by applying the FT on the interference pattern (Eq. 10) the following terms are achieved.

$$\begin{aligned} FT\left(I_{fringes}\right) = \delta(q) + FT(A(\mathbf{r})^2) \quad & \text{Center band} \\ +V.\,FT(A\exp(i\phi))\otimes\delta(\mathbf{q}-\mathbf{q_c}) \quad & +\text{ Side band} \\ +V.\,FT(A\exp(i\phi))\otimes\delta(\mathbf{q}+\mathbf{q_c}) \quad & -\text{ Side band} \end{aligned} \tag{11}$$

where **q** is the spatial frequency. Eq. 11 expresses the interference pattern in the Fourier space. The center band is carrying the amplitude information of both elastically and inelastically scattered electrons and two side bands are carrying the same phase information of the beam. The side bands are just complex conjugate of each other. Spatially filtering one of the side bands and inverse FT of the side band finally give the phase image which can be used to determine the atomic displacement using the geometric phase relationship.

This technique is applied by few researchers to determine the atomic displacement inside semiconductors [15, 16]. The specimen fabrication for DFEH is very crucial and challenging. Additionally in DFEH studies, the observed displacement field, **R(**r**)**, is the linear average of the displacement over the thickness of the specimen that the electron beam traverses, **R**(z). Therefore the displacement variation through the specimen thickness, which can be considered as the third dimension, is still missing. The in plane projected atomic displacement, **R(**r**)**, is the integration of the displacement at different depth in the specimen, **R**(z), which is in agreement with the split HOLZ line dependency on the atomic displacement along the z-axis. Some works have been done to simulate the missing dimension using **R(**r**)** measured by DFEH. Javon et al. [52, 53] developed an expression to use the DFEH reconstructed geometric phase in order to simulate the third missing dimension, **R**(z). They introduced a weighting function which is a function of the extinction distance, ξ_g, deviation parameter, s, and the specimen thickness, t. Therefore the reconstructed geometric phase turns into;

$$\phi_g = -2\pi \int_0^t f_R^g(z)\mathbf{g}.\mathbf{R}(\mathbf{z})dz \tag{12}$$

where $f_R^g(z)$ is the weighting function that is different for every diffracted beam due to its direct relationship with the extinction distance or dynamical diffraction effect.

Their study on the weighting function for different diffracted beams results in showing a strong dependency of **R**(z) in the simulations on the dynamical diffraction. For instance, 111 diffracted beam in Si has a small extinction distance, ξ_{111} =79.4 nm and shows a high oscillation of the weighting function whereas the weighting function has a smaller oscillation for 008 diffraction beam, ξ_{008} =540 nm, and the geometrical phase for 008 will not be influenced by the dynamical diffraction. Therefore, higher index planes with higher extinction distances are less affected by the dynamical diffraction. An explicit solution for this effect is to perform DFEH with high index diffraction beams, which are potentially kinematical, however they are unfortunately inaccessible by DFEH due to their high Bragg angle [52, 53].

The weighting function is also influenced by the thickness change and the deviation factor. Therefore changes in the specimen orientation and thickness, the experimental condition and the diffracted beam bring a different weighting function. Consequently the evolution of the weighting function for different diffracted beams and experimental conditions can be a limit in the simulation of the z-dependent atomic displacement via DFEH.

2.4 Summary

HOLZ lines are high index diffracted beams with the highest sensitivity to the atomic displacement. HOLZ line positional change has been used to measure the 2D atomic displacement, which is the average of the displacement vectors at different depth of the material. Since the path length of the electron beam changes while passing through a bent crystal they are observed as a split of the intensity peaks on the observation plane. The change in the path length adds a phase factor to the diffracted beam at the exit surface of the specimen. Therefore, it is more straightforward to obtain the phase information of the diffracted beam. DFEH is the best candidate to measure the phase of the diffracted beam, however it measures the projection of the z-dependent atomic displacement on the xy plane and it requires a uniform specimen in terms of thickness and composition to remove extra contributions in the phase. Applying a weighting function to simulate **R**(z) is also sensitive to the dynamical diffraction. It is suggested to perform DFEH using higher Bragg diffracted beams which are not accessible in DFEH.

Contrary to the efforts done in the z-dependent atomic displacement measurement there is still no experimental method which can obtain the atomic displacement distribution through the thickness of the crystal, **R**(z).

Accordingly, the focus of this work is to establish a novel technique to reconstruct the phase information of the diffracted beam in order to measure the z-dependent atomic displacement, **R**(z). The reconstructed phase needs to be strain-dependent with no contribution of the thickness change and the composition change to simplify the calculations and the specimen preparation.

Since the split HOLZ line internal fringes carry the z-dependent displacement distribution along the beam direction, the aim is to recover the phase profile across the split HOLZ line which will be the first experimental procedure enables measuring the phase directly related to **R**(z).

As a recall, the contribution of this work is to introduce the theory of the technique, the experimental details in fabricating the specimen, obtaining the interference pattern and reconstructing the phase image and interpreting the result with the developed analytical approach. Chapter 3 and Chapter 4 are the main contributions of the current work. In Chapter 3, the theoretical details of the technique are introduced which are followed by the analytical calculation of the phase profiles for some suggested z-dependent displacement profiles. The analytical approach is then supported by the experimental procedure and results in Chapter 4.

Chapter 3

Self-Interference of Split HOLZ line-Theory and Phase Calculation

This chapter focuses on the theoretical development of a novel technique which enables reconstructing the phase profile across the split HOLZ line in order to determine the z-dependent displacement profile. The technique is called self-interference of split HOLZ line (SIS-HOLZ) [54, 55]. All the phase simulations and related equations in this chapter are derived in order to study the z-dependent atomic displacement in semiconductors. This method can be categorised in the electron holography based techniques, however it is implemented in the diffraction mode. The SIS-HOLZ principles are based on the diffracted beam interferometry (DBI) which was first introduced by Herring et al. [56, 57, 58, 59, 60, 61]. Before defining the SIS-HOLZ method, some principles of the interferometry in the diffraction mode are presented in the following section.

3.1 The Interferometry in the Diffraction Space

This is a method of interfering the k-space electron intensity on the diffraction plane in a controlled manner using an electron biprism. The purpose is to obtain the phase change of the interfering beams. It is revealed that all electron intensities which are generated from a coherent electron source of a TEM including elastically scattered electrons (which form HOLZ lines) and inelastically scattered electrons (like those forming Kikuchi bands) have enough coherency to form fringes while self-interfered under a wide range of electron diffraction conditions. Unlike electron interferometry in the image mode, on the diffraction plane the angular separation of elastically and inelastically scattered acts as a spatial filter. Therefore, the combination of the interferometry on the diffraction plane with an imaging filter can give high contrast fringes. Generally in DBI, the electron beam coming from the source impinges on the specimen after passing the prefield (before specimen) lenses and is diffracted by the specimen. Then, it travels through the post specimen lenses and field free space until it reaches the electron biprism which is inserted in the selected area aperture holder. If the voltage on the biprism is chosen suitably then it deflects the diffracted beams towards each other by the opposite angles to overlap. The basic expression of the DBI image wave is related to the spatial frequency (k-space) representation which can be obtained by

a Fourier transform. Before showing the effect of the apertures, lenses and the specimen on the wave in the SIS-HOLZ, some principles are required to introduce.

In the spatial frequency space, the effect of isoplanatic lens aberrations on the image wave is taken into account with a multiplication by a complex factor. For example for the spherical aberration, it is

$$\exp\left(-\frac{i\pi}{2}C_s\lambda^3|\mathbf{k}|^4\right) \tag{13}$$

where C_s is the spherical aberration constant, λ is the electron wavelength and $\mathbf{k}$ is the spatial frequency vector. There is also a defocusing factor which must be considered. Finally, γ is introduced for both pre-field and post field spherical aberration and defocusing factor.

$$\gamma(k) = \frac{\pi}{2}C_s\lambda^3|\mathbf{k}|^4 + \pi\lambda\Delta Z|\mathbf{k}|^2 \tag{14}$$

where ΔZ is the defocus factor. The effect of the apertures on the electron can be added as a real factor represented by a window function, i.e. a rectangular function, Eq. 15. This has no effect on the phase of the beam, but depending on the size of the aperture, it effects on the intensity of the interfering sources and the contrast of the interference pattern. The rectangular aperture function operates as a filter results in cutting all spatial frequencies larger than K_A.

$$B(\mathbf{k}) = \begin{cases} 1 & \text{for} \quad |\mathbf{k}| < K_A \\ 0 & \text{for} \quad |\mathbf{k}| > K_A \end{cases} \tag{15}$$

Also, the interaction of the wave with the specimen and any other deflecting field is described by multiplying the wave by a transmission function, $\exp(-2\pi i\mathbf{K}\cdot\mathbf{r})$, which is equivalent to a convolution in the spatial frequency space. The Fourier transform of $\exp(\pm 2\pi i\mathbf{K}.\mathbf{r})$ is $\delta(\mathbf{k} \mp \mathbf{K})$ where δ is a delta function. This simply means a rigid displacement of the wave by an absolute value of $\mathbf{K}$, $|\mathbf{K}|$, on the diffraction plane. The effect of an aperture with a deflecting stage causing a rigid shift of $\mathbf{K}_T$ in the frequency space can be shown as

$$T(\mathbf{k} \mp \mathbf{K}_T) = B(\mathbf{k})\exp((\pm 2\pi i\mathbf{K}_T\cdot\mathbf{r})) \tag{16}$$

where $B(\mathbf{k})$ denotes the aperture function which is a window function referring to the filtering in real space or Fourier space. The value of $B(\mathbf{k})$ for the frequencies smaller than K_A is 1 and it is zero for spatial frequencies larger than K_A. So it is considered as a

constant coefficient equals to 1 for the rest of the calculations. T symbolizes the transmission function and $\mathbf{K_T}$ is a rigid displacement in the frequency space due to the interaction with any deflecting field other than the specimen and the biprism. The specimen is also considered as a tilting stage which contributes to the transmission function by

$$\Sigma_j A_j \exp\left(2\pi i \mathbf{g_j} \cdot \mathbf{r}\right) \tag{17}$$

A is the complex amplitude of the diffracted beam, **g** is the diffraction vector and j denotes the replicas of the electron beams. Eq. 17 corresponds to Eq. 1 which is the diffracted beam equation from a perfect crystal.

Considering the specimen effect on the electron wave, the imaging wave function after the specimen plane in the spatial frequency space can be represented by

$$\Sigma_j A_j \, T\left(\mathbf{k} - \mathbf{K_T} - \mathbf{g_j}\right) \exp\left(-i\gamma_A \left|\mathbf{k} - \mathbf{g_j}\right|\right) \tag{18}$$

From the specimen to the biprism, the beam is first disturbed by the spherical aberration of the post-field (post specimen) objective lens, C_{SB}. Since the interference occurs in the k-space, it is required to bring the biprism into the near focus condition on the diffraction plane. Therefore, a biprism defocus factor is needed which can be adjusted by the objective lens current or the specimen height. The biprism defocus is shown schematically in the SIS-HOLZ setup in Section 3.1.1. The deflection of the electron beam due to the biprism voltage is also expressed as a rigid displacement in the spatial frequency plane by $\pm\mathbf{K_B} = \pm(\alpha_B/\lambda)\mathbf{b}$ plus an additional phase factor of $\exp(\pm 2\pi i \, \mathbf{K}_B \cdot \mathbf{r_B})$. Here, α_B is the deflection angle directly related to the biprism voltage (V_B) and the voltage of the TEM (E) through $\alpha_B \propto V_B/E$, **b** is the biprism unit vector which is perpendicular to the unit vector, and $\mathbf{r_B}$ is the coordination of a generic point on the biprism axis. The term $\exp(\pm 2\pi i \, \mathbf{K_B} \cdot \mathbf{r_B})$ represents the phase sensitivity to the position of the electron beam with respect to the biprism wire and the earthed plates, which is explained in detail in Section 3.1.3. Therefore, the waves passing both sides of the biprism experience the extra phase factor which is called $T_B(\mathbf{r_B})$. $T_B(\mathbf{r_B})$ includes the biprism displacement effect on the phase profile. Ultimately the wave function resulting from DBI has two contributions, one goes the left side of the biprism and the other goes to the right side of the biprism.

$$\Phi_{\text{Left}} = \Sigma_{jL} A_{jL} \exp(2\pi i \mathbf{K_B} \cdot \mathbf{r_B}) \times T\left(\mathbf{k} + \mathbf{K_B} - \mathbf{K_T} - \mathbf{g_{jL}}\right) \times \exp(-i\gamma_A \left|\mathbf{k} + \mathbf{K_B} - \mathbf{g_{jL}}\right|) \times \exp(-i\gamma_B |\mathbf{k} + \mathbf{K_B}|) \quad (19)$$

$$\Phi_{\text{Right}} = \Sigma_{jR} A_{jR} \exp(-2\pi i \mathbf{K_B} \cdot \mathbf{r_B}) \times T\left(\mathbf{k} - \mathbf{K_B} - \mathbf{K_T} - \mathbf{g_{jR}}\right) \times \exp(-i\gamma_A \left|\mathbf{k} - \mathbf{K_B} - \mathbf{g_{jR}}\right|) \times \exp(-i\gamma_B |\mathbf{k} - \mathbf{K_B}|) \quad (20)$$

Now the resultant wave function is $\Phi_{\text{Resultant}} = \Phi_{\text{Left}} + \Phi_{\text{Right}}$ and the phase will be obtained by

$$\phi = \tan^{-1} \frac{\text{Im}(\Phi_{\text{Resultant}})}{\text{Re}\,(\Phi_{\text{Resultant}})} \quad (21)$$

The explained routine is employed to calculate the phase profile across the split HOLZ line in a strained specimen which is explained next.

3.1.1 Self-interference of Split HOLZ line (SIS-HOLZ)

The specimen in this work was superlattices of $Si/Si_{0.8}Ge_{0.2}$ on the Si substrate, Fig.9.

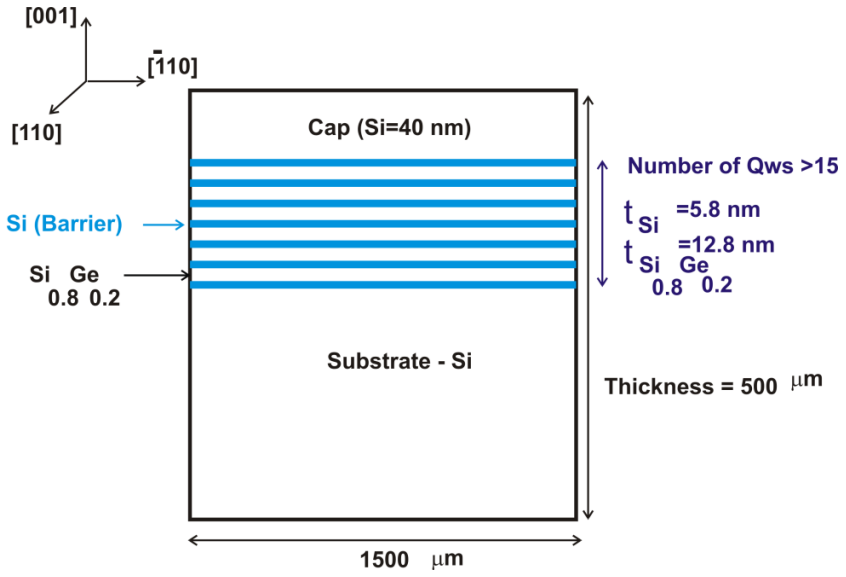

Fig.9- A schematic of the bulk sample cross-section, showing the thickness of the superlattices, the cap layer, and Si substrate.

This work is developed using $Si/Si_{0.8}Ge_{0.2}$ quantum wells. Si and Ge are very favorable in semiconductor industry. Si is the eighth most abundant element in the universe by mass. Si and Ge both have diamond cubic structure. Ge is highly miscible in Si. In the past decades, germanium has found new applications as a key material for the electronic-photonic integration on the silicon platform. Their indirect band gap make them unsuitable for optoelectronics such as laser diodes or light emitting diodes (LEDs) and etc. Although Si is cheap and a widely available semiconductor material. So it is the basis of modern electronics. Si/Si_xGe_{1-x} superlattices are widely used in thermoelectric applications, for example in the power stations. Therefore, the thermal gradient is converted to the electricity. So, low thermal conductive semiconductors with indirect bandgaps are favorable. Si is not a good thermoelectric material by itself due to its low thermoelectric conversion efficiency. Si/Si_xGe_{1-x} superlattices instead are very promising for this application due to the low thermal conductivity and high thermoelectric conversion efficiency. Thermoelectric conversion efficiency is directly related to the electrical conductivity, band structure, which is affected by the beneficial strain in superlattices.

Quantum devices are also an area of intense research for Si/Si_xGe_{1-x} quantum wells. While many recent advances in quantum devices have happened using GaAs materials system, silicon has a very unique position. It has the smallest spin-orbit coupling comparing with any currently practical semiconductor material, due to its high position in the periodic table. Additionally, the predominant isotope of silicon is Si-28, with nuclear spin zero. The bandgap of bulk Si is larger than that of Si_xGe_{1-x}. Therefore, at their interface the conduction-band edge of Si would lie above that of Si_xGe_{1-x} and the valence-band edge would lie below that of Si_xGe_{1-x}. This is type I of the band alignment. In type II of the band alignment the bandgap of Si remains larger than unstrained Si_xGe_{1-x}. The biaxial tensile strain on Si, causes the edge of the conduction band in Si decreases relative to unstrained Si_xGe_{1-x}. This type of band alignment causes quantum confinement in Si/ Si_xGe_{1-x} quantum wells. By increasing the mole fraction of Ge from 0 to x the conduction band edge in unstrained Si is split decreasing the bandgap energy. Si barrier layers act as quantum wells and electrons supplied either by the voltage or Si_xGe_{1-x} layers are confined at the Si/ Si_xGe_{1-x} interfaces. x can change from 0.20 to

0.35 in quantum computers. This range provides conduction-band offsets between the Si well and Si_xGe_{1-x} layers of roughly 100–200 meV. Larger values of x could be used, but doing so would impose severe limits on the thickness of the Si well due to strain considerations [62]. This signifies the impact of strain measurement techniques in developing quantum computers.

Due to the lattice mismatch between Si and SiGe, when SiGe is epitaxially grown on the relaxed Si, often referred to as a virtual substrate, both Si substrate and SiGe epitaxy layer will acquire different atomic spacing comparing with their original spacing and become strained, Fig. 10. Generally the lattice mismatch can be accommodated by strain and/or misfit dislocations. Accommodation by strain only is obtained with layers thinner than a critical thickness, t_C. As it can be seen in Fig. 10, in pseudomorphic strained SiGe layer, there is tensile strain in y direction (growth direction) and compressive strain in x direction. The tensile and compressive strains are in the opposite directions in Si substrate. Considering a bulk specimen, as long as the epitaxial layer thickness is lower than the critical thickness, t_C, the pseudomorphic layers of Si and SiGe are strained uniformly along the x and y directions. Exceeding t_C results in the relaxation of Si and SiGe layers by producing misfit dislocations. If the specimen is a thin film the surface relaxation will cause non-uniform strain in z-direction. Therefore, the pseudomorphic strained planes will be relaxed on the top and the bottom surfaces of the specimen. Hence, it is expected to have maximum displacement at the center of the specimen along the z-axis. This results in a non-uniform strain profile, i.e. bending in the z direction.

The non-uniform atomic displacement along the z direction cause the HOLZ line split. Several studies have been reported on the relation between the split HOLZ lines and the atomic displacement profile along the Si interface with SiGe or Ge in TEM thin and relaxed specimens [23, 38, 39, 43, 44, 63]. Mostly Finite Element Method (FEM) is used to model the atomic displacement field in the system. Accordingly, there are three main displacements profiles borrowed in this work to develop the analytical approach of the SIS-HOLZ. These profiles are conventionally called, V-shape/triangle profile, bell-shape profile and parabola profile. Later in this chapter the mathematical functions of the

displacement profiles are presented. Before, reporting the mathematical development of the approach, the SIS-HOLZ methodology is presented in the following.

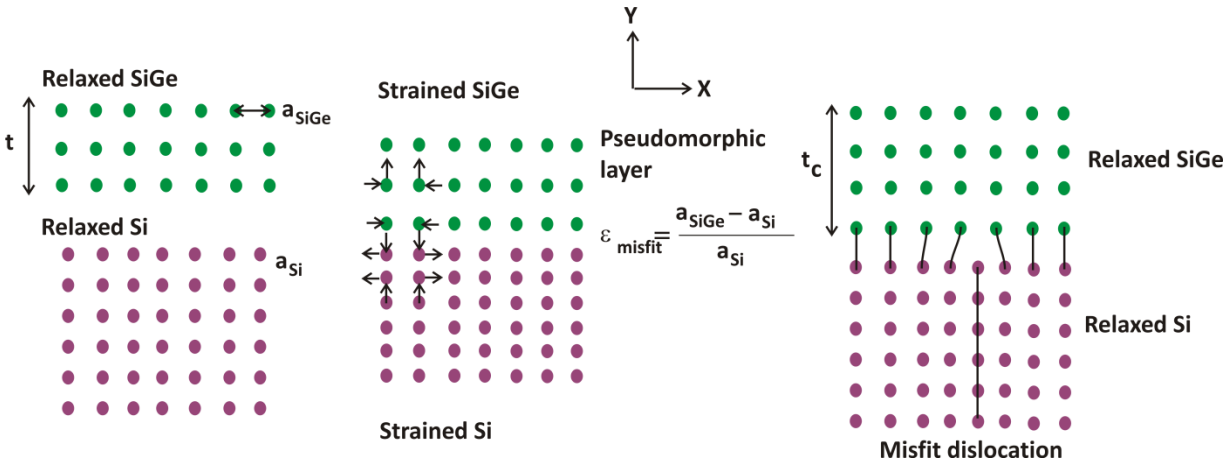

Fig. 10- The relationship between lattice mismatch of Si and SiGe and misfit strain and dislocation.

SIS-HOLZ is a diffracted beam interferometry based technique which self-interferes the split HOLZ line to retrieve the phase profile across the split HOLZ line. The SIS-HOLZ is shown schematically in Fig. 11. S_1 and S_2 represent the interfering virtual sources in the k-space representing the split HOLZ line and, L is the camera length. In Fig. 11, Z_O is the specimen plane, Z_1 and Z_{OB} are respectively the planes conjugate to the virtual sources (S_1 and S_2) and the electron biprism. The term $Z_{OB} - Z_O$ is the biprism defocus. The biprism defocus helps to focus the virtual sources on the plane Z_1. After focusing the biprism image on Z_1 by adjusting the biprism defocus, the biprism needs to be placed in the middle and parallel with the split HOLZ line i.e., perpendicular to the HOLZ line's **g** vector, $\mathbf{g}||\mathbf{b}$. Then, by applying a voltage on the biprism, two sides of the split are deflected towards each other and interfered giving the interference fringes (interferogram) on the diffraction plane. Rearranging Eq. 19 and Eq. 20 for the SIS-HOLZ method gives

$$\phi^{-}_{shifted} = \Sigma_{j\mathbf{s}_1} A_{j\mathbf{s}_1} \exp(-2\pi i \mathbf{g_{j1}} \cdot \mathbf{R}(z)) \exp(-2\pi i \mathbf{S_1} \cdot \mathbf{r}) \times T(\mathbf{k} + \mathbf{K_B} - \mathbf{K_T}) \times \exp(+2\pi i \mathbf{K_B} \cdot \mathbf{r_B}) \quad (22)$$

$$\times \exp(-i\gamma_A|\mathbf{k}+\mathbf{g_{j1}}+\mathbf{S_1}+\mathbf{K_B}|)\times \exp(-i\gamma_B|\mathbf{k}+\mathbf{g_{j1}}+\mathbf{S_1}+\mathbf{K_B}|)$$

$$\phi^{+}_{\text{shifted}} = \Sigma_{j\mathbf{s}_2} A_{j\mathbf{s}_2} \exp(-2\pi i \mathbf{g_{j2}}\cdot\mathbf{R}(z)) \exp(-2\pi i \mathbf{S_2}\cdot\mathbf{r})$$

$$\times T(\mathbf{k}-\mathbf{K_B}-\mathbf{K_T})\times \exp(-2\pi i \mathbf{K_B}\cdot\mathbf{r_B}) \quad (23)$$

$$\times \exp(-i\gamma_A|\mathbf{k}+\mathbf{g_{j2}}+\mathbf{S_2}-\mathbf{K_B}|)\times \exp(-i\gamma_B|\mathbf{k}+\mathbf{g_{j2}}+\mathbf{S_2}-\mathbf{K_B}|)$$

Note, $\mathbf{K}_T$ is identical in both interfering beams and will be removed from the final wave function. A_{S_1} and A_{S_2} denote the amplitudes of the split HOLZ line from two left and right halves of the split. j is an integer showing the array of the replicas of the diffracted intensities deviated from the exact Bragg position due to the bend, and i is the complex number. $\mathbf{g_{j1}} = \mathbf{g_{j2}}$ is the reciprocal wave vector of the HOLZ line and $\mathbf{S_1}$ and $\mathbf{S_2}$ are the two left and right halves of the split. $\mathbf{K_B}$ can be considered as the rigid displacement of the beam due to the deflection angle, α_B. $\mathbf{S_1}$ and $\mathbf{S_2}$ are two sides of the split HOLZ line with respect to the center of split. They represent the diffracted beams coming from the bottom and the top sides of the specimen, assuming the center as the origin. $\phi^{+}_{\text{shifted}}$ represents the diffracted wave passing through the right side of the biprism deflected to the left side. According to the SIS-HOLZ schematic (Fig. 11) the contributed diffracted beam in $\phi^{+}_{\text{shifted}}$ is $\mathbf{S_2}$. Correspondingly, $\phi^{-}_{\text{shifted}}$ represents the diffracted wave passing through the left side of the biprism deflected towards the right side and $\mathbf{S_1}$ is the contributed to the diffracted beam in $\phi^{-}_{\text{shifted}}$. Eq. 22 and Eq. 23 are the simple presentations of the two interfering diffracted beams deflected by the biprism and influenced by the aberration.

The extra phase factor of $\exp(\pm 2\pi i \mathbf{K_B}\cdot\mathbf{r_B})$ which is attributed to the biprism displacement effect is neglected in this work due to the biprism adjustment in the center of the spit, parallel with the HOLZ. The observation carried out in the diffraction mode and the general interferogram intensity is given by

$$I = |\Phi|^2 = |\phi^{-}_{\text{shifted}} + \phi^{+}_{\text{shifted}}|^2 \quad (24)$$

The first terms in Eq. 22 and Eq. 23 correspond to the Howie-Whelan equation for an imperfect bent crystal specimen. Accordingly, in order to calculate the reconstructed phase across the split SIS-HOLZ line, the solution of the Howie-Whelan equation must

be multiplied by several phase factors coming from the effect of the biprism, the spherical aberration and the defocus effect.

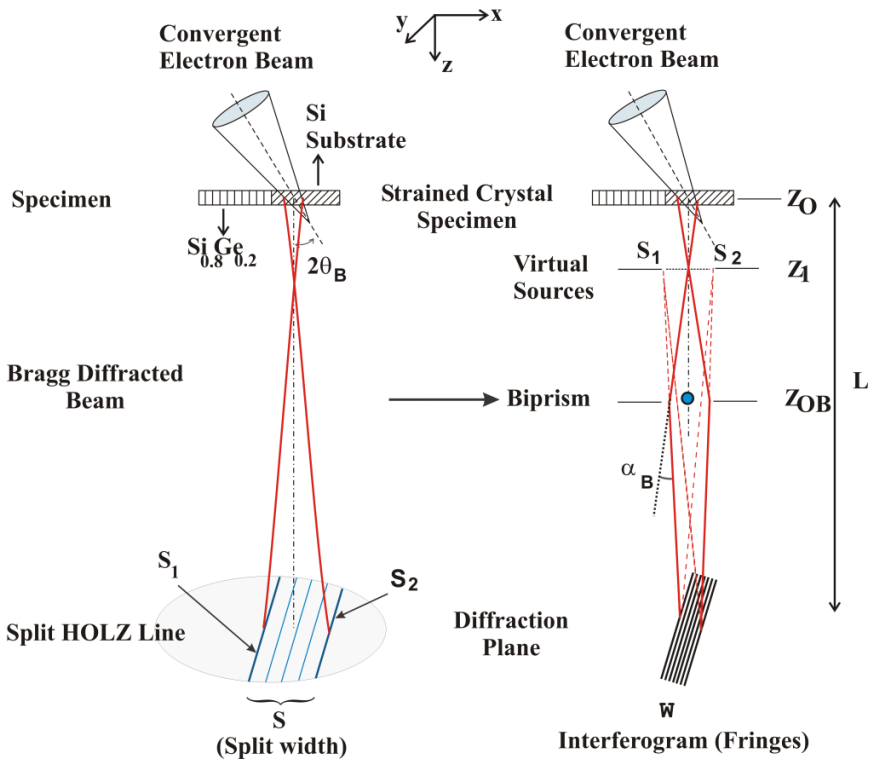

Fig. 11- A simplified diagram of the SIS-HOLZ technique. By applying a voltage on the biprism, the intensities passing either of its sides deflect towards each other by an angle of α_B to self- interfere. The region of interest (ROI) for conducting the experiment was in the Si substrate close to its interface with superlattices. Here, S_1 is from the bottom half side of the specimen and S_2 comes from the top half side of the specimen, if the beam is under-focused as in the diagram [27, 64].

The analytical solution of the Howie-Whelan equation is found for three different z-dependent atomic displacements in a thinned specimen. The solutions are then plugged into Eq. 22 and Eq. 23. Finally $\phi^{+}_{shifted}$ and $\phi^{-}_{shifted}$ are added and Eq.21 gives the phase change across the split HOLZ line. In order to solve Howie-Whelan equation, Eq. 5, Φ_g can be expressed as the Fourier transform (FT) of the extra phase factor, $\exp(2\pi i \mathbf{g}\cdot \mathbf{R}(z))$, multiplied by a rectangular (slit) function, $\prod(z)$ [24, 43, 64]. Therefore, Φ_g can be rearranged,

$$\Phi_g(s) = \frac{i\pi}{\xi_g}\int_{-\infty}^{+\infty} \exp\left(-2\pi i \boldsymbol{g}\cdot\boldsymbol{R}(z)\right)\prod_{-\frac{t}{2}}^{\frac{t}{2}}(z)\ \exp(-2\pi i s z)dz \qquad (25)$$

Since the solution of the Howie-Whelan equation is separated into two halves, Eq.25 can be expressed as the generic form of:

$$\begin{aligned}\Phi_g(s) = &\frac{i\pi}{\xi_g}\int_{-\infty}^{+\infty} \exp(-2\pi i \mathbf{g}\cdot\mathbf{R}(z))\ \prod_{-\frac{t}{4}}^{\frac{t}{4}}\left(z+\frac{t}{4}\right)\ \exp(-2\pi i s z)\,dz \\ &+\ \frac{i\pi}{\xi_g}\int_{-\infty}^{+\infty} \exp\left(-2\pi i \mathbf{g}\cdot\mathbf{R}(z)\right)\prod_{-\frac{t}{4}}^{\frac{t}{4}}\left(z-\frac{t}{4}\right)\ \exp(-2\pi i s z)\ \ dz\end{aligned} \qquad (26)$$

The FT of the rectangular function is a sinc function. Therefore, the FT of a shifted rectangular function is,

$$\int_{-\infty}^{+\infty}\prod_{-\frac{t}{4}}^{\frac{t}{4}}\left(z\pm\frac{t}{4}\right)\ \ \exp(-2\pi i s z)dz = \exp\left(2\pi i s\left(\pm\frac{t}{4}\right)\right)\left(\frac{t}{2}\right)\mathrm{sinc}\left(\pi s\frac{t}{2}\right) \qquad (27)$$

Substitution of Eq. 27 into Eq. 26 gives

$$\begin{aligned}&\Phi_g(s)= \\ &\frac{i\pi}{\xi_g}\int_{-\infty}^{+\infty}\exp(-2\pi i\mathbf{g}\cdot\mathbf{R}(z))\exp(-2\pi i\mathbf{sz})\ dz\otimes\exp\left(2\pi i s\left(+\frac{t}{4}\right)\right)\left(\frac{t}{2}\right)\mathrm{sinc}\left(\pi s\left(\frac{t}{2}\right)\right) \\ &+\frac{i\pi}{\xi_g}\int_{-\infty}^{+\infty}\exp(-2\pi i\mathbf{g}\cdot\mathbf{R}(z))\exp(-2\pi i\mathbf{sz})\ dz\otimes\exp\left(2\pi i s\left(-\frac{t}{4}\right)\right)\left(\frac{t}{2}\right)\mathrm{sinc}\left(\pi s\left(\frac{t}{2}\right)\right)\end{aligned} \qquad (28)$$

where $\otimes$ is the convolution operator. In Eq. 28, the first term represents the diffracted wave coming from the bottom part which corresponds to $\Phi_g(S_1)$ and the second term denotes the diffracted beam coming from the top side of the specimen, $\Phi_g(S_2)$.

The atomic displacement through the thickness of a crystal, Fig. 12, **R**(z), can be assumed as a V-shape, a bell-shape, or a parabola profile. The **R**(z) direction is considered consistent with respect to the **g** vector and is indicated as Rf(z) where R is a scalar representing the atomic displacement amplitude over the crystal thickness and f(z)

shows the displacement distribution function along the beam direction. $\mathbf{g}\cdot\mathbf{R}(z) = gRf(z)\cos\beta$ where β can be considered as the angle between the **g** vector and the displacement vector, **R**(z), Fig. 12. Assuming **g** being parallel with **R**(z) ($\beta = 0$), the extra phase factor of $\exp(-2\pi i\mathbf{g}\cdot\mathbf{R}(z))$ is simplified into $\exp(-2\pi igRf(z))$. For different displacement profile functions, various diffracted beam functions can be achieved. In the following the analytical solution of Howie-Whelan equation for various z-dependent displacement distribution functions, f(z), are presented.

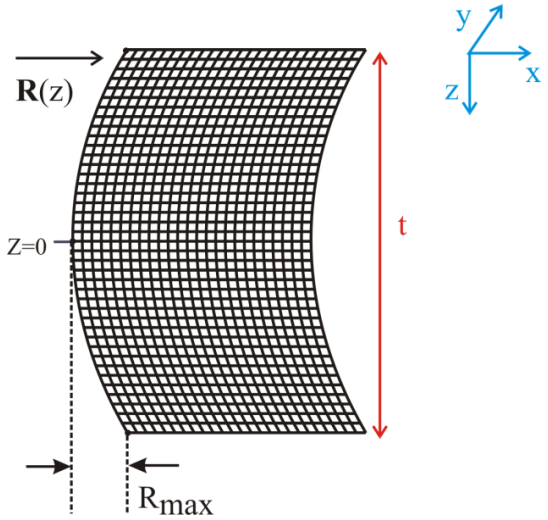

Fig. 12 – A schematic drawing of a lattice with a bending distortion. **R**(**z**) is the displacement vector. $\mathbf{R_{max}}$ denotes the maximum displacement.

3.1.1.1 Analytical Solution of Howie-Whelan Equation for a V-shape Displacement Profile

Consider a V-shape (triangle) displacement distribution along the z-axis as

$$Rf(z) = \begin{cases} \frac{R}{t}\left(z + \frac{t}{2}\right) & -\frac{t}{2} \le z \le 0 \\ \frac{R}{t}\left(\frac{t}{2} - z\right) & 0 \le z \le \frac{t}{2} \end{cases} \qquad (29)$$

R in the right side of Eq. 29 is 2α where α is a real number and the atomic displacement amplitude on the left side of Eq. 29 is equal to α. Therefore, the atomic displacement amplitude is $R = \alpha$ and the displacement function is $\frac{2}{t}\left(z \pm \frac{t}{2}\right)$. In order to

avoid introducing more variables, staying consistent with R as the atomic displacement amplitude in all three profiles, it is preferred to put 2 inside R on the right side of Eq. 29. Here, zero displacement occurs on the surface of the specimen. By applying the analytical solution to the diffracted wave function from a specimen carrying a V-shape displacement profile, the following equation can be obtained.

$$\begin{aligned}\Phi_g(s) &= \Phi_g(S_1) + \Phi_g(S_2)\\ &= \frac{i\pi}{\xi_g}\int_{-\infty}^{+\infty}\exp\left(-\frac{2\pi igR}{t}\left(\frac{t}{2}+z\right)\right)\exp(-2\pi isz)\,dz\\ &\otimes\exp\left(2\pi is\left(+\frac{t}{4}\right)\right)\left(\frac{t}{2}\right)\mathrm{sinc}\left(\pi s\left(\frac{t}{2}\right)\right)\\ &+\frac{i\pi}{\xi_g}\int_{-\infty}^{+\infty}\exp\left(-\frac{2\pi igR}{t}\left(\frac{t}{2}-z\right)\right)\exp(-2\pi isz)\,dz\\ &\otimes\ \exp\left(2\pi is\left(-\frac{t}{4}\right)\right)\left(\frac{t}{2}\right)\mathrm{sinc}\left(\pi s\left(\frac{t}{2}\right)\right)\end{aligned} \tag{30}$$

The FT of $\exp\left(-\frac{2\pi igR}{t}\left(\frac{t}{2}\pm z\right)\right)$ are tabulated as

$$\int_{-\infty}^{+\infty}\exp\left(-\frac{2\pi igR}{t}\left(z\pm\frac{t}{2}\right)\right)\exp(-2\pi isz)\,dz = \exp(-\pi igR)\,\delta\left(s\pm\left(\frac{R}{t}\right)g\right) \tag{31}$$

where δ is a delta function. Substituting Eq.31 into Eq. 30 and performing the convolution, the diffracted beam equation for a V-shape displacement profile is

$$\begin{aligned}\Phi_g(s) &= \frac{i\pi}{\xi_g}\exp(-\pi igR)\,\delta\left(s+\left(\frac{R}{t}\right)g\right)\otimes\exp\left(+\pi is\left(\frac{t}{2}\right)\right)\left(\frac{t}{2}\right)\mathrm{sinc}\left(\pi s\left(\frac{t}{2}\right)\right)\\ &+\frac{i\pi}{\xi_g}\exp(-\pi igR)\,\delta\left(s-\left(\frac{R}{t}\right)g\right)\otimes\exp\left(-\pi is\left(\frac{t}{2}\right)\right)\left(\frac{t}{2}\right)\mathrm{sinc}\left(\pi s\left(\frac{t}{2}\right)\right)\\ &= \frac{i\pi}{\xi_g}\exp(-\pi igR)\exp\left(+\pi i\frac{t}{2}\left(s+\left(\frac{R}{t}\right)g\right)\right)\frac{\sin\left(\pi\left(\frac{t}{2}\right)\left(s+\left(\frac{R}{t}\right)g\right)\right)}{\pi\left(s+\left(\frac{R}{t}\right)g\right)}\\ &+\frac{i\pi}{\xi_g}\exp(-\pi igR)\exp\left(-\pi i\frac{t}{2}\left(s-\left(\frac{R}{t}\right)g\right)\right)\frac{\sin\left(\pi\left(\frac{t}{2}\right)\left(s-\left(\frac{R}{t}\right)g\right)\right)}{\pi\left(s-\left(\frac{R}{t}\right)g\right)}\end{aligned} \tag{32}$$

Regarding Eq. 32, the diffracted electron beam function has two terms, one from the top side of the specimen and one from the bottom side of the crystal. Comparing Eq. 32 with Eq. 22 and Eq. 23 reveals

$$\Phi_g(S_1) = \Sigma_{\mathbf{jS}_1} A_{\mathbf{jS}_1} \exp\left(-2\pi i \mathbf{g_{j1}} \cdot \mathbf{R}(z)\right) \exp(-2\pi i \mathbf{S_1} \cdot \mathbf{r})$$

$$\cong \frac{i\pi}{\xi_g} \exp(+2\pi i g R) \exp\left(-\pi i \frac{t}{2}\left(s + \left(\frac{R}{t}\right) g\right)\right) \frac{\sin\left(\pi\left(\frac{t}{2}\right)\left(s + \left(\frac{R}{t}\right) g\right)\right)}{\pi\left(s + \left(\frac{R}{t}\right) g\right)} \qquad (33)$$

$\Phi_g(S_1)$ represents the diffracted beam coming from the bottom part of a specimen with a V-shape displacement profile along the z-axis. The Diffracted beam coming from the top part of the specimen carrying a V-shape displacement profile is represented by

$$\Phi_g(S_2) = \Sigma_{\mathbf{jS}_2} A_{\mathbf{iS}_2} \exp\left(-2\pi i \mathbf{g_{j2}} \cdot \mathbf{R}(z)\right) \exp(-2\pi i \mathbf{S_2} \cdot \mathbf{r})$$

$$\cong \frac{i\pi}{\xi_g} \exp(-2\pi i g R) \exp\left(-\pi i \frac{t}{2}\left(s - \left(\frac{R}{t}\right) g\right)\right) \frac{\sin\left(\pi\left(\frac{t}{2}\right)\left(s - \left(\frac{R}{t}\right) g\right)\right)}{\pi\left(s - \left(\frac{R}{t}\right) g\right)} \qquad (34)$$

In order to have the resultant wave function of SIS-HOLZ it is required to add extra phase shifts introduced in Eq. 22 and Eq. 23. Comparing $\Phi_g(S_1)$ in Eq. 33 and $\Phi_g(S_2)$ in Eq. 34 with $\phi^{-}_{\text{shifted}}$ and $\phi^{+}_{\text{shifted}}$, the plus and minus shifted electron beams have extra phase factors as

- The biprism effect, $\exp(\mp 2\pi i \mathbf{K}_B \cdot \mathbf{r})$ and $\exp((\pm 2\pi i \mathbf{K}_B \cdot \mathbf{r}_B))$. These two phase factors are introduced through the transmission function of the biprism, i.e. $\Phi_g(S_{1,2})\exp(\mp 2\pi i K_B(r - r_B))$.
- Any tilting stage inserted between the condenser and the objective lenses, $\exp(-2\pi i \mathbf{K}_T \cdot \mathbf{r})$,
- Pre-field spherical aberration and defocus, $\exp\left(-i\gamma_A\left(|\mathbf{k} + \mathbf{g_{j1,2}} + \mathbf{S_{1,2}} \pm \mathbf{K}_B|\right)\right)$
- Post-field spherical aberration and defocus, $\exp\left(-i\gamma_B\left(\left|\mathbf{k} + \mathbf{g_{j1,2}} + \mathbf{S_{1,2}} \pm \mathbf{K}_B\right|\right)\right)$

Before applying the phase shifts to $\Phi(S_1)$ and $\Phi_g(S_2)$ some simplifications can be done on Eq. 22 and Eq. 23 as follows;

- A perfect overlap happens while on the diffraction plane, the biprism is centered in the split parallel with the HOLZ line. The width of the split is linearly related to the displacement of the atomic planes

$$s = \frac{8|\mathbf{g} \cdot \mathbf{R}|}{t} \tag{35}$$

Therefore, $s/2 = |\mathbf{S_1}| = |\mathbf{S_2}| = +4|\mathbf{g} \cdot \mathbf{R}|/t$. In a perfect overlap $\mathbf{K_B} = \mathbf{S_1} = -\mathbf{S_2}$. In the presence of a symmetric bent about $z = 0$, the extra phase factor due to the misplaced biprism which contributes the biprism phase shift, $\exp(-2\pi i \mathbf{K}_B \cdot \mathbf{r}_B)$, can be neglected. In the presence of a displaced or a misaligned biprism, an extra phase factor will come into account which is discussed in Section 3.1.3.

- Regarding Eq.14, the pre field and the post filed aberration factor is

$$\begin{aligned} &\gamma_A \left(\left|\mathbf{k} + \mathbf{g_{j1,2}} + \mathbf{S_{1,2}} \pm \mathbf{K}_B\right|\right) \\ &= \frac{\pi}{2} C_{sA} \lambda^3 |\mathbf{k} + \mathbf{g_{j1,2}} + \mathbf{S_{1,2}} \pm \mathbf{K}_B|^4 + \pi\lambda(Z_O - Z_1) \left|\mathbf{k} + \mathbf{g_{j1,2}} + \mathbf{S_{1,2}} \pm \mathbf{K}_B\right|^2 \end{aligned} \tag{36}$$

where C_{sA} is the spherical aberration constant of the pre-field objective lens and $Z_O - Z_1$ is the distance between the specimen plane and the focus probe position (Fig. 11). In the perfect overlap condition the spherical aberration on both $\phi^+_{shifted}$ and $\phi^-_{shifted}$ become identical and cancel when two beams interfere. Additionally in the SIS-HOLZ (Fig. 11), $Z_O - Z_1$ can be neglected since it is a few microns, i.e., close to zero with respect to the camera length, L. Therefore, the term γ_A can be dropped out from both $\phi^+_{shifted}$and $\phi^-_{shifted}$ while they are interfered.

- Regarding Eq. 14, the post filed aberration factor is

$$\begin{aligned} &\gamma_B \left(\left|\mathbf{k} + \mathbf{g_{j1,2}} + \mathbf{S_{1,2}} \pm \mathbf{K}_B\right|\right) \\ &= \frac{\pi}{2} C_{sB} \lambda^3 \left|\mathbf{k} + \mathbf{g_{j1,2}} + \mathbf{S_{1,2}} \pm \mathbf{K}_B\right|^4 \\ &+ \pi\lambda(Z_{OB} - Z_O) \left|\mathbf{k} + \mathbf{S_{1,2}} \pm \mathbf{K}_B\right|^2 \end{aligned} \tag{37}$$

Generally by considering ideal imaging the spherical aberration can be neglected, however an ideal lens does not exist. The post field spherical aberration can be removed with the same scenario mentioned for the pre-field spherical aberration but there will be the biprism defocus effect. $Z_{OB} - Z_O$, is the biprism defocus factor which is added to both shifted waves. $Z_{OB} - Z_O$ is a TEM dependent factor which varies in different TEMs but

it has the small value of few μm. Therefore, the phase factors added to $\Phi_g(S_1)$ and $\Phi_g(S_2)$ can be simplified into $\exp(\mp 2\pi i \mathbf{K_B} \cdot \mathbf{r})$.The resultant wave equation is rearranged considering the extra phase factor.

$$\begin{aligned}\Phi_{\text{Resultant}} &= \phi^{-}_{\text{shifted}} + \phi^{+}_{\text{shifted}} \\ &= \Phi_g(S_1)\exp(-2\pi i K_B \cdot r) + \Phi_g(S_2)\exp(+2\pi i K_B \cdot r)\end{aligned} \tag{38}$$

By applying Eq. 38 into Eq. 32, the final resultant wave function for a V-shape displacement profile is,

$$\Phi(s) = \left(\frac{i\pi}{\xi_g}\exp(-\pi i g R\ )\exp(+\pi i s\omega)\frac{\sin(\pi\left(\frac{t}{2}\right)\left(s+\left(\frac{R}{t}\right)g\right)}{\pi\left(s+\left(\frac{R}{t}\right)g\right)}\right) + \left(\frac{i\pi}{\xi_g}\exp(-\pi i g R)\exp(-\pi i s\omega)\frac{\sin(\pi\left(\frac{t}{2}\right)\left(s-\left(\frac{R}{t}\right)g\right)}{\pi\left(s-\left(\frac{R}{t}\right)g\right)}\right) \tag{39}$$

where, $\omega = t/2 - \alpha_B\ \mathbf{b}\cdot\mathbf{r}$ assuming $\pm K_B \propto \pm s/2$. $\Phi(s)$ represents the wave function of the self-interfered split HOLZ line coming from the top half and the bottom half sides of the specimen with a V-shape displacement profile.

3.1.1.2 Analytical Solution of Howie-Whelan Equation for a Bell Shape Displacement Profile

To have the phase profile approximation of a bell-shape displacement, a cosine function is considered [20, 43] to express the displacement distribution through the thickness of the crystal.

$$Rf(z) = R\cos\left(\frac{2\pi z}{t}\right) \tag{40}$$

The period of Eq.40 is related to the specimen thickness and zero displacement happens at $z = \pm t/4$. The maximum displacement amplitude, R, occurs at the center. Finally the scattered wave function including two terms coming from the half top side and the half bottom side of the specimen is

$$\Phi_g(s) \tag{41}$$

$$= \frac{i\pi}{\xi_g}\int_{-\infty}^{+\infty} \exp\left(-2\pi i g R \cos\left(\frac{2\pi z}{t}\right)\right)\exp(-2\pi i s z)\, dz \otimes \exp\left(\pi i s\left(\frac{t}{2}\right)\right)\frac{\sin\left(\pi s\left(\frac{t}{2}\right)\right)}{\pi s}$$

$$+ \frac{i\pi}{\xi_g}\int_{-\infty}^{+\infty} \exp\left(-2\pi i g R \cos\left(\frac{2\pi z}{t}\right)\right)\exp(-2\pi i s z) dz \otimes \exp\left(-\pi i s\left(\frac{t}{2}\right)\right)\frac{\sin\left(\pi s\left(\frac{t}{2}\right)\right)}{\pi s}$$

Following the same routine explained in Section 3.1.1.1, the FT of the exponential of the displacement function needs to be employed. The FT of the exponential of a cosine function is

$$\exp\big(-A\cos(2\pi B z)\big) = \sum_{-\infty}^{+\infty}(-1)^n(-i)^n J_n(iA)\delta(z - nb) \qquad (42)$$

where J_n is the n^{th} order Bessel function, $A = 2\pi i g R$ and $B = 1/t$. Therefore, Eq. 41 can be simplified to

$$\Phi_g(s) = \frac{i\pi}{\xi_g}\sum_{-\infty}^{+\infty}(i)^n J_n(2\pi g R)\delta\left(s - \frac{n}{t}\right) \otimes \exp\left(\pi i s\left(\frac{t}{2}\right)\right)\frac{\sin\left(\pi s\left(\frac{t}{2}\right)\right)}{\pi s} \qquad (43)$$

$$+ \frac{i\pi}{\xi_g}\sum_{-\infty}^{+\infty}(i)^n J_n(2\pi g R)\delta\left(s - \frac{n}{t}\right) \otimes \exp\left(-\pi i s\left(\frac{t}{2}\right)\right)\frac{\sin\left(\pi s\left(\frac{t}{2}\right)\right)}{\pi s}$$

Since $J(-m) = (-1)^n J_n(m)$, Eq. 43 is rearranged as follows;

$$\Phi_g(s) = \frac{i\pi}{\xi_g}\left[J_0(2\pi g R)\delta(s) + \sum_{n=1}^{n=+\infty}(i)^n J_n(2\pi g R)\{\delta(+q) + \delta(-q)\}\right] \otimes \exp\left(\pi i s\left(\frac{t}{2}\right)\right)\frac{\sin\left(\pi s\left(\frac{t}{2}\right)\right)}{\pi s} \qquad (44)$$

$$+ \frac{i\pi}{\xi_g}\left[J_0(2\pi g R)\delta(s) + \sum_{n=1}^{n=+\infty}(i)^n J_n(2\pi g R)\{\delta(+q) + \delta(-q)\}\right] \otimes \exp\left(-\pi i s\left(\frac{t}{2}\right)\right)\frac{\sin\left(\pi s\left(\frac{t}{2}\right)\right)}{\pi s}$$

where $\pm q = s \pm nB$. Finally, the resultant wave function from the superposition of two halves of the split HOLZ lines coming from a crystal specimen with a cosine bell-shape displacement profile is,

$$\Phi(s) = \frac{i\pi}{\xi_g}\left[J_0(2\pi gR)\exp\left(\pi is\left(\frac{t}{2}\right)\right)\frac{\sin\left(\pi s\left(\frac{t}{2}\right)\right)}{\pi s}\right]$$
$$+\frac{i\pi}{\xi_g}\left[\sum_{n=1}^{+\infty}(i)^n J_n(2\pi gR)\left(\exp\left(\pi i\left(s+\frac{n}{t}\right)\left(\frac{t}{2}\right)\right)\frac{\sin\left(\pi\left(s+\frac{n}{t}\right)\left(\frac{t}{2}\right)\right)}{\pi\left(s+\frac{n}{t}\right)}\right)\right]$$
$$+\frac{i\pi}{\xi_g}\left[\sum_{n=1}^{+\infty}(i)^n J_n(2\pi gR)\left(\exp\left(\pi i\left(s-\frac{n}{t}\right)\left(\frac{t}{2}\right)\right)\frac{\sin\left(\pi\left(s-\frac{n}{t}\right)\left(\frac{t}{2}\right)\right)}{\pi\left(s-\frac{n}{t}\right)}\right)\right]$$
$$\times\exp(-2\pi i\mathbf{K}_B\cdot\mathbf{r})$$
$$+\frac{i\pi}{\xi_g}\left[J_0(2\pi gR)\exp\left(-\pi is\left(\frac{t}{2}\right)\right)\frac{\sin\left(\pi s\left(\frac{t}{2}\right)\right)}{\pi s}\right] \quad (45)$$
$$+\frac{i\pi}{\xi_g}\left[\sum_{n=1}^{+\infty}(i)^n J_n(2\pi gR)\left(\exp\left(-\pi i\left(s+\frac{n}{t}\right)\left(\frac{t}{2}\right)\right)\frac{\sin\left(\pi\left(s+\frac{n}{t}\right)\left(\frac{t}{2}\right)\right)}{\pi\left(s+\frac{n}{t}\right)}\right)\right]$$
$$+\frac{i\pi}{\xi_g}\left[\sum_{n=1}^{+\infty}(i)^n J_n(2\pi gR)\left(\exp\left(-\pi i\left(s-\frac{n}{t}\right)\left(\frac{t}{2}\right)\right)\frac{\sin\left(\pi\left(s-\frac{n}{t}\right)\left(\frac{t}{2}\right)\right)}{\pi\left(s-\frac{n}{t}\right)}\right)\right]$$
$$\times\exp(+2\pi i\mathbf{K}_B\cdot\mathbf{r})$$

Rearrangement of Eq.45 gives

$$\Phi(s) = \frac{i\pi}{\xi_g}\left[J_0(A)(\exp(\pi is\omega)+\exp(-\pi is\omega))\ \frac{\sin\left(\pi s\left(\frac{t}{2}\right)\right)}{\pi s}\right]$$
$$+\frac{i\pi}{\xi_g}\left[\sum_{1}^{+\infty}(i)^n J_n(A)(\exp(\pi i(+q)\omega)+\exp(-\pi i\,(-q)\omega))\frac{\sin\left(\pi(+q)\left(\frac{t}{2}\right)\right)}{\pi(+q)}\right] \quad (46)$$
$$+\frac{i\pi}{\xi_g}\left[\sum_{1}^{+\infty}(i)^n J_n(A)(\exp(\pi i(+q)\omega)+\exp(-\pi i\,(-q)\omega))\frac{\sin\left(\pi(-q)\left(\frac{t}{2}\right)\right)}{\pi(-q)}\right]$$

In thin specimens zero displacement can be held by the surfaces due to the strain relaxation on the surface [43]. Therefore, some modification on the introduced cosine

profile in Eq. 40 gives the surface relaxed bell-shape displacement profile through the specimen thickness.

$$\mathrm{Rf(z)} = \frac{\mathrm{R}}{2}\left(\cos\left(\frac{2\pi \mathrm{z}}{\mathrm{t}}\right) + 1\right) \tag{47}$$

The new cosine function changes the resultant wave function into $\exp(-\pi \mathrm{igR})\,\Phi(\mathrm{s})$ where A is equivalent to πigR in this case.

3.1.1.3 Analytical Solution of Howie-Whelan Equation for a Parabola Displacement Profile

For a parabola displacement function, a cosine function is considered with the period and amplitude twice as the bell-shape function introduced in Eq. 40. This allows to stay with the same amplitude of atomic displacement. Therefore, the atomic displacement amplitude is 2R. This modifies the displacement profile from a bell-shape to a parabola through the specimen thickness. In this profile zero displacement happens at the surfaces and the maximum displacement occurs in the center of the specimen. Since a cosine function is used to define the z-dependent parabola displacement and the profile just depends on the amplitude and the period of the function, it is preferably called a pseudo-parabola function as follows;

$$\mathrm{Rf(z)} = 2\mathrm{R}\cos\left(\frac{\pi \mathrm{z}}{\mathrm{t}}\right) \tag{48}$$

The new displacement function changes the Bessel function to $\mathrm{A} = \mathrm{J_n}(4\pi \mathrm{igR})$ and $\mathrm{B} = \frac{1}{2\mathrm{t}}$ and the delta functions into $\delta(\mathrm{s} + \mathrm{n}/2\mathrm{t}) + \delta(\mathrm{s} - \mathrm{n}/2\mathrm{t})$. Therefore, the resultant wave function is

$$\Phi(\mathrm{s}) = \frac{\mathrm{i}\pi}{\xi_\mathrm{g}}\left[\mathrm{J}_0(4\pi \mathrm{gR})(\exp(\pi \mathrm{is}\omega) + \exp(-\pi \mathrm{is}\omega))\frac{\sin\left(\pi \mathrm{s}\left(\frac{\mathrm{t}}{2}\right)\right)}{\pi \mathrm{s}}\right] \tag{49}$$

$$+\frac{\mathrm{i}\pi}{\xi_\mathrm{g}}\left[\sum_1^{+\infty}(\mathrm{i})^\mathrm{n}\mathrm{J_n}(4\pi \mathrm{gR})(\exp(\pi \mathrm{i}(+\mathrm{q})\omega) + \exp(-\pi \mathrm{i}\,(-\mathrm{q})\omega))\frac{\sin\left(\pi(+\mathrm{q})\left(\frac{\mathrm{t}}{2}\right)\right)}{\pi(+\mathrm{q})}\right]$$

$$+\frac{i\pi}{\xi_g}\left[\sum_1^{+\infty}(i)^n J_n(4\pi gR)(\exp(\pi i(+q)\omega)+\exp(-\pi i\,(-q)\omega))\frac{\sin\left(\pi(-q)\left(\frac{t}{2}\right)\right)}{\pi(-q)}\right]$$

This equation is the same as Eq. 46 although $\pm q = s \pm nB$. Eq.39, Eq.46 and Eq. 49 are used to simulate the phase profile across the split HOLZ line in the following section. Since the bell-shape profile is the best fit for the experimental data (this is discussed in Section 3.1.2), the simulation is also implemented for some typical different parameters of **g** vector, R, t, which are effective inherent properties of the specimen. Another parameter related to the biprism misalignment is presented in Section 3.1.3.

3.1.2 Simulation and Graphs

Three atomic displacement profiles are plotted for the specimen thickness of 160 nm and R= 0.0325 nm. The corresponding simulated phase profiles are achieved for 008 HOLZ line. The plots are given in Fig. 13. The considered values are chosen due to the experimental results which are presented in

Chapter 4, since the analytical section is obtained after the experimental details of the technique were investigated. Regarding Fig. 13, the phase profiles are dissimilar for various atomic displacement profiles. The phase profile for a bell-shape displacement profile shows an extra broad peak in the center of the phase profile. In

Chapter 4 the experimental profile shows a proper fit with the simulated phase profile coming from a bell-shape atomic displacement profile.

One of the major challenges in this work was fitting the simulated profile with the experimental profile due to the lack of a fitting parameter. So it was necessary to study the effect of some effective parameters in the phase profile such as t, R and **g**. This study is reported in the following sections.

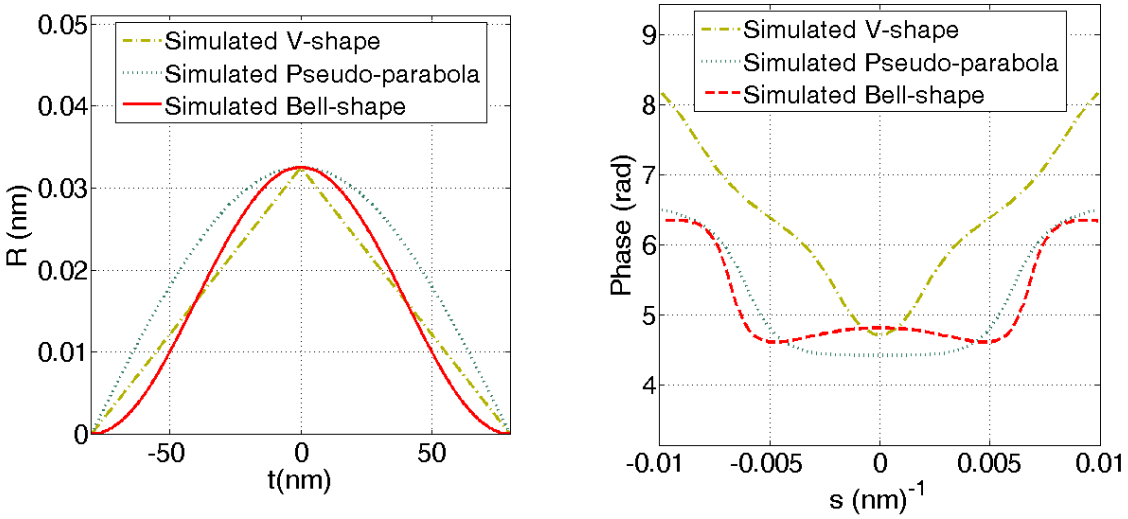

(a) (b)

Fig. 13- (a) the displacement profiles through the thickness of the crystal, (b) the simulated phase profiles for the corresponding displacement profiles [27].

3.1.2.1 Phase sensitivity to parameters

To recall Eq. 22 and Eq. 23, the SIS-HOLZ image wave function is the sum of two contributions, one is the beam coming from the left side of the biprism, S_1, and the other comes from the right side of the biprism, S_2 . Each carries the following phase terms of

- The biprism deflection angle, $\exp(\pm 2\pi i \mathbf{K}_B \cdot \mathbf{r})$.

- The biprism displacement factor $\exp(\pm 2\pi i \mathbf{K}_B \cdot \mathbf{r}_B)$, where $\mathbf{r}_B$ denotes the coordination of a generic point on the biprism axis.
- The pre-field (pre-specimen lenses) and the post-field (post-specimen lenses) spherical aberration and defocus.
- A rigid displacement, $\mathbf{K}_T$, due to the other deflecting stages rather than the biprism and specimen which is introduced to the image wave function by the microscope transmission function.

These extra phase factors complicate the SIS-HOLZ wave solutions. As it is mentioned previously, by adjusting the biprism in the middle of the split parallel with the HOLZ line and assuming an ideal imaging (aberration free imaging), the second and the third items can be neglected in the simulation. The fourth item is also identical for both interfering diffracted beams. So, it can be removed from the resultant wave equation. Therefore, considering a constant angle of deflection, α_B, the only contributing parameter in the phase calculation is the extra phase factor due to the displacement profile, $\exp(2\pi i g R f(z))$. The phase profile varies for different $|\mathbf{g}|$, R values, and t which is reported in the following sections.

3.1.2.2 Atomic Displacement Amplitude, R

The phase sensitivity to the atomic displacement amplitude, R, is shown in Fig. 14. Regarding Eq. 5, R is in the phase factor of the diffracted electron beam. For the same 008 HOLZ line when R=0 there is no displacement and the phase profile shows a flat line at 2π . By increasing the displacement amplitude when considering the constant thickness of 160 nm, a broad peak appears at the center of the phase profile and it grows while R increases from 0.01 nm up to 0.05 nm. Conceptually, this corresponds to a higher split width. At $R = 0.01$ nm the peak maximum is at 1.51π which goes higher up to 1.82π at $R = 0.05$ nm. The change in the peak height $\text{from } R = 0.01 \text{ to } R = 0.05$ nm is increasing, although it is not linear, Fig. 15.

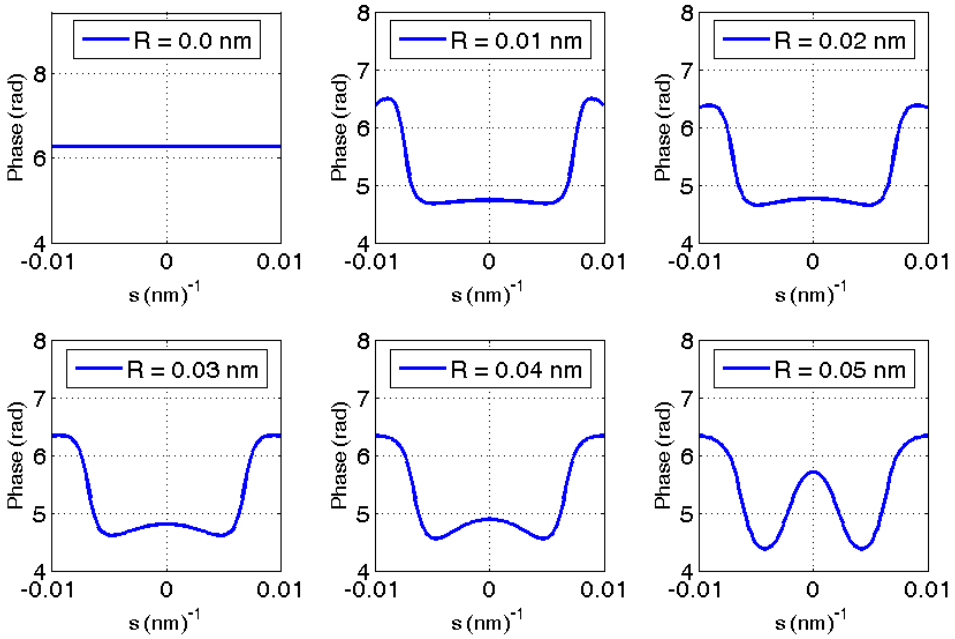

Fig. 14- Phase profile sensitivity to the atomic displacement amplitude shows a broader peak with shorter height for smaller R. The only variable in the plotted profiles is R [64].

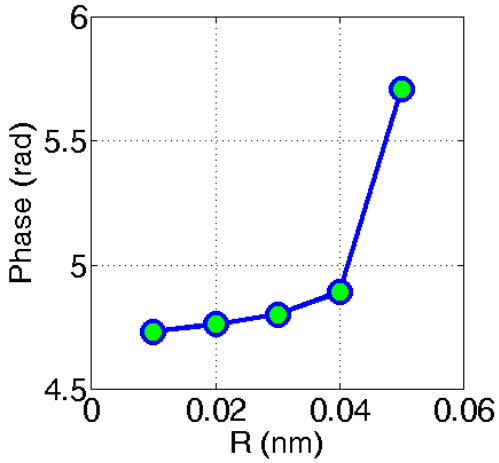

Fig. 15- The central broad peak maximum changes versus the atomic displacement amplitude variation from 4.74 rad to 5.71 rad. Although R is increasing linearly, the phase does not change linearly.

3.1.2.3 Reciprocal Lattice Spacing, |g|

By moving the probe towards or away from the interface, due to the lattice mismatch the lattice constant varies away from the interface. However, this has a

negligible effect on the shape of the phase profile and the height of the central broad peak. Various lattice constants considering Si, Ge and different compositions of $Si_{1-x}Ge_x$ are examined but no distinguishable changes were appeared in the profile. Instead, the phase profile is significantly influenced by the absolute value of the **g** vector. $|\mathbf{g}| = 1/d$ directly affects the central broad peak height. d is the interplanar spacing. The higher the absolute value of the **g** vector, the higher the peak height. However, no change is observed in the shape of the phase profile, Fig. 16. The split HOLZ lines with smaller **|g|** shows broader central peak with a shorter height. No difference was observed in the phase profiles simulated for i.e. $\bar{7}59$ and $75\bar{9}$. For the simulations in this section typical HOLZ lines in CBED pattern of Si are chosen.

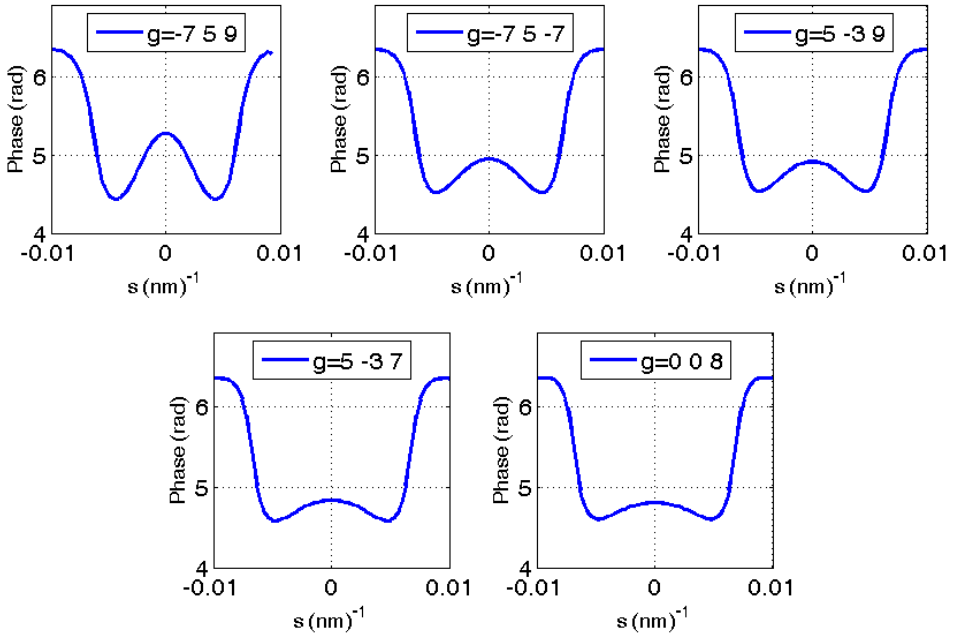

Fig. 16- The phase profile sensitivity to **|g|**. The profiles are plotted for the constant thickness of 160 nm and maximum atomic displacement of 0.03 nm **[64]**.

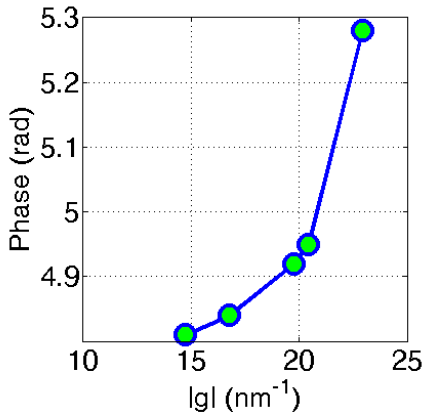

Fig. 17- The central broad peak maximum changes versus|**g**|. Both the central peak height and the absolute value of the **g** vector are not changing linearly.

3.1.2.4 The Specimen Thickness, t

In this section the phase profiles are all simulated for 008 HOLZ line considering the $Si_{0.8}Ge_{0.2}$ lattice constant and at constant displacement amplitude of 0.03 nm. The simulations are presented in Fig. 18. As shown, the central peak height in the phase profile decreases by increasing the specimen thickness from 150 nm to 200 nm. The thickness values are chosen according to the experimental thickness variation measured in the fabricated specimen. The specimen thickness results are reported in Section 4.3.2. The increasing thickness values are linearly related, although the central peak height does not show a linear reduction, Fig. 19.

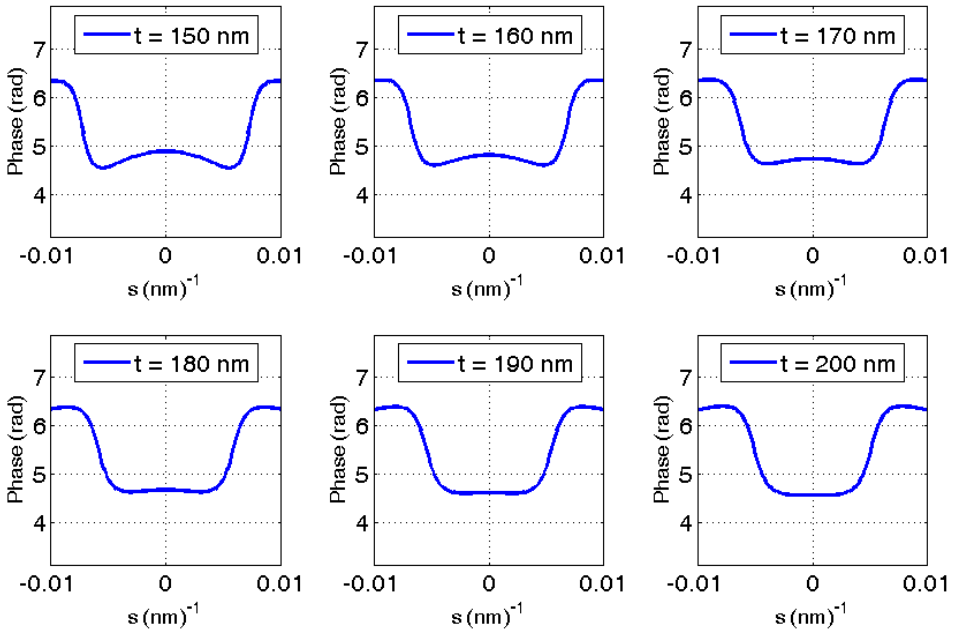

Fig. 18- The phase profiles for various thicknesses starting from 150 nm to 200 nm. The 50 nm deduction in the thickness decreases the central peak maximum from 1.53π to 1.45π **[64]**.

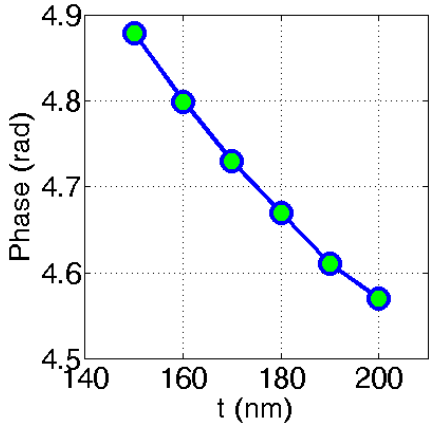

Fig. 19- The central broad peak maximum versus the thickness ranging from 150 nm to 200 nm. The linear reducing distribution of t does not show a linear change.

The phase change for various R, $|\mathbf{g}|$ and t are connected non-linearly in Fig. 15, Fig. 17 and Fig. 19. Since the major observable change to the phase profile happens at the center of the phase where s=0, in order to acquire the more accurate phase profile change for fitting the simulated phase profile with the experiment, Eq. 46 is rewritten at $s = 0$:

$$\Phi(\text{at s} = 0) = \frac{i\pi}{2\xi_g}[J_0(\pi gR)] + \frac{i\pi}{2\xi_g}\left[\sum_1^{+\infty}(i)^n J_n(\pi gR)\left(\exp(-\pi iq)+\exp(-\pi iq)\right)\right] + \frac{i\pi}{2\xi_g}\left[\sum_1^{+\infty}(i)^n J_n(\pi gR)\left(\exp(-\pi iq)+\exp(-\pi iq)\right)\right] \quad (50)$$

where $q = n/2 - 2\,(n/t)\alpha_B \mathbf{b}.\mathbf{r}$.

Using $\cos(x) = (\exp(-ix) + \exp(ix))/2$, Eq. 50 can further be simplified into

$$\Phi(\text{at s} = 0) = \frac{i\pi}{2\xi_g}\left[J_0(\pi gR) + 4\sum_1^{+\infty}(i)^n J_n(\pi gR)(\cos(\pi q))\right] \quad (51)$$

The real part of Eq.51 occurs at odd numbers of n while the imaginary part happens at even numbers of n. Therefore,

$$\text{phase}\left(\Phi(\text{at s} = 0)\right) = \tan^{-1}\left(\frac{J_0(A) + 4\sum_{n=\text{even}}(i)^{2n}J_n(A)(\cos(\pi q))}{4\sum_{n=\text{odd}}(i)^{n+1}J_n(A)(\cos(\pi q))}\right) \quad (52)$$

Eq. 52 is used to extrapolate the plotted profiles in Fig. 15, Fig. 17 and Fig. 19 for broader ranges of **R**, **|g|** and **t**. In Fig. 20 the highlighted points on the plots are the values studied in Fig. 15, Fig. 17 and Fig. 19.

Also, Eq. 52 is used to fit the simulated phase profile with the experimental phase profile (reported in Chapter 4) to achieve the correct R value and **R(**z**)** vector.

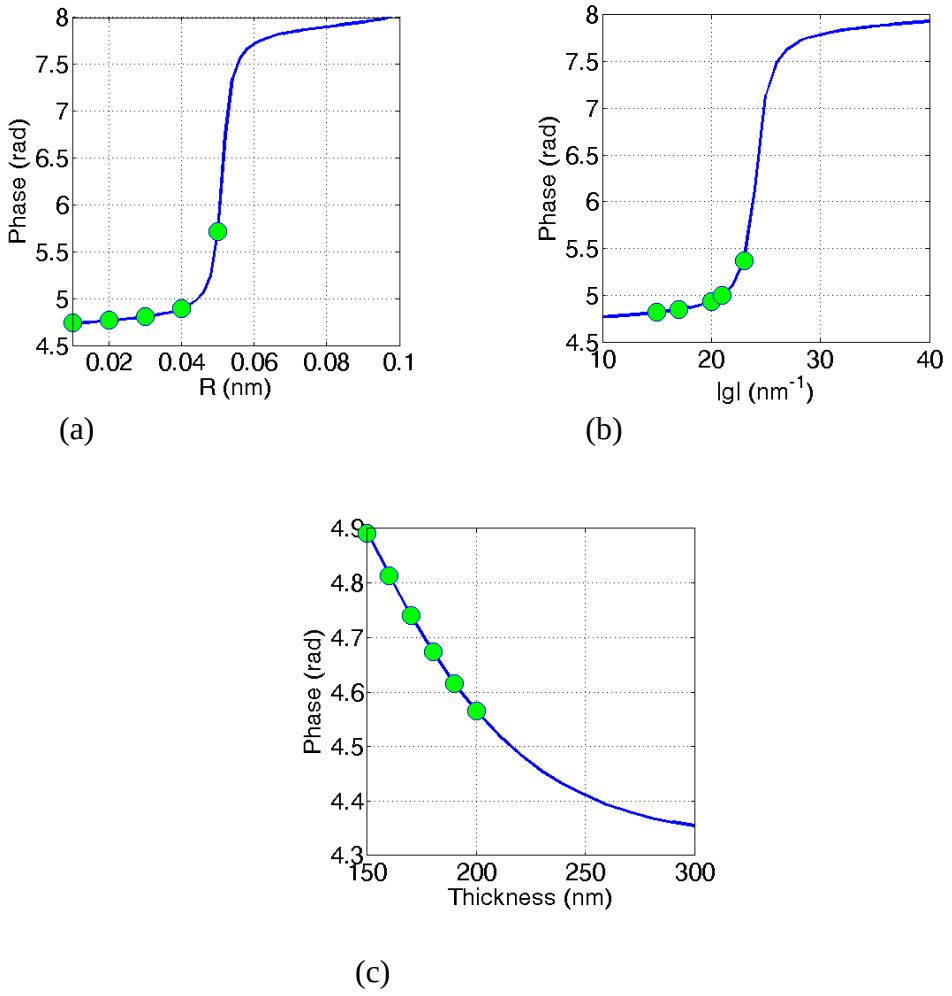

Fig. 20- The phase change at s=0 for various parameters of, (a) atomic displacement amplitude, R, (b) the magnitude of the **g** vector, |**g**|, (c) the thickness, t.

3.1.3 The Biprism Misalignment Effect

According to Fig. 21(a) the electrostatic biprism consists of a charged wire, B, whose axis is coincident with the y direction. The wire is placed between two earthed plates. The electrons with respect to their position with the wire are not equally affected by the distributed potential. This phase factor is added to the electron beam phase as $T_B(\mathbf{r_B}) = \exp(-2\pi i\,(\alpha_B/\lambda)\,|\mathbf{r_B}\cdot\mathbf{b}\,|)$ to comprise the mentioned effect. $\mathbf{r_B} = x_B\hat{\mathbf{i}} + y_B\hat{\mathbf{j}}$ is previously introduced as the coordination of a point on the biprism plane. Its dot product with the unit vector of the biprism eliminates the $\hat{\mathbf{j}}$ component. x_B is the horizontal distance of the charged particles from the biprism and y_B is the vertical distance of the

charged particles from the biprism. Also, $\hat{\mathbf{i}} = \mathbf{b} = [1\ 0]$ and $\hat{\mathbf{j}} = [0\ 1]$ are the vectors of the coordinate system and $\hat{\mathbf{i}}$ is perpendicular to the biprism.

When the biprism is symmetrically aligned in the middle of two interfering sources, the whole phase factor including the biprism deflection angle and the biprism position added to the beams passing the right and the left sides of the biprism are $+\exp(-2\pi i\,(\alpha_B/\lambda)\,\mathbf{b}\cdot(\mathbf{r}-\mathbf{r_B^R})$ and $-\exp(-2\pi i\,(\alpha_B/\lambda)\,\mathbf{b}\cdot(\mathbf{r}-\mathbf{r_B^L})$ respectively, where $|r_{Bx}^R| = |r_{Bx}^L| = |r_{Bx}|$. R and L show the right and left side of the biprism respectively. Therefore, in the case of a symmetric alignment of the biprism, the phase shift added to the beam passing the right and the left sides of the biprism are equal. When the biprism is displaced, such as Fig. 21(b), the added phase shift to the beams passing the right and the left sides are not equal since $|r_{Bx}^R| \neq |r_{Bx}^L|$ [65].

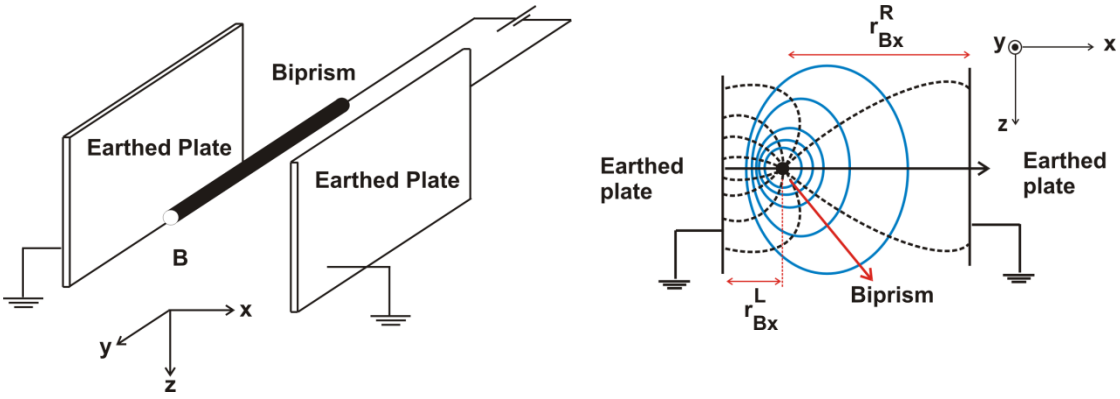

(a) (b)

Fig. 21- (a) The elements of an electron-optical biprism. It includes a rotatable wire in the center and two fixed earthed plates, (b) Potential (solid) and field (dashed) distributions of the electrostatic field due to an asymmetric charged line between two earthed plates **[65]**.

Therefore, in the case of a misaligned biprism in the SIS-HOLZ technique with a rotated biprism in the xy-plane (the biprism plane), a generic coordination system must be defined to find the horizontal distances to the biprism axis (Fig. 22). While the biprism is rotated by an angle of ω_B, the horizontal distances in the rotated frame, $r_B'^R$ and $r_B'^L$, can be expressed via a rotation 2×2 matrix.

$$\begin{bmatrix} r'_{Bx} \\ r'_{By} \end{bmatrix} = \begin{bmatrix} \cos\omega_B & -\sin\omega_B \\ +\sin\omega_B & \cos\omega_B \end{bmatrix} \begin{bmatrix} r_{Bx} \\ r_{By} \end{bmatrix} \tag{53}$$

Considering $r^R_{Bx} = -r^L_{Bx} = \pm r_{Bx}$ and $r^R_{By} = r^L_{By} = r_{By}$

$$\mathbf{r'^R_B} = \left[\cos\omega_B r_{Bx} - \sin\omega_B r_{By}\right]\hat{\mathbf{i}}' + \left[\sin\omega_B r_{Bx} + \cos\omega_B r_{By}\right]\hat{\mathbf{j}}' \tag{54}$$

$$\mathbf{r'^L_B} = \left[\cos\omega_B r_{Bx} - \sin\omega_B r_{By}\right]\hat{\mathbf{i}}' + \left[+\sin\omega_B r_{Bx} + \cos\omega_B r_{By}\right]\hat{\mathbf{j}}' \tag{55}$$

At $\omega_B = 0$, $r'^R_B = r'^L_B = r_B$. In a misaligned biprism the extra phase shifts added to $\Phi_g(S_2)$ and $\Phi_g(S_1)$ to produce the resultant wave function are Eq.56 and Eq. 57, respectively;

$$T_B\left(\mathbf{r'^R_B}\right) = +\exp(-2\pi i\,(\alpha_B/\lambda)\,\mathbf{b}' \cdot \left(\mathbf{r} - \mathbf{r'^R_B}\right) \tag{56}$$

$$T_B\left(\mathbf{r'^L_B}\right) = -\exp(-2\pi i\,(\alpha_B/\lambda)\,\mathbf{b}' \cdot \left(\mathbf{r} - \mathbf{r'^L_B}\right) \tag{57}$$

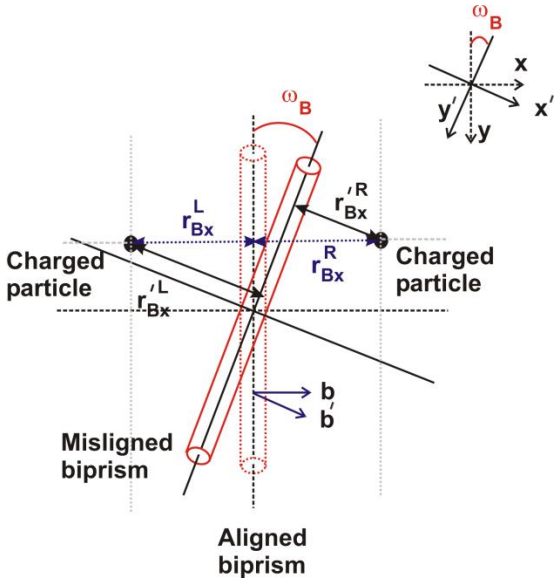

Fig. 22- Comparing the horizontal distances of the beams passing the left and right sides of the biprism with the biprism in an aligned and misaligned configuration. $|r'^R_{Bx}| \neq |r'^L_{Bx}|$ are the new horizontal distances of the charged particles to the biprism.

b and b' have already been defined as a unit vectors always perpendicular to the biprism axis. Therefore, the dot product of $\mathbf{b}' \cdot \hat{\mathbf{j}}'$ is always zero. In Eq. 54 and Eq. 55 the

$\hat{\mathbf{j}}'$ components of $\mathbf{r'^{R}_{B}}$ and $\mathbf{r'^{L}_{B}}$ are eliminated. Accordingly, $r'^{R}_{Bx} = \cos\omega_B r_{Bx} - \sin\omega_B r_{By}$, $r'^{L}_{Bx} = +\cos\omega_B r_{Bx} - \sin\omega_B r_{By}$ and the phase shifts added to the beams passing the right and the left sides of the biprism are different because of $|r'^{R}_{Bx}| \neq |r'^{L}_{Bx}|$. Hence, the added phase shifts to both wave functions are not symmetric and it is expected to obtain an asymmetric phase profile. The phase profiles are simulated for 008 HOLZ line, R=0.03 nm and $t = 160$ nm while ω_B changes in Fig. 23.

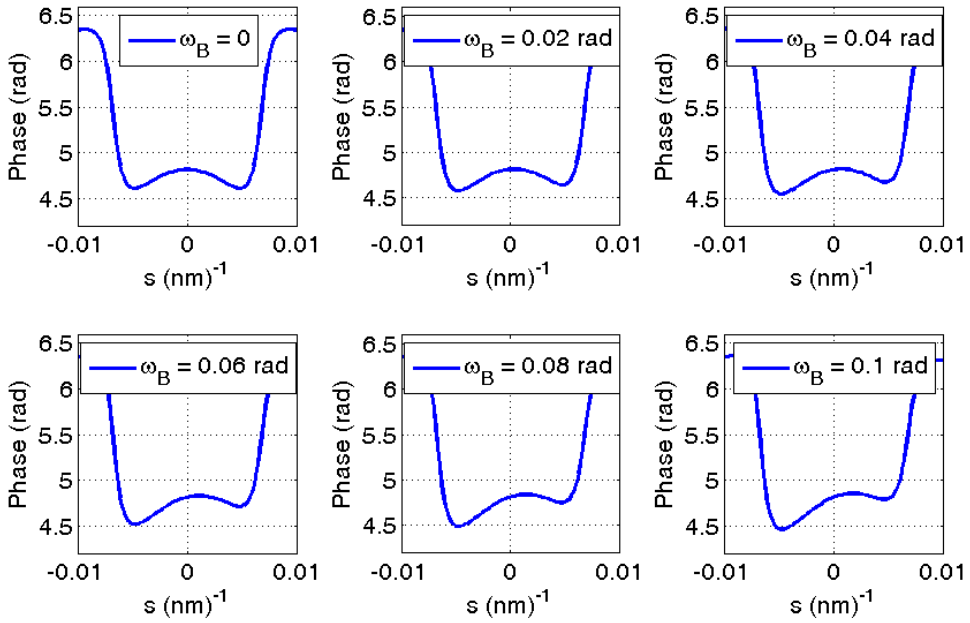

Fig. 23- The effect of the biprism misalignment on the symmetry of the phase profile. $\boldsymbol{\omega_B}$ is the angle of the biprism rotation.

In next chapter, the specimen fabrication, the thickness measurement and the experimental procedure and the results of the SIS-HOLZ line are presented.

Chapter 4

Experiment, Results, and Discussion

This chapter covers the SIS-HOLZ experimental details and results. The first step in transmission electron microscopy (TEM) techniques is to have an electron transparent specimen. In this work the specimen is fabricated from a bulk sample. Since the specimen is used for the displacement measurement purposes using a diffracted beam interferometry based technique, some considerations are always required in the specimen fabrication. In the following section the details of fabricating a specimen for the SIS-HOLZ technique are presented.

4.1 Specimen Fabrication

The industrial bulk sample in this work was a wafer of superlattices of $Si/Si_{0.8}Ge_{0.2}$ on a Si substrate. The molecular beam epitaxy (MBE) growth direction was unknown. Therefore, before cross-sectioning the sample, the growth direction, and the number of superlattices in addition to the superlattices thickness were studied using a High Resolution X-Ray Diffraction, Bruker HRXRD-D8 DISCOVER. The XRD experiments revealed [001] as the growth direction. The Si cap layer was investigated to be 40 nm thick with roughly > 15 layers of $Si/Si_{0.8}Ge_{0.2}$ superlattices having the thickness equivalent to $5.8\,\mathrm{nm}$ and Si barriers with the thickness of $12.8\,\mathrm{nm}$. The exact number of quantum wells is finally found using STEM images which is reported in Section 4.3.

The ROI in this work was in the Si substrate close to the interface which experiences the lattice mismatch strain between Si and $Si_{0.8}Ge_{0.2}$. The goal is to measure the z-dependent atomic displacement while z axis is considered parallel to the electron beam direction. A specimen cross section was fabricated using the in situ liftout method by a focused ion beam (FIB) machine. This is a technique used particularly in the semiconductor industry and materials science for the material removal [66, 67] . The FIB setup is very similar to scanning electron microscope (SEM), however the FIB uses a focused beam of ions. It is known as an efficient method in terms of time to fabricate TEM specimens with uniform thickness using a high energy gallium ion beam. The specimen fabrication using FIB leads to large uncertainties on the strain measurement and misinterpretation of data. Due to the formation of amorphous layers on the surface of the

thin specimen during the FIB, the results can be influenced either by reducing the diffraction pattern quality or by deforming the crystal [67].

To reduce the amorphous layer down to less than 10 nm on each side, the specimen fabrication either needs to be optimized or remove the damaged layer by ion milling. This modification differs for various materials and machines. The reported modified parameters in this work are obtained for superlattices of $Si/Si_{0.8}Ge_{0.2}$ on the Si substrate.

Before inserting the bulk sample into the FIB, the top surface was covered with 15 nm of a protective gold/palladium (Au/Pd) layer to reduce the possible ion beam induced damage and loss of the specimen's surface material. This was done by an Anatech Hummer VI (Au/Pd) sputtering system. In order to make a cuboid specimen of roughly 12-15 μm length by 2-3 μm width and 12-14 μm height from the bulk sample, the so called in situ liftout technique presented in the following section was used.

4.1.1 FIB In Situ Liftout Technique

The FIB machine used in this work was a single beam Hitachi FIB-2100, although a dual beam FIB machine is preferable in terms of time efficiency and a larger specimen tilt. The machine was equipped with the liquid gallium metal ion source to produce the ion beam and a tungsten deposition system. The machine had actuated TEM and SEM holder stages with a pick/place probe. Its nominal spatial resolution was 6 nm at 40kv. The magnification range was 700X to 200,000X and the maximum diameter of the bulk specimen that could fit in the SEM holder stage was 100 mm. The maximum current was 40 nA at 40 kV. Prior to the lift out, it was required to specify an area of interest and load the bulk sample into the SEM holder stage. A schematic of the final cross sectioned specimen was needed, knowing the orientation of the region of interest with respect to the ion beam in FIB and the electron beam in TEM. To make a uniform cross section specimen in terms of thickness, the FIB ion beam was chosen parallel to the growth direction, perpendicular to the surface, Fig. 24. Here, t shows the specimen thickness. Firstly, few microns of tungsten layer was deposited on the working area of $4 \times 30\ \mu m^2$. This step was necessary to protect the Si cap layer and superlattices from the gallium ion beam damage and loss of specimen material. Then four trenches using 40-0-300 beam

were milled on four sides of the tungsten coating. All FIB beams are characterised by three numbers, i.e. 40-0-300. The first number from left, 40, shows the voltage of the beam which here is 40 kV. The middle number, zero, explains if the condenser is on or off. So it can be either one as the lens is on or zero showing it is off. Finally the third number shows the diameter of the objective aperture. Hence, by choosing different values for the voltage, using the condenser lens and different objective aperture diameter we can have beams with different power good for either rough cuts or fine and neat final cuts. In Fig. 25, the secondary ion image of the tungsten coated area with the sketches of four rough cuts on four sides of the region of interest with the required cutting beams parameters is shown.

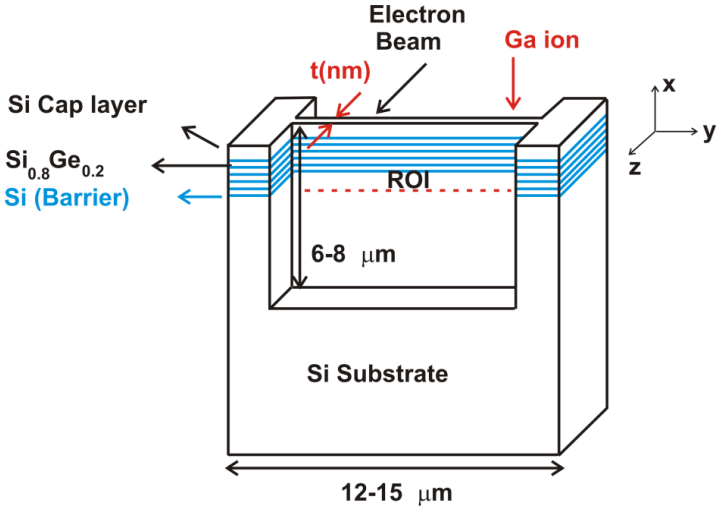

Fig. 24- A schematic of the TEM specimen. The ROI is shown by a dashed line. It is needed to have enough thin space under the superlattices to be able to scan the beam or tilt the specimen without blocking the electron beam by the thick areas **[27]**.

After the trenches were cut, the sample was tilted to do the other two final lift out cuts. The boxes in Fig. 26(a) were cut with 40-1-150 beam having a lower beam current comparing with 40-0-300. This was for the purpose of avoiding the re-deposition of the material and reattachment of the specimen to the bulk sample. Finally, the specimen was detached from every side except one, ready to lift out using the lift out probe, Fig. 26(b). The welding beam used for all the attachment steps was 40-0-80**.**

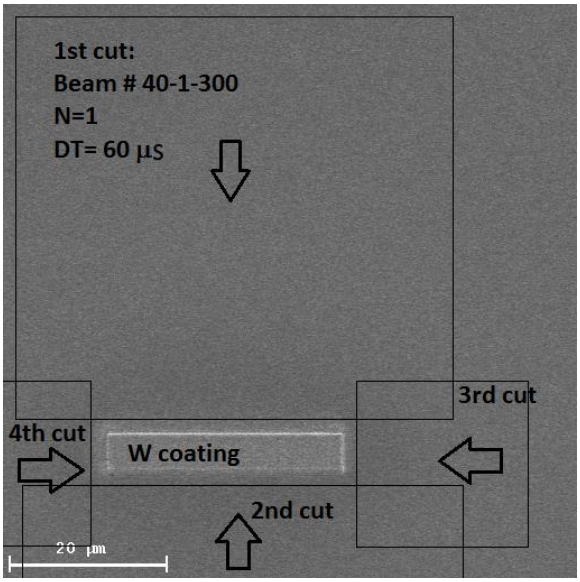

Fig. 25- The only difference between the sketched cuts are the direction of the beam to make trenches. N is the number of passes of the ion beam. DT is the dwell time which is the time that the beam stays on each point.

After the lift out, the specimen was attached to a FIB copper grid. The proper place for the specimen was on top of the post B on a 3 post coper grid, Fig. 27. This is suggested as an important consideration in the specimen fabrication to avoid the copper deposition on the specimen surface during the ion milling. One other challenge before attaching the specimen on the grid was flattening the bottom surface of the detached specimen and the top surface of post B to make a strong attachment on the grid. Weak attachment causes losing the specimen, due to instability of the specimen under the gallium ion beam in the FIB and the electron beam in the microscope. Generally, fabricating the specimen using the single beam Hitachi FIB-2100 was a time consuming and challenging step in the experimental routine. This was due to the instability of the lower voltage beams and the limited tilt of 40° in the machine.

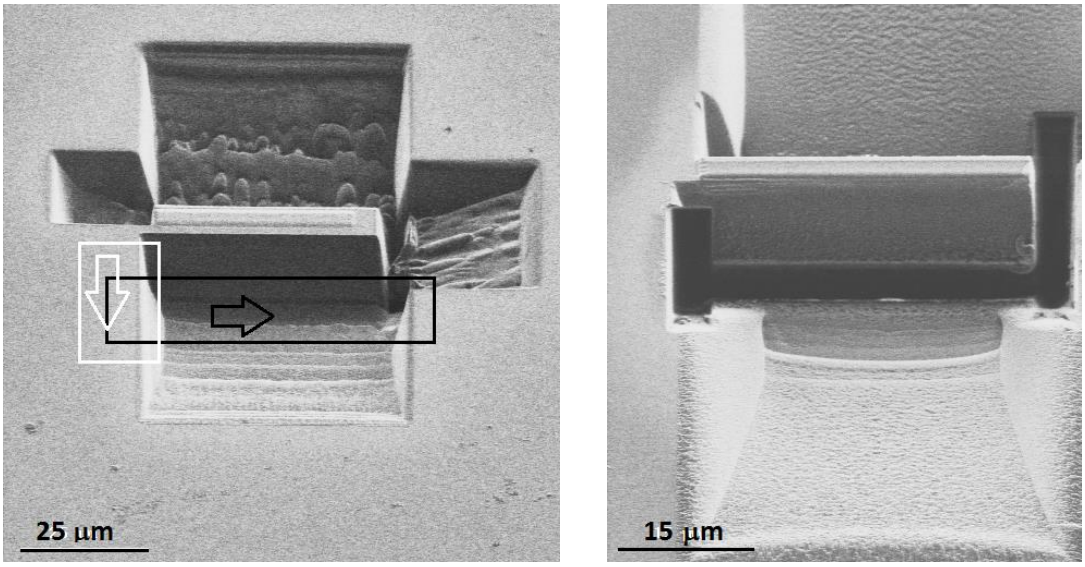

(a) (b)

Fig. 26- The secondary ion images of, (a) the fabricated trenches. The sample is tilted 40°. The sketched rectangles on the image show the final cuts before the lift out, (b) the specimen is ready to pick up. The FIB probe must be brought in from the top right side of the specimen.

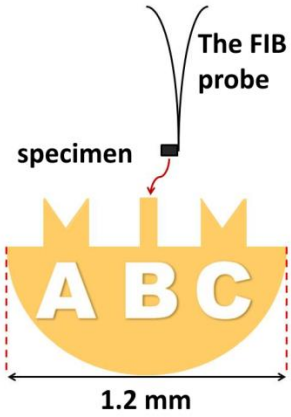

Fig. 27- A schematic of the FIB copper grid showing the probe attaching the specimen on top of the post B.

The final thinning cuts on the specimen attached to the copper grid, were done using 40-0-30 and 30-0-30 respectively on both sides of the specimen, although it is suggested to use a lower voltage beam of 8-20 kV for the final cut [67]. Every 10 kV energy adds ~10 nm damaged layer on the surface. So ~30 nm of damaged layer was assumed to exist on each surface of the specimen. To remove the induced damaged layer,

both thinned surfaces were ion milled after the FIB. The Ar^+ beam of the ion miller was set to a glancing angle of ±15 degrees with a 5μA current and a 3kV voltage. After milling each side for about 3-4 minutes, the specimen was cleaned to remove the surface radicals using a Hitachi UV Zone Cleaner for 10 minutes on each side. A good tactic found in the specimen making experiments is to fabricate multiple specimens on one copper grid. Not every experiment was successful. In appendix A. VI, some images of the failed specimens are shown. According to Section 3.1.2, the thickness effect on the phase profile is considerable. So, specimens with a uniform thickness were preferred for the SIS-HOLZ method. In either uniform or non-uniform specimens, the specimen thickness needs to be measured accurately since the thickness knowledge is important for a good fit of the experimental data and the simulation. In this work the specimen thickness was measured using electron energy-loss spectroscopy (EELS) which is explained in the next section. Besides, the theoretical development of this work is based on the kinematical simulation using the Howie-Whelan equation. So, multiple scattering effect is neglected. In order to satisfy this theory, the thickness of the specimen must fit below a predefined value relative to the extinction distance, ξ_g, which is reported in Section 4.3.2.

4.1.2 Specimen Thickness Measurement by Electron Energy-Loss Spectroscopy

When an electron beam passes through a thin specimen the elastic and inelastic scattering occur. Elastic and inelastic scattering are both due to the Coulomb interactions with the atomic nucleus and the electron cloud. The original electron will be deflected through an angle or it will go straight through the nucleus. The larger the angle of scattering, the bigger the energy loss. Inelastic scattering involves the loss of energy of the original electron beam through producing quasi particles such as phonons and plasmons. Thus, the electrons are separated by their kinetic energies to produce EELS spectrums.

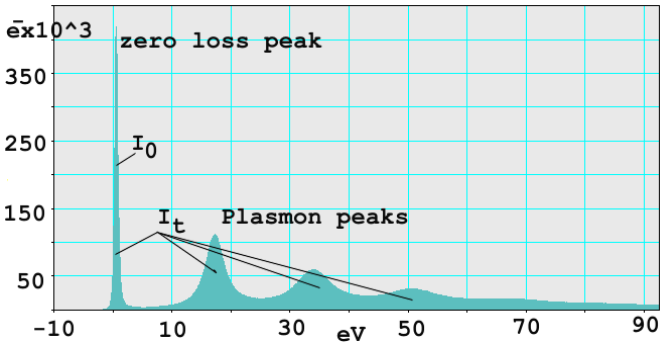

Fig. 28- An EELS spectrum taken of the Si substrate from one of the fabricated specimen.

In a typical energy- loss spectrum there are three main sections, Fig. 28:

- Zero loss peak
- Low loss region (5-50 eV)
- High loss region (Not shown in Fig. 28)

The low loss region is included in the elastic scattering of the outer shell electrons. Plasmon oscillation occurs most frequently in the range of 5 eV to 50 eV. The number of plasmon peaks is directly related to the thickness. In order to calculate the thickness of the specimen using EELS spectrum Eq. 58 can be used.

$$t = \lambda \ln(\frac{I_0}{I_t}) \quad (58)$$

Here, t is the thickness and λ is the mean free path of the electron in the specimen (appendix A. VII). I_0 is the intensity of the zero loss peak and I_t is the total spectrum intensity. The mean free path is the average distance that one electron travels in the material between inelastic events. It depends on the electron energy of the beam and the atomic number of the material. The mean free path for Si was calculated using the EELS interface. It needs the knowledge of the material properties, the accelerating voltage and the semi-collection angle of the beam. Theoretically, considering 200 kV as the voltage, 3 mrad as the semi-collection angle and 14 as the atomic number for Si, mean free path is 162 nm, however since the objective aperture was not used, the semi-collection angle was considered as 50 mrad. Therefore, the mean free path for Si was calculated as ≈ 88 nm. The output of EELS technique is an spectrum of $\ln(\frac{I_0}{I_t})$ versus length in nm which gives

the thickness variation. For this purpose, an area of roughly $\approx 75 \times 100\ \mathrm{nm}^2$to $75 \times 120\ \mathrm{nm}^2$ was chosen on each specimen to obtain the thickness variation in each specimen. The calculated thickness values are presented further in Section 4.3. Due to the thickness results, the most uniform specimen, (specimen 1 and specimen 2 ≈ 166 nm) were picked to conduct the SIS-HOLZ experiment which is presented in the following section.

4.2 SIS-HOLZ Experimental Procedure

For the SIS-HOLZ experiment in this work the Hitachi HF-3300v STEHM (Scanning Transmission Electron Holography Microscope) having spherical plus Coma aberration correction of its TEM mode operating at 200 kV was used. This microscope is equipped with:

- A high coherence, high stability and high brightness field emission electron source.
- A rotatable electron biprism in the selected area aperture plane. Its biprism was a thin wire of quartz covered with gold having a diameter of 0.35 μm with 2 mm length. It could move in both x and y directions (x: ±1 mm, y: ±1 mm) plus a 360^o in-plane rotation enabling the biprism to be easily aligned parallel to any split HOLZ line.
- Electron energy loss spectrometer, EELS.
- A Gatan Ultrascan 2K×2K CCD camera and an imaging energy filter GIF 2K×2K camera using zero loss electrons were used to record the interference patterns. A 10 eV energy slit was used to help with removing the background noise and increase the fringe contrast. The importance of the fringe contrast in the phase noise will be discussed further in this chapter.
- High stability single and double tilt holders (Hitachi). In this work, the copper grid holding the specimen was held in a double tilt holder with $\pm 15\ °$ tilt.

The simplified schematic of the SIS-HOLZ method is presented in Fig. 11. After aligning the beam in both imaging and diffraction mode, the first step in this method was to get a CBED pattern in the TEM mode including HOLZ lines. By selecting “spot” on

the TEM manual controller the scanning in the STEM mode can be stopped. To get a focused image, a region far from the interface was picked, after adjusting the specimen height and focusing the image, it was only required to switch to the diffraction mode. A CBED pattern was visible on the screen. The magnification of the CBED pattern and the disk size can be changed respectively by the camera length and the probe size. So by adjusting the probe size and the camera length, the details of the 000 CBED disk can be observable. Looking for a zone axis (ZA) is always needed to find out the orientation of the beam with respect to the crystal specimen and index the diffraction pattern. However the ZAs are not proper places to conduct the SIS-HOLZ experiment. ZAs are busy places with the intersection of many diffraction planes and the dynamical diffraction effect increases at the intersections. So, it was preferred to find a major ZA first, i.e. 001, 011 or 111 and move along a Kikuchi band towards a minor ZA, i.e. 015 or to tilt around a Kikuchi band, i.e. 004 to find a region with fewer HOLZ lines and intersections. Fig. 29 shows a schematic map of Kikuchi bands and some major and minor ZAs in a diamond cubic crystal. The major ZAs which are busy while minor ZAs show fewer intersections of atomic planes. 001, and 011 ZAs were observed in the work.

This map helps to find ZAs by tilting the specimen with the angles of α and β (Fig. 30) to achieve the preferred CBED pattern and HOLZ line. i.e. at 001 ZA. It was preferred to move away along 400 to conduct the SIS-HOLZ experiment. Tilting the specimen changes the thickness. Due to the thickness effect on the phase profile, calculating the thickness at every tilt is required. This can be done either by repeating the EELS measurement or by recording the tilt (α and β) to calculate the new thickness. Either way, the primary knowledge of the specimen thickness in the ROI is required.

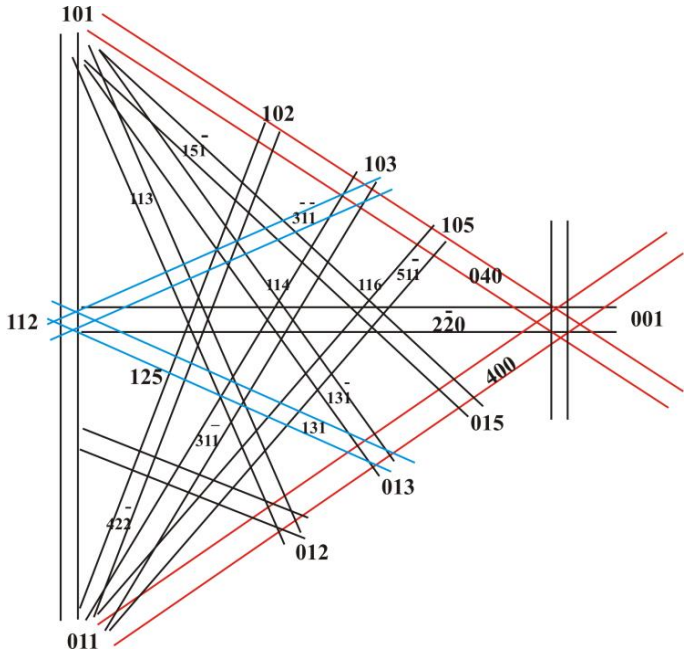

Fig. 29- A schematic of the Kikuchi bands in the fcc and diamond cubic crystal. This is a map in crystals which is helpful to understand the orientation of the crystal with respect to the beam. Kikuchi bands are used to travel through the reciprocal space.

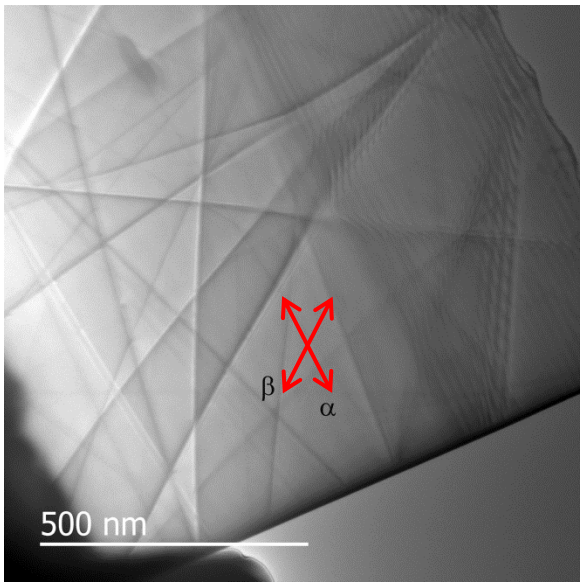

Fig. 30 – TEM image of a fabricated specimen with the thickness of ≈200 nm showing the direction of **α** and **β** tilt. By changing **α** and **β** it was possible to move between the ZAs or along a preferred Kikuchi band.

In 000 CBED disk some deficient HOLZ lines split when the beam approaches the strained interface whereas others remain as an unsplit line. Some splits are symmetric with respect to the center of the split and some are asymmetric. Also the intensity of the split HOLZ line decreases within the strained region and can disappear at the interface or inside the superlattices. Not all the split HOLZ lines can be used to conduct the SIS-HOLZ method. Finding the proper split HOLZ with high contrast was a big challenge. The size of the split also matters. Wider split gives finer fringes which help with the reconstruction steps. This is also discussed further in Section 4.3.

After picking a high contrast split HOLZ line, the biprism alignment within the split was required. Although the SIS-HOLZ is a diffracted beam interferometry based technique, the initial alignment of the biprism is usually done in the image mode. The biprism alignment included rotating the biprism until it is parallel with the HOLZ line and placing it in the center of the split. After the biprism alignment, the diffraction mode was again chosen. Some adjustment in the biprism alignment was needed to compensate for the electron rotation along the optical axis. After the biprism alignment, the specimen was slightly defocused (the biprism defocus, $Z_{OB} - Z_O$). This can be done by gradually changing the specimen height. As it is mentioned in Chapter 3, the biprism defocus, $Z_{OB} - Z_O$, helps to nearly focus the virtual sources, S_1 and S_2 on the plane Z_1 (Fig. 11). The biprism defocus varies in different TEMs due to the objective lens power. Also, due to the effect of the specimen tilt in the specimen thickness, a biprism defocus readjustment is usually required after tilting the specimen or moving the probe in a non-uniform thickness specimens.

Finding the split HOLZ line, the initial biprism alignment, and the biprism defocus was first done within the bright field (BF) 000 CBED disk, however the experiment was conducted in the dark field (DF) disk. The DF condition improves the contrast of the split HOLZ line and enhances recovery of the strain information on the specific crystalline plane by removing extra phase information that is present in the bright field disk of the CBED pattern. By working in the DF disk one can also more easily find areas along the split HOLZ line that have not been phase shifted by intersecting with other HOLZ lines. Also, the biprism alignment inside the split HOLZ line was easier in the DF rather than BF. Before self-interfering the split HOLZ line, for the biprism

alignment purposes, it was useful to apply a negative potential on the biprism to find the middle of the split. The interfering voltage was finally applied on the aligned and centered biprism to self- interfere the two halves of the split HOLZ line. The applied biprism voltage depended on the separation of interfering sources, S_1 and S_2, which is related to the split width and the biprism defocus, the biprism voltage varies to make a fully overlapped interference pattern where

$$\Delta s = |S_1| + |S_2| \propto 2\alpha_B(Z_{OB} - Z_O) \tag{59}$$

where Δs is the separation of sources. The source separation, Δs, is related to the split width. Higher deflection angle needs higher voltages of the biprism which gives finer fringes [56, 60];

$$\Delta = \frac{1}{2|K_B|\lambda(Z_{OB} - Z_O)} \tag{60}$$

where Δ is the fringe spacing on the diffraction plane, and λ is the electron wavelength. According to Eq. 59 and Eq. 60, wider split HOLZ line can give finer fringes. Additionally, increasing the biprism defocus will produce finer fringes.

Two CCD cameras were available for recording the interferograms. The GIF camera magnified the image of the interferogram by ~10 times with respect to the low resolution camera placed higher in the microscope's column resulting in a larger camera length. A large camera length helps to obtain more pixels per fringe, which increased the signal to noise ratio.

Finally, the interferogram needed to be reconstructed to determine its amplitude and phase. The phase information is necessary for measuring the atomic displacement profile along the path of the electron beam. The reconstruction steps of the digital phase image included:

- Fast Fourier Transform (FFT) of the interferogram,
- Filtering one of the side bands using a low pass filter centered on its carrier frequency, q_c.
- Inverse FFT of the filtered sideband

The reconstruction steps were performed using Holoworks, a DigitalMicrograph subroutine of Gatan. During the phase image reconstruction steps, in order to avoid the

overlap between the center band and two sidebands in the frequency space, the carrier frequency of fringes, q_c, must be three times larger than maximum spatial frequency, q_m, $q_c \geq 3q_m$, Fig. 31. The carrier frequency, q_c, is related to the fringe spacing in the hologram. Finer fringes give higher, q_c, and $\Delta \propto 1/q_c$. If the filter radius is smaller than 1/3 q_c, some of the phase information related to the strain will be missed. If it is larger than $1/3q_c$, the phase image will include information from the center band making it more complicated.

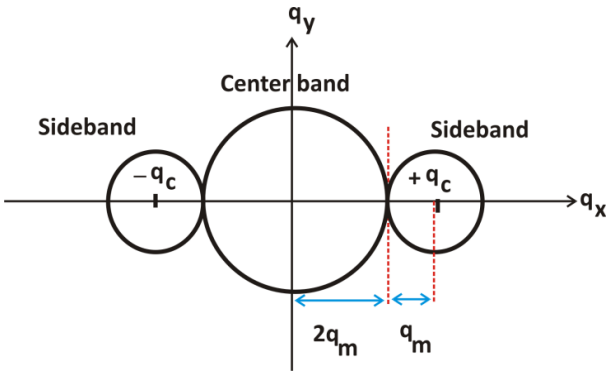

Fig. 31- A schematic of the frequency space during the reconstruction steps. This can be achieved by the FT of the interferogram. The filter size in the Fourier space must be at least $\approx \mathbf{q_m}$ **[27]**.

One extra step was found very helpful before reconstructing the phase image. A Gaussian filter was applied to the Fourier information to remove extra phase information due to the biprism, i.e., the defocused biprism creates Fresnel fringes that produce streaks in the Fourier image. An example of the results before and after Gaussian filtering the interferogram is presented in Section 4.3.5. Finally, the phase profile was obtained across the phase image of the split HOLZ line and compared with the simulated profiles.

4.3 Results and Discussion

4.3.1 Specimen Observation

Fig.32 shows the STEHM images of a good specimen with a uniform thickness. The cap layer and the superlattices are protected with the tungsten coating. Fig.32(b)

shows the period of $Si/Si_{0.8}Ge_{0.2}$ quantum wells is 25**.** The tungsten coating thickness is measured in Fig. 33 showing ~295 nm on the top surface.

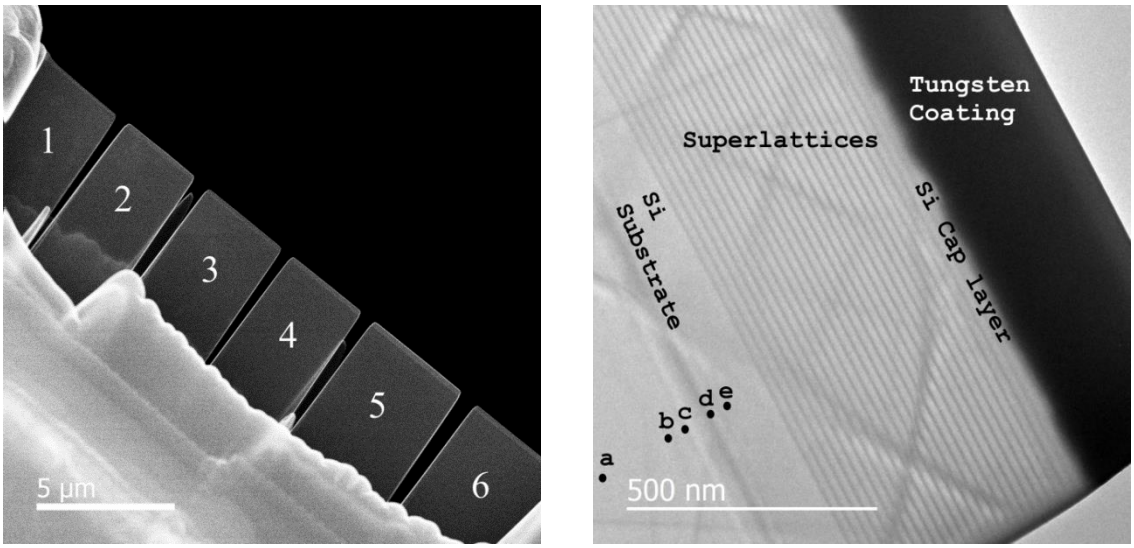

(a) (b)

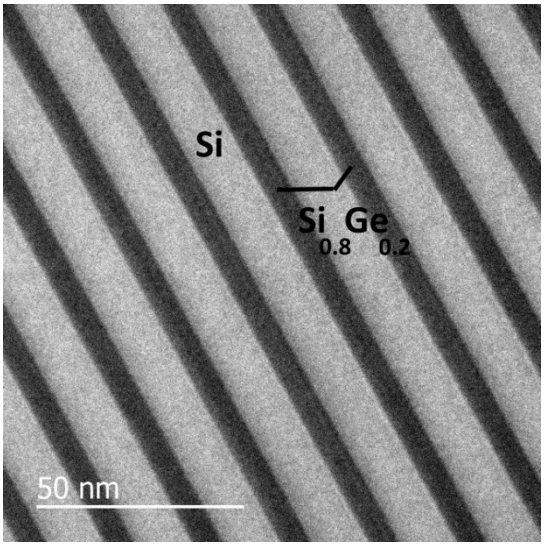

(c)

Fig.32- The STEM images of the final fabricated specimens, (a) Specimens 1 and 2 are electron beam transparent at 200 kV that some Si layers on the other side of the specimens can be seen, (b) and (c) high magnification STEM images of specimen 1 showing $Si/Si_{0.8}Ge_{0.2}$ Superlattices, Si capping layer and tungsten coating [27].

Comparing with HRXRD results shown schematically in Fig.9, the Si barrier thickness shows -7.5% deviation while $Si_{0.8}Ge_{0.2}$ thickness is +10.3% deviated. The interfaces are quite sharp and coherent as it is shown in Fig.32(c). The calculated misfit strain in Si substrate at its interface with $Si_{0.8}Ge_{0.2}$ is 0.781% (Using Vegard's Law to calculate $Si_{0.8}Ge_{0.2}$ lattice constant). Vegard's law gives the lattice parameter of a solid solution of two constituents such as A_xB_{1-x} as; $a_{A_xB_{1-x}} = xa_A + (1-x)a_B$.

The labels on Fig.32(b) are the ROIs for the CBED patterns taken further in Fig. 49 and Fig. 50.

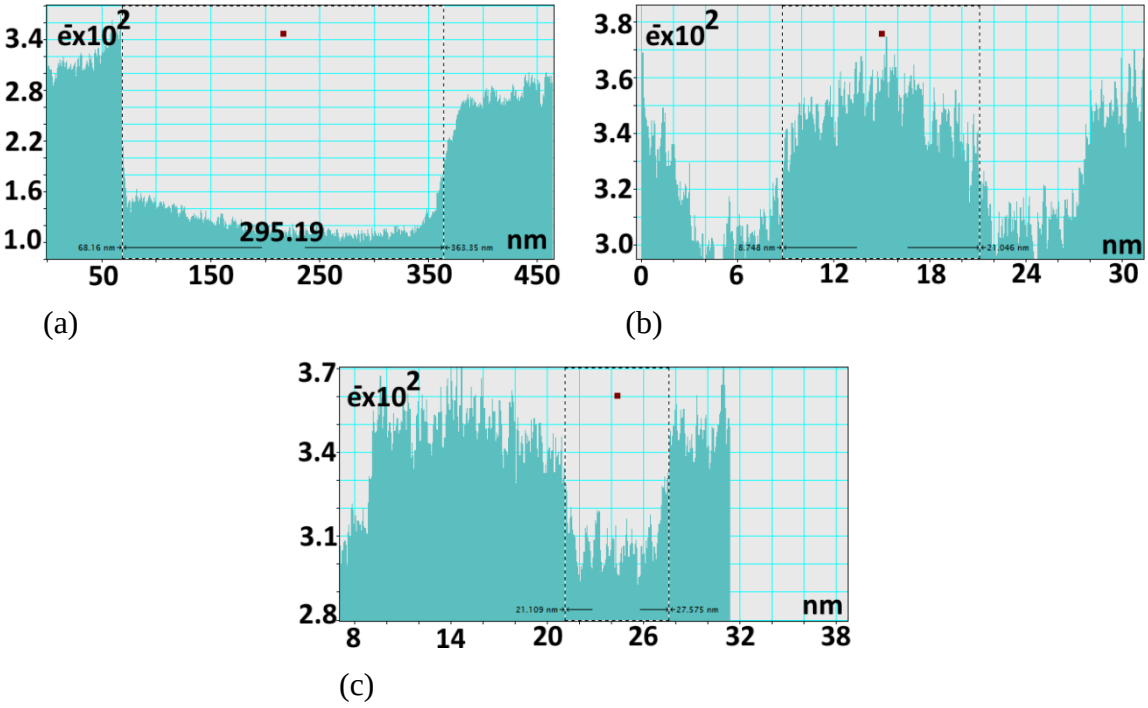

Fig. 33- The intensity profile across, (a) the tungsten region of the STEM image in Fig.32(c) showing the thickness of the tungsten coating and, (b) the Si barriers in the superattices and, (c) the $\mathbf{Si_{0.8}Ge_{0.2}}$ layers.

4.3.2 Specimen Thickness

According to Fig. 34 unlike specimen 3 to 6, Specimen 1 and 2 showed a uniform thickness. The thickness for fabricated specimens was calculated using Eq.58. The results are presented in

Table 2. Specimens 1 and 2 were favorable to conduct the SIS-HOLZ experiment due to the uniform distribution of thickness across a wide area of $75 \times 120\ nm^2$. Therefore, there was no need to repeat the thickness measurement during the experiment while moving the probe to find a wide split HOLZ line.

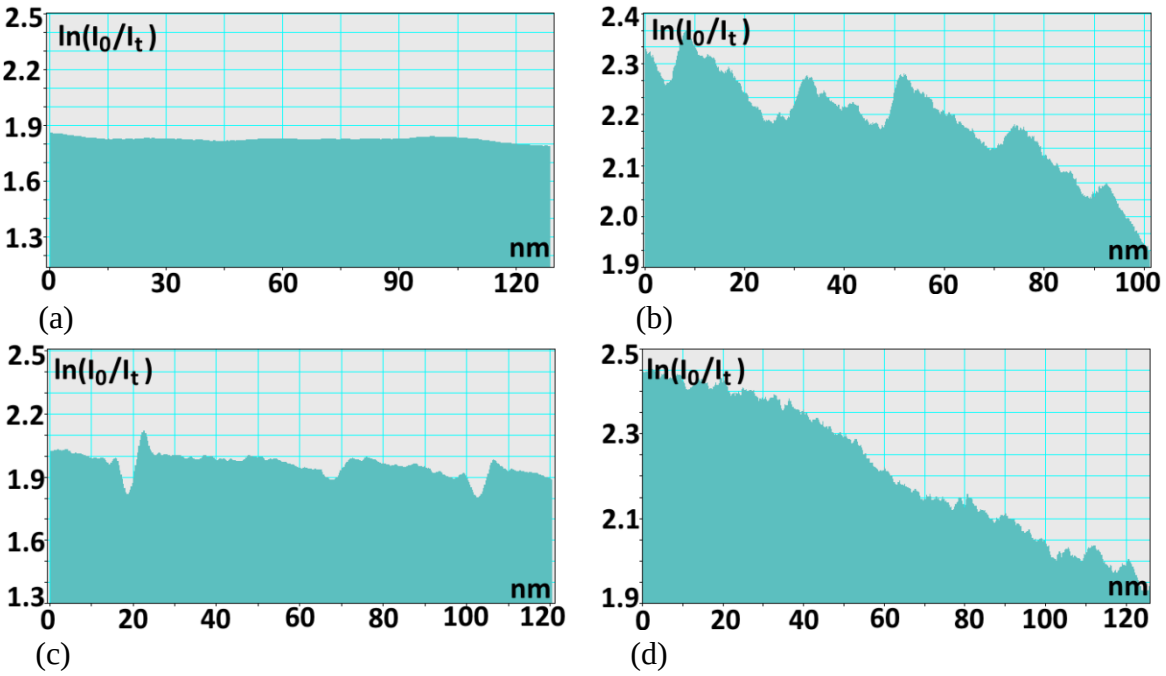

Fig. 34- Thickness variation spectrums. The vertical axis is $\ln(I_0/I_t)$ and the horizontal axis is the length of the studied area. The profiles are for, (a) specimens 1 (and for specimen 2 is also the same.), (b), (c) and, (d) specimens 3 to 6

Table 2- Thickness variation for 6 fabricated specimens using FIB in an area of $\approx 75 \times 100\ nm^2$ to $75 \times 120\ nm^2$.

specimen	$\ln(I_0/I_t)$	Thickness (nm)	Thickness variation (nm)
1 and 2	1.86-1.89	165	$\pm$ 1.32
3 and 4	1.79-2.03	168	$\pm$10.56
5	1.91-2.03	173	$\pm$5.28
6	1.93-2.36	188	$\pm$19.00

Also, many studies clearly shows that the kinematical approximation (Howie-Whelan formula) gives a fairly acceptable intensity profile across HOLZ lines as long as

the sample thickness is less than ξ_g/π [24, 43, 68]. In this work the SIS-HOLZ data quantification was performed on 008. Its extinction distance, ξ_{008}, in Si is 540 nm [43, 52]. Specimens 1 and 2 thicknesses are below 171 nm and allow using kinematical diffraction theory.

4.3.3 CBED Patterns

Regarding Fig. 35 in the diffraction mode by adjusting the probe size, the zero CBED disk diameter increases and its details such as the HOLZ lines become visible in the 000 CBED disk. In Fig. 35(c) the Kikuchi bands and the HOLZ lines can be seen in 000 CBED disk.

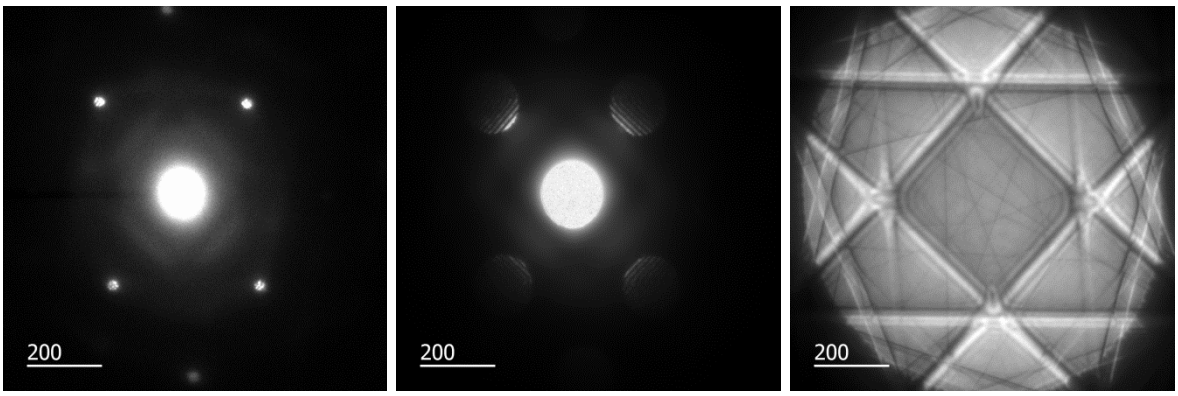

(a) (b) (c)

Fig. 35- 001, ZA, opening the electron probe changes the CBED disk size. By opening the probe from (a) to (c) the zero beam size in the CBED pattern increases. The diffraction pattern looks a little bit distorted.

Depending on the order of the HOLZ line which is related to their Bragg angle their intensity varies. The intensity of the HOLZ lines in 000 CBED disk are dissimilar due to their angle of Bragg. HOLZ lines with very high index come from higher Bragg angles called the 2nd and the 3rd order HOLZ lines. Comparing with the 1st order HOLZ line, the 2nd and the 3rd HOLZ lines have lower intensity in the 000 CBED disk. However, they have higher sensitivity to the atomic displacement. The 2nd or the 3rd order HOLZ line cannot be used in the SIS-HOLZ due to their lower contrast comparing with the higher intensity HOLZ lines. They split first but they disappear quickly by approaching to the strained region. By moving towards the interface the individual HOLZ

line split width increases due to the non-uniform misfit strain. The maximum atomic displacement through the specimen thickness, R, is relative to the split width, Eq. 35.

Fig. 36 shows 000 CBED disk taken at $\alpha = -5$ and $\beta = 10$ degrees from the 011 ZA along 400 Kikuchi band. The order of figures shows the distance of the electron probe from the interface of $Si_{0.8}Ge_{0.2}/Si$. Fig. 36 (a) was taken far from the interface where there is no strain and Fig. 36(i) was taken inside the superlattices which is highly strained. In 000 CBED disk of Fig. 36(a) there are both high contrast and low contrast individual HOLZ lines. Fig. 36 explains the split width change by moving the probe towards the interface due to the higher atomic displacement. Besides, HOLZ lines do not show the same sensitivity to the strained region. Therefore, the split width is not the same in every HOLZ line while approaching towards the interface. Some HOLZ lines do not split which they represent the invisible strained field i.e. the one which is shown by the red arrow line in Fig. 36. Regarding the extra phase factor of $\exp(2\pi i\mathbf{g}\cdot\mathbf{R}(z))$ and Eq. 35, while the **g** vector is parallel with the atomic displacement vector, **R**(z), the maximum split happens. When the **g** vector is perpendicular to **R**(z) no split occurs, although the strain is not zero. This is called invisible strained atomic plane. In 000 CBED disk multiple HOLZ lines can be seen which by approaching towards the strained regions of the specimen not only the HOLZ lines split but also the 000 CBED disk becomes noisy. To avoid interfering the other HOLZ lines intersections and the background noise which can lead to misinterpreting the phase profile, the SIS-HOLZ method was preferably conducted in the DF disk of the chosen split HOLZ line.

In the next section the intensity distribution in the BF disk and a DF disk are compared.

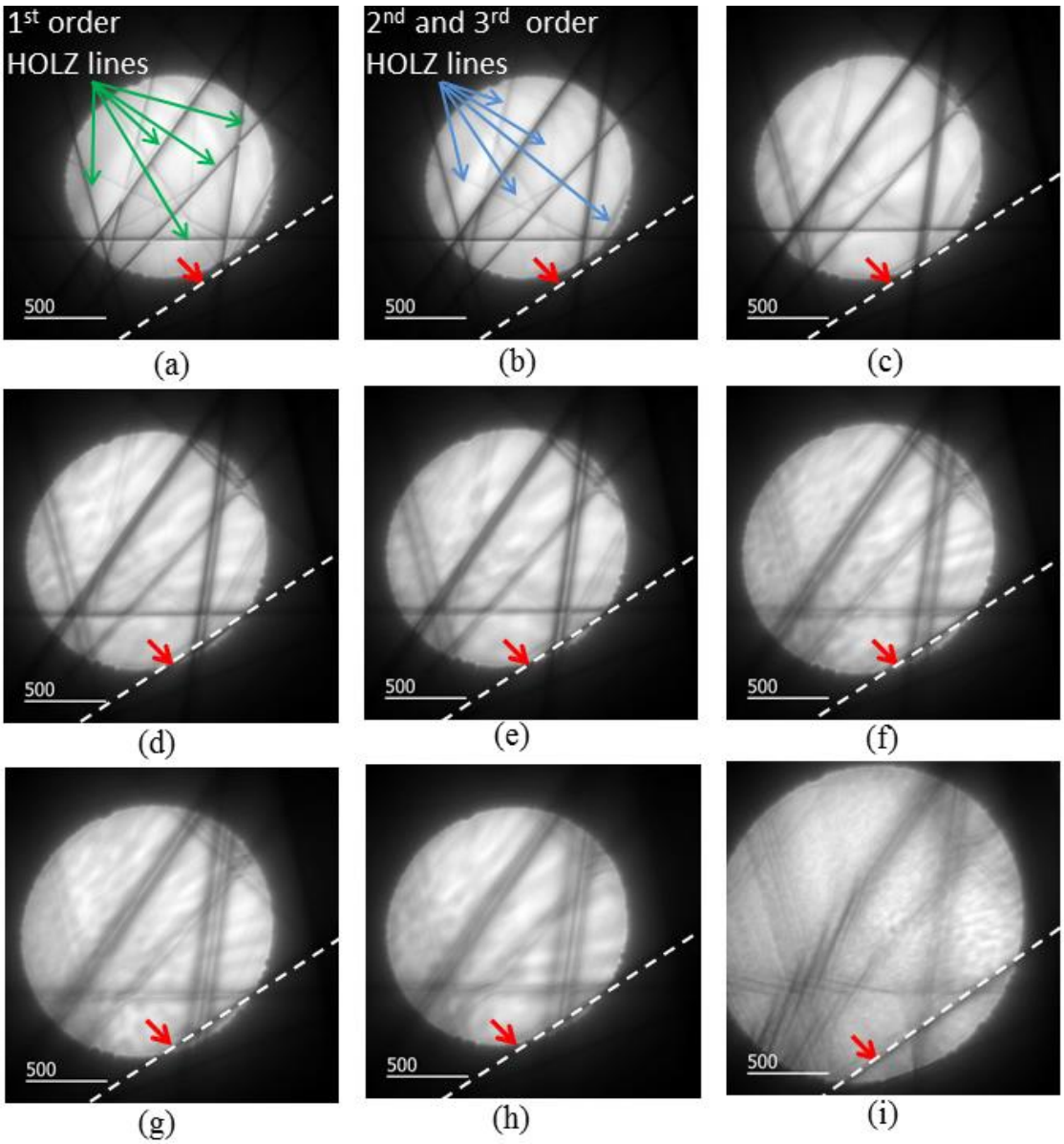

Fig. 36- The evolution of HOLZ lines from a non-strained region of the specimen towards the interface of $\mathbf{Si_{0.8}Ge_{0.2}/Si}$. Superlaticces, (a) individual HOLZ lines at $\mathbf{> 400\ nm}$ away from the interface, (b),(c) HOLZ lines starts to spread at $\mathbf{350 - 300\ nm}$, (d) split starts at $\mathbf{\approx 270\ nm}$, (e) at $\mathbf{\approx 250\ nm}$, (f) at $\mathbf{\approx 190\ nm}$, (g) split HOLZ line with internal intensities at $\mathbf{\approx 170\ nm}$, (h) at $\mathbf{\approx 120\ nm}$, (i) complicated pattern inside the superlattices. The red arrow shows a white dashed line. This is an individual HOLZ line staying unchanged by moving towards the interface.

4.3.4 Dark Field and Bright Field Disks HOLZ line

HOLZ line come into pairs. One in the bright field disk, deficient line, and one in dark field disk, excess line. Fig. 37(a) shows two distinct excess and deficient split HOLZ lines. The rocking curves across the split HOLZ line 1 are obtained, Fig. 37(b-e). The rocking curves show the same trends in both 000 CBED disk and in the DF disk, Fig. 37(b) and Fig. 37(c). Intensity profiles in both BF and DF disks in Fig. 37(c) and Fig. 37(d) show a noisier background in 000 CBED disk. By moving the probe towards the interface some splits became asymmetric, Fig. 38. Also the number of recorded electrons, N, shows 40% reduction, from $\geq 3 \times 10^3 e^-$ to $\approx 1.8 \times 10^3 e^-$.

According to Eq. 35, the asymmetric split HOLZ line can either be due to the thickness change or the angle variation between R(z) and g vectors. R(z) and g vectors orientation can be due to the non-uniform distribution of an inhomogeneous atomic displacement in terms of orientation, which corresponds to an asymmetric distribution of R through the thickness across the crystalline plane.

If $A_{S_1} \approx A_{S_2}$, the fringes contrast, V, which is given by Eq.61 has its maximum value and it only depends on the coherency of the interfering beams, γ.

$$V = \frac{2|A_{S_1}||A_{S_2}|}{|A_{S_1}|^2 + |A_{S_2}|^2}|\gamma| \quad (61)$$

While, if $A_{S_1} \neq A_{S_2}$ the fringe contrast, V, decreases. So, the fringe contrast is highly related to the interfering beams intensity. High fringe contrast reduces the phase noise;

$$\delta\phi = \frac{c}{V\sqrt{N}} \quad (62)$$

where $\delta\varphi$ is the phase noise, N is the number of collected electrons per pixel which is related to the interfering beams intensity, and c is a constant.

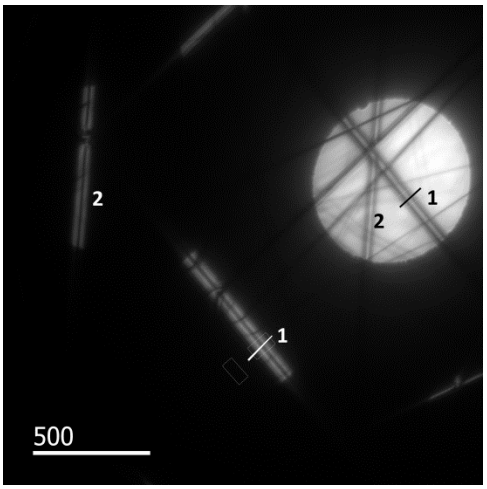

(a)

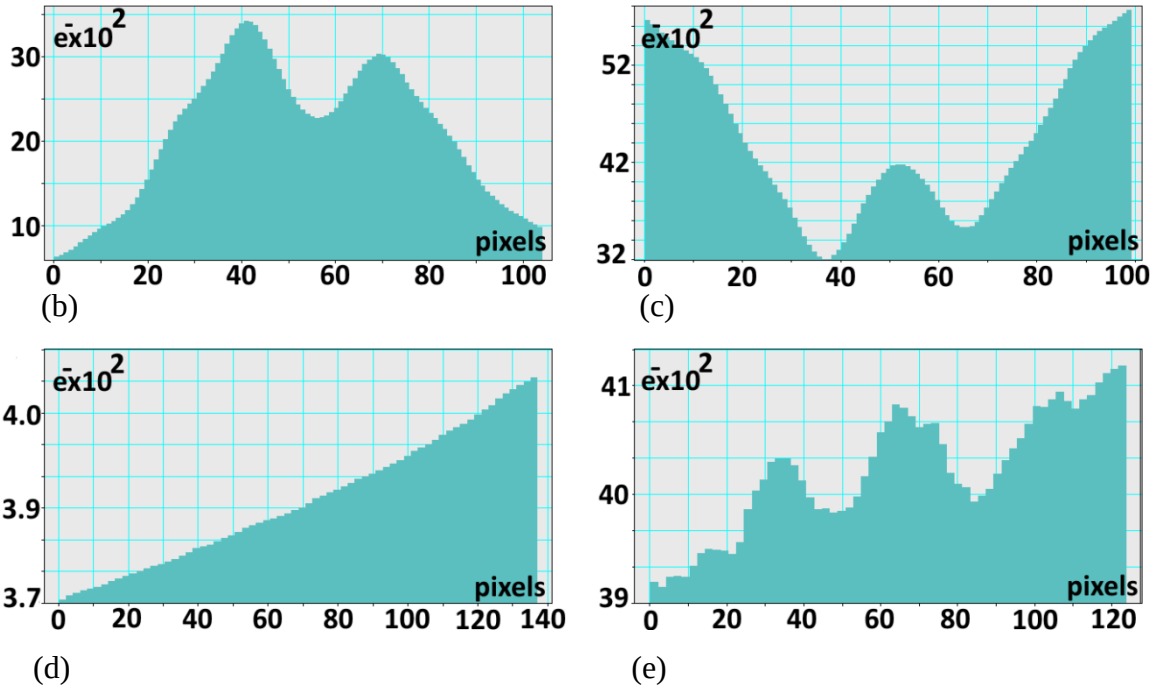

(b) (c)

(d) (e)

Fig. 37 – (a) A CBED pattern showing some symmetric split and individual HOLZ lines in 000 CBED disk and DF disk. The intensity profile across, (b) the split in dark field area, (c) the split in 000 CBED disk, (d) the 000 CBED background, (e) the DF disk background.

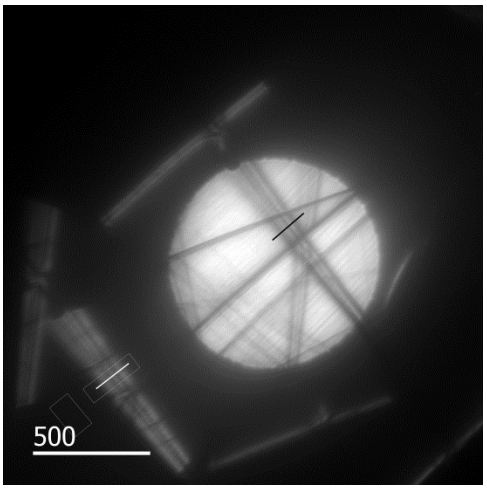

(a)

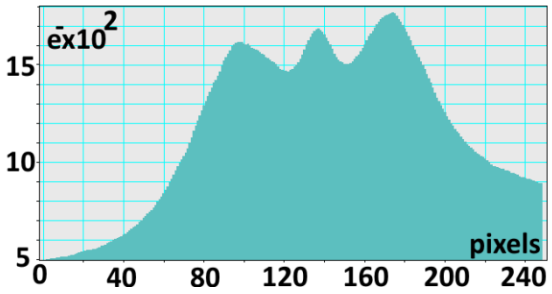

(b)

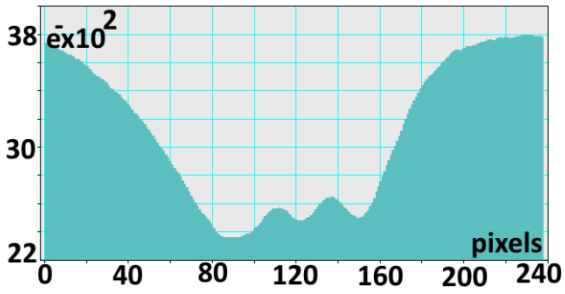

(c)

Fig. 38- The 000 CBED disk at the same orientation of Fig. 37(a) closer to the interface, (b) the rocking curve across the asymmetric HOLZ line in the DF disk, (c) the rocking curve across the asymmetric HOLZ line in the 000 CBED disk.

Therefore, by increasing the split width the contrast of the fringes decreases due to the lower intensity of the interfering beams, however higher split width gives finer fringes due to the inverse relationship of the interfering sources separation and the fringe spacing (Eq. 59 and Eq.60). Finer fringes correspond to the larger carrier frequency, q_c, and easier filtering of the side band. Hence there is always a trade-off between choosing a wide split and high intensity split.

In order to develop this technique it was preferred to avoid additional variables in the experiment to obtain a closer fit with the simulated phase profile. This was only because of the novelty of the technique and the lack of reference phase profiles across the split HOLZ lines. Thus, higher intensity and symmetric split HOLZ lines which $A_{S_1} \cong$

A_{S_2} were preferred to implement the experiment. Although, the technique is feasible for the asymmetric splits as well. Generally, picking a proper split HOLZ line to conduct the experiment was one of the major challenges of the method.

4.3.5 Reconstructing the Phase Profile

The phase image reconstruction was a very crucial step in obtaining the phase profile. Theoretically, the reconstruction steps include Fourier transforming of the fringes, filtering a side band and inverse Fourier transform of the selected side band to get the phase image. Practically, some more steps help with increasing the fringe contrast and the signal to noise ratio. This is discussed in Section 5.1. Filtering the Fresnel fringes and the image edge effect, determining the maximum spatial frequency, q_m (Fig. 31), in order to choose the right filter size, $\frac{1}{3}q_m$, and centering the filter on the side band are very important in the reconstruction steps. This helps with recovering only the phase profile without amplitude information. Choosing the filter size and centering it on the side band is very critical. The larger the source separation, the larger the angle of deflection, α_B. Larger α_B decreases the fringe spacing which results in larger special frequency and carrier frequency. This separates the side bands and the center band in the Fourier domain helping with the filtering. The source separation depends on the split width and the biprism defocus both. Although the larger split gives finer fringes, the intensity of the split HOLZ line decreases due to the multiple scattering around highly strained atomic planes. This decreases N and increases $\delta\phi$ in Eq. 62. The biprism defocus can compromise with the lower intensity splits HOLZ line. The biprism defocus separates the interfering sources more, Eq. 59. However, the biprism defocus has a limit too. Either over focus or defocus can help with the separation of the sources and decreasing the fringe spacing until the contrast of the split HOLZ line is not decreased. By defocusing the biprism more than a specific value the contrast of the split HOLZ lines will be degraded. The biprism defocus can be achieved for each experiment and microscope separately. Fig. 39(a) shows a reference interferogram achieved at the biprism voltage of 8 V. The fringes intensity across the interferogram is presented in Fig. 39(b) showing a non-uniform fringe intensity profile due to the Fresnel fringes. The Fresnel fringes form

by the interference of the diffracted beams from the edge of the biprism. They are unwanted fringes which must be removed from the interferogram.

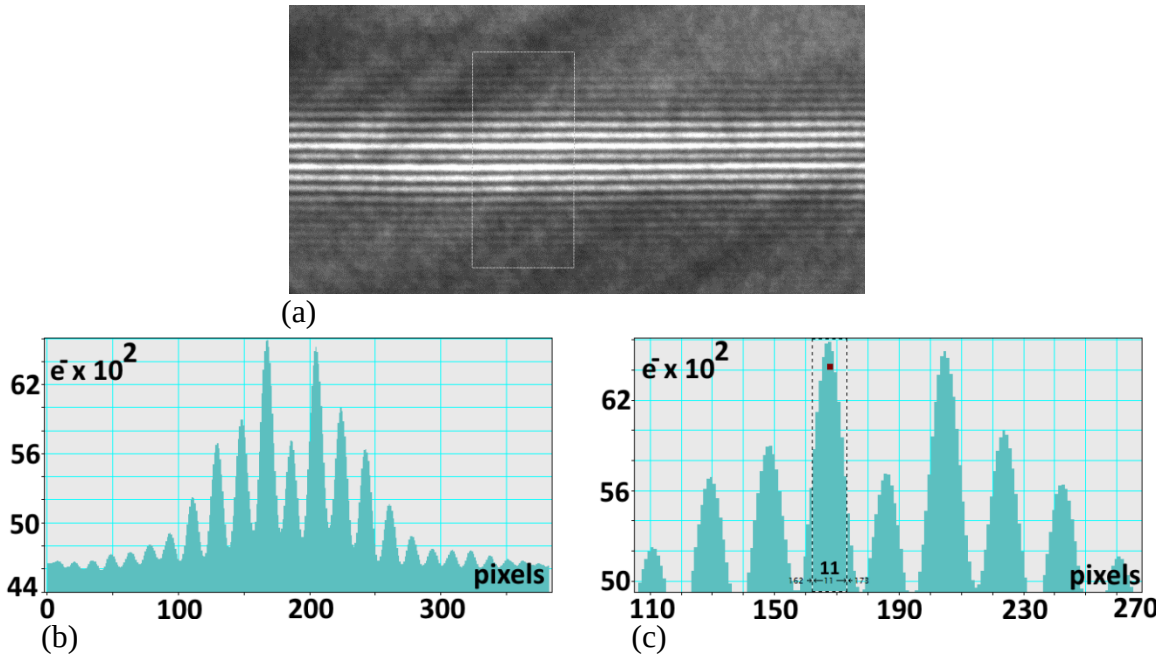

Fig. 39- (a) A horizontal tilted reference interferogram at 8 V, (b) the intensity profile across the fringes showing Fresnel fringes, (c) the fringe spacing is 11 pixels.

Fig. 39(b) shows the fringe spacing of the interferogram which is obtained using the full width at half maximum (FWHM) of the fringe. A method which helps removing the Fresnel fringes is to filter the interferogram before the reconstruction steps. The FT of the interferogram in Fig. 39(a) is given in Fig. 40(a). The FT space shows the distribution of the intensity around the center band and side bands and the intensity tails which can degrade the signal to noise ratio. The Fresnel fringes intensity contributes to the intensity distribution between the side bands and the center band. Initial filtering of the interferogram was done in several steps to remove the tails and the Fresnel fringes effects. A Gaussian filter was used to denoise the interferograms. Fig. 40(b) is achieved after 4 times filtering. Three times filtering were performed to remove the tails intensity and once was done to remove the Fresnel fringes intensity. This step requires some accuracy in terms of the right width and the position of the filter to avoid removing the

phase information carried by the side bands. If the filter is not applied carefully it may decrease the fringe contrast which decreases the signal to noise ratio. So, one must be careful to avoid reducing the fringe contrast.

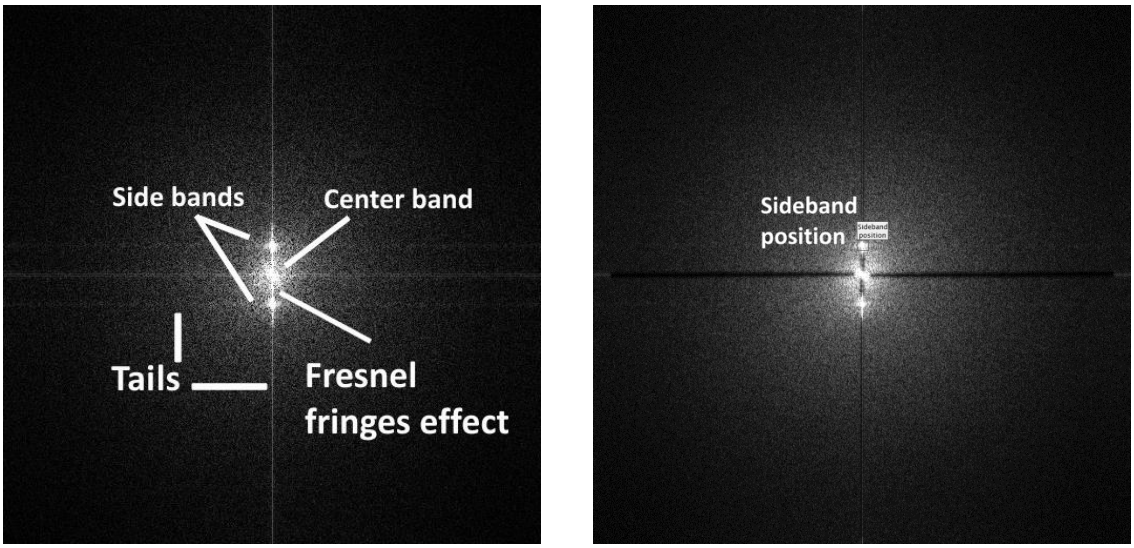

(a) (b)

Fig. 40- (a) The FT of a non-filtered interferogram, (b) the filtered FT image of the fringes. To remove the tails the filter width was 8 pixels. To diminish the Fresnel fringes effect, the filter width was 4 pixels. The tails are caused due to the image edge effect.

Comparing Fig. 39(c) and Fig. 41(c) shows not only the Fresnel fringes can be removed by filtering the interferogram but also the fringe spacing decreases. Therefore, the interferogram used to reconstruct the phase image was Fig. 41(a). Unlike the electron holography, the electron interferometry has no reference wave and the phase measurement is a relative measurement. In fact the phase of both interfering beams is unknown. However, the interferogram in Fig. 41(a) which represents the fringes of the biprism without the split HOLZ line can be considered as a reference interferogram. This reference interferogram can provide the SIS-HOLZ method with a reference phase image and a phase profile. This is to compare the phase profile across a split HOLZ line to help with a better interpretation of the data.

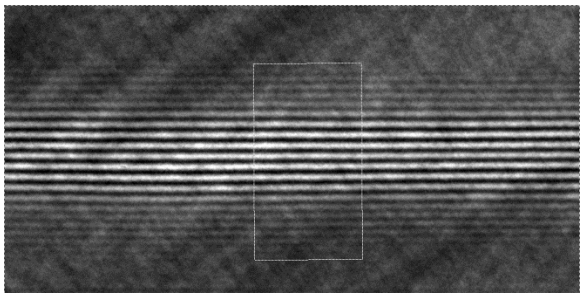

(a)

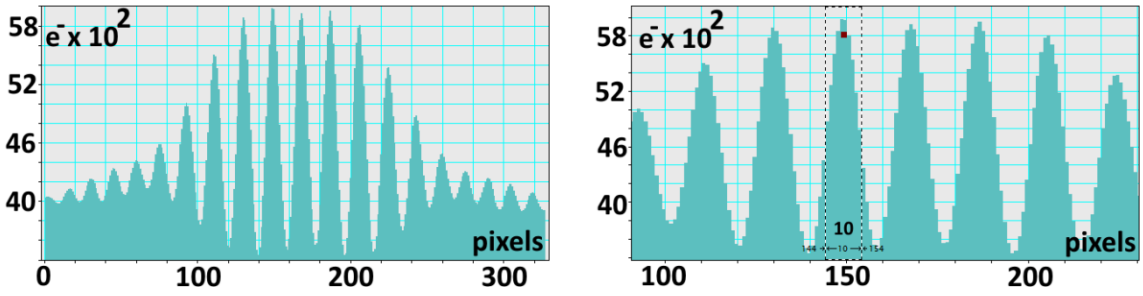

(b) (c)

Fig. 41- (a) The filtered interferogram, (b) the fringe intensity profile across the filtered interferogram, (c) the fringe spacing is now 10 pixels.

The FT of the filtered reference fringes (Fig. 41(a)) with the position and the size of a window on one of the side bands, the reconstructed phase images and the phase profiles before and after initial filtering of the interferogram are given in Fig. 42.

A reference phase profile usually shows a flat phase profile depending on the size and position of the filter i.e. Fig. 42(d), however the reference phase profile from an unfiltered interference pattern shows a noisy profile in Fig. 42(e).

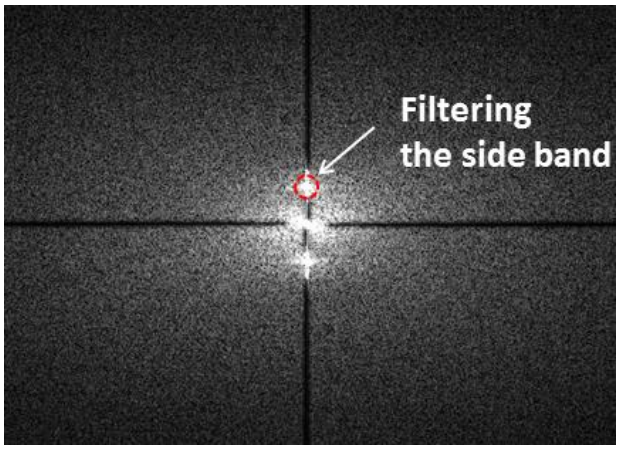

(a)

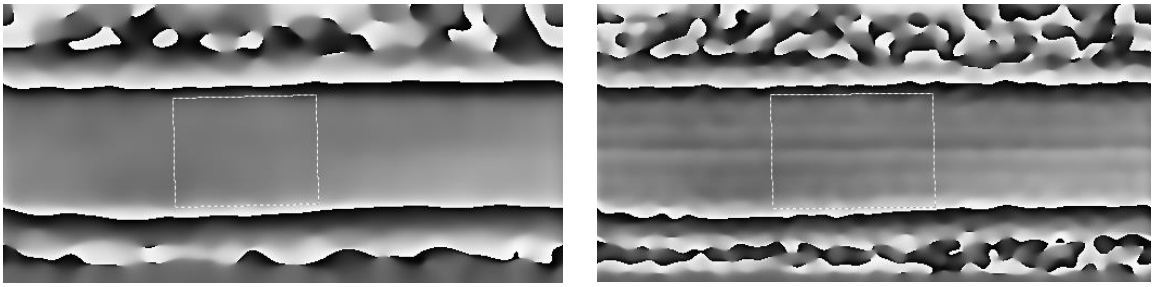

(b) (c)

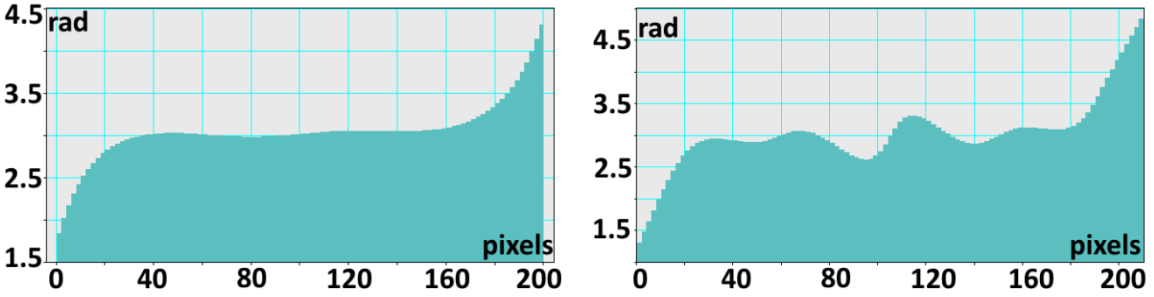

(d) (e)

Fig. 42- (a) The window position and its size in the Fourier space of the interferogram in Fig. 41(a), (b) the reconstructed filtered reference phase image, (c) the reconstructed unfiltered reference phase image, (d) the filtered reference phase profile and, (e) the unfiltered reference phase profile.

Now, by inserting the aligned biprism into a split HOLZ line from the same CBED pattern taken at the same ZA shown in Fig. 36 (with a different tilt) and self-interfering the split, an interferogram was obtained which is presented Fig. 43(a). A horizontally tilted sub-image of the interferogram is presented in Fig. 43(b). The

experiment was conducted in the DF disk and the interferogram was filtered prior to the reconstruction steps to increase the signal to noise ratio. Comparing the phase profile in Fig. 43(d) with the flat phase profile obtained from the reference interferogram shows multiple peaks which represents the phase profile across the split HOLZ line. This experiment was conducted on several split HOLZ lines to investigate if the experiment is repeatable and the SIS-HOLZ interferograms were reproducible. Additionally the effect of the biprism voltage was studied experimentally. The results are reported in Section 4.3.6.

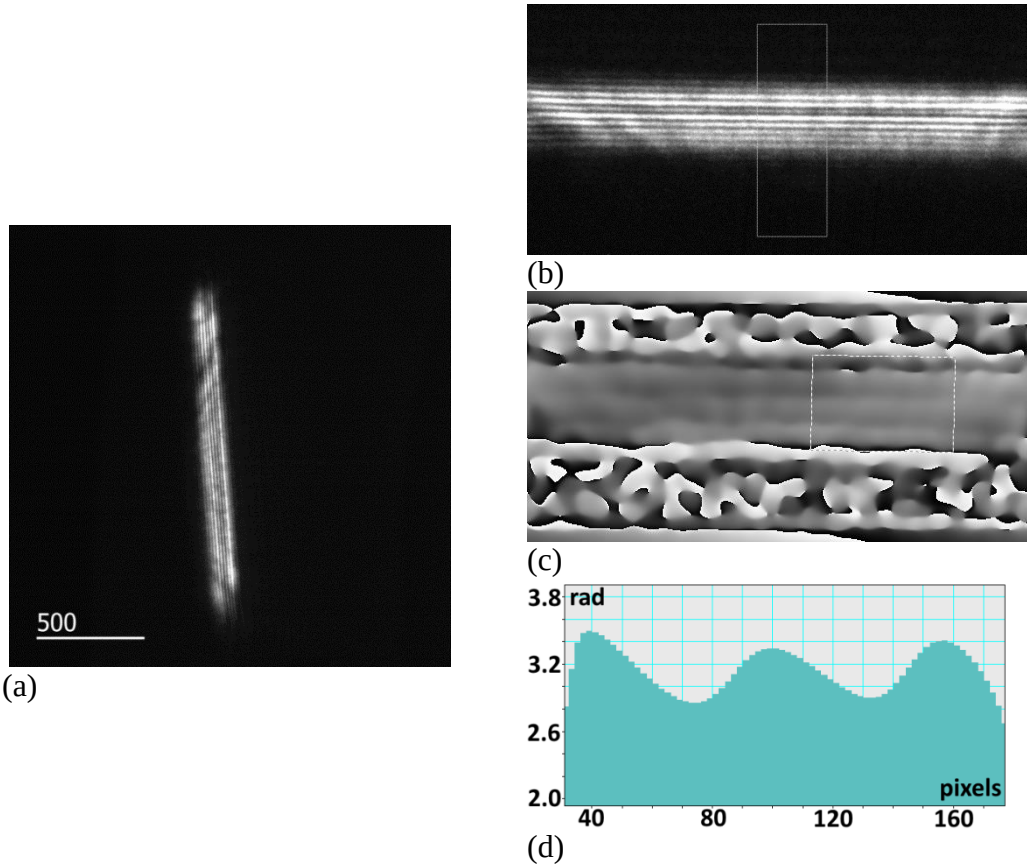

Fig. 43- An interferogram achieved by self- interfering of the split HOLZ line in the DF disk, (b) a horizontally tilted sub-image of the interferogram, (c) the reconstructed phase image, (d) the phase profile across the split HOLZ line obtained from the phase image.

4.3.6 The Phase Profiles by Increasing the Biprism Voltage

The SIS-HOLZ was implemented on the split HOLZ line in Fig. 44 at different voltages.

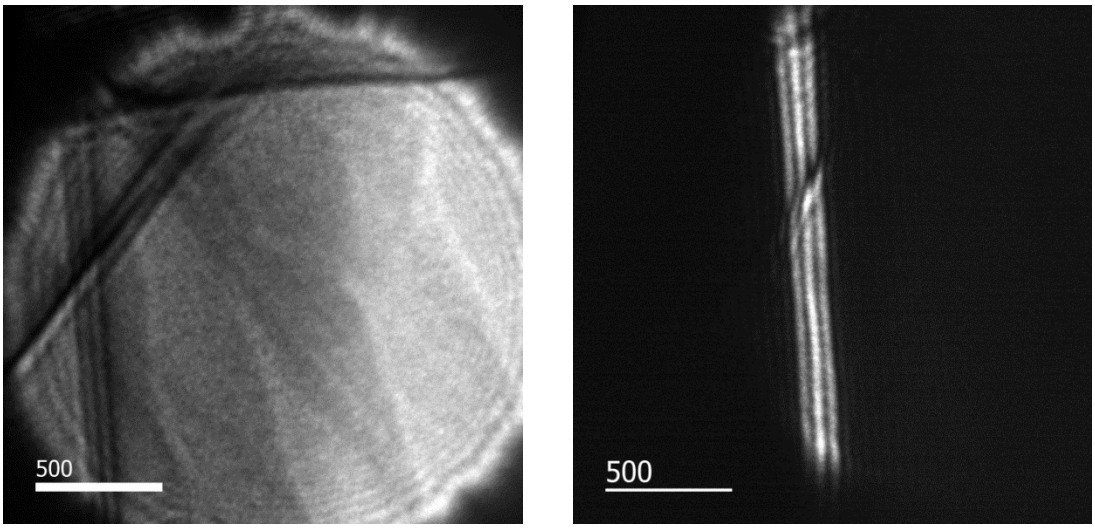

(a) (b)

Fig. 44- (a) 000 CBED pattern taken at a tilt with respect to 011 ZA, recorded with a GIF camera,(b) the corresponding DF disk split HOLZ line.

The reconstructed phase profiles while increasing the biprism voltage from 4V to 12V are presented in Fig. 45. In Fig. 45(a) there is no peak in the phase profile. Fig. 45(b) shows two halves of the split starts interfering at 5V since a peak appears at 5V and its height increases by increasing the biprism voltage from 6V to 8V in Fig. 45(c) to Fig. 45(e). The peak height decreases again at 9V and 10V in Fig. 45(f) and Fig. 45(g). At 11V, multiple peaks appear, Fig. 45(h), and at 12V two separated peaks can be seen which seems two halves of the split are totally separated, Fig. 45(i). Assuming the phase profile across the split HOLZ line the same as Fig. 46, the explained changes in the phase profiles regarding the biprism voltage (Fig. 45) can be justified schematically. In Fig. 46 the phase is shown in two parts of $\phi_1(\mathrm{Rf}(z))$ and $\phi_2(\mathrm{Rf}(z))$ which represent the left and the right sides of the phase profile across the split HOLZ line. S_1 and S_2 correspond to $\pm\Delta\theta/2$, where $\Delta\theta$ is the angular deflection from the exact Bragg angle due to the atomic bent. The SIS-HOLZ experimental phase profile is the outcome of the sketched overlap. By increasing the biprism voltage, S_1 and S_2 shift more towards each other. This shift is related to K_B.

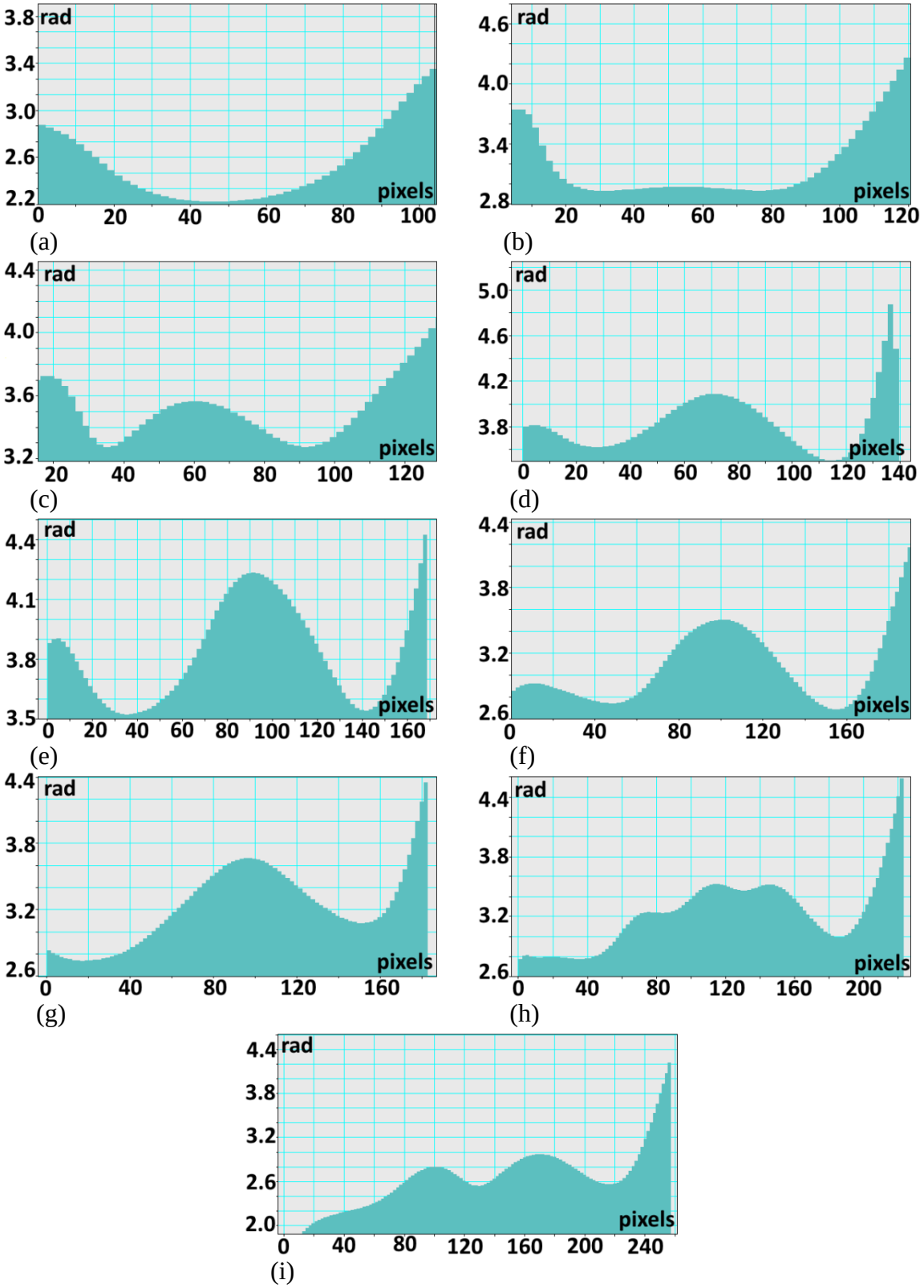

Fig. 45- The reconstructed phase profiles at the biprism voltage of, (a) 4V, (b) 5V, (c) 6V, (d) 7V, (e) 8V, (f) 9V, (g) 10V, (h) 11V and, (i) 12V.

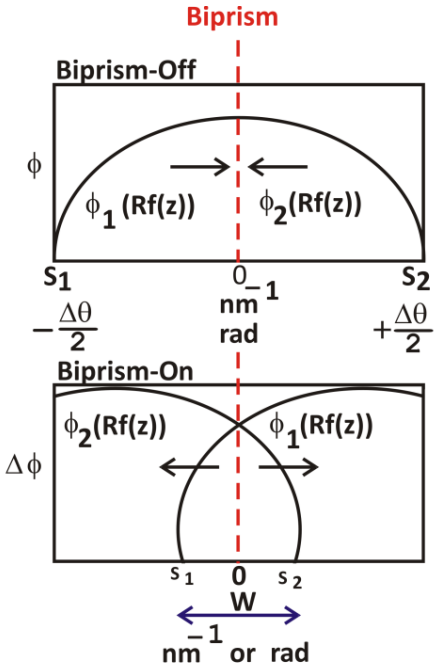

Fig. 46- A schematic of the phase profile across the split HOLZ line. When the biprism is off, there is no interference and only the split HOLZ line can be seen. When the biprism is on, the left and the right halves interfere **[27]**.

Accordingly, in Fig. 45 the full overlap may have happened at (7-8)V with the maximum height of the central broad peak and then two halves of the split started to diverge and pass each other after the biprism voltage of 9V. The halves are totally separated at about 12V. The rigid shift of the interfering beams, K_B, is linearly related to the angle of deflection, α_B. Therefore, the information of the biprism deflection angle is required for the simulation purposes. It helps with calculating the rigid shift of the interfering beams towards each other on the diffraction plane. The fringes spacing information at each biprism voltage is used to calculate the angle of deflection. Also recording the precise value of the biprism defocus is a requisite. The experimental obtained fringes for the biprism voltages from 6V to 10V in Fig. 45 are shown in Fig. 47.

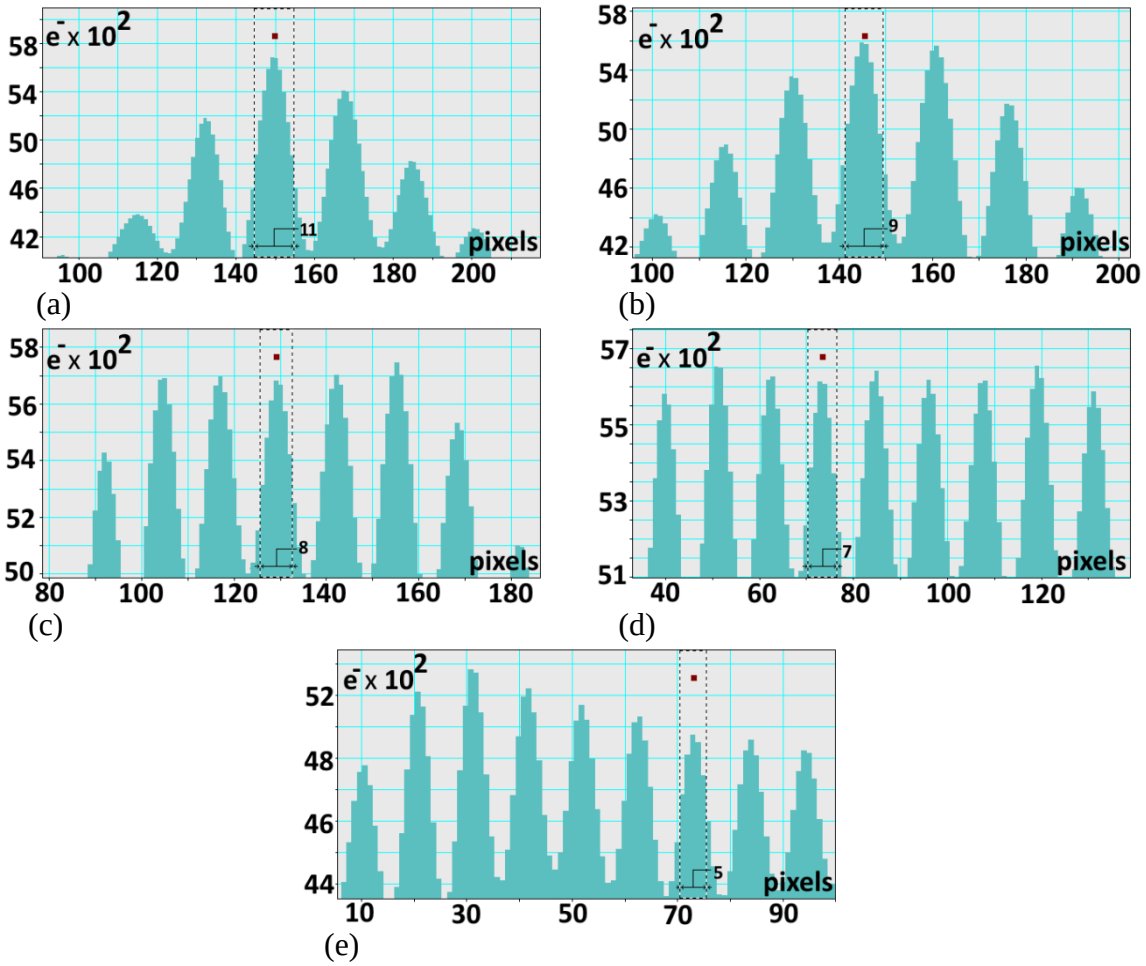

Fig. 47- The obtained fringes at the biprism voltages of, (a) 6V is 11 pixels, (b) 7V is 9 pixels, (c) 8V is 8 pixels, (d) 9V is 7 pixels, (e) 10V is 6 pixels. The pixels size is 0.005 $\mathbf{nm^{-1}}$.

At a constant biprism defocus the fringe spacing decreases by increasing the biprism voltage. The angle of deflection is directly related to the biprism voltage. Fig. 47 shows the effect of the biprism voltage on the fringes spacing. The same as the central peak height in the phase profiles, the fringe intensity also shows an increasing/decreasing trend. The maximum number of recorded electrons happens at the biprism voltage of 8V. According to Fig. 45(e), the maximum height of the central broad peak in the phase image happens at the same biprism voltage. The fringe intensity change is possibly due to the difference of the interfering beams intensity. As it is mentioned before, the split HOLZ line has two main peaks with the maximum intensity and multiple lower

intensities inside the split. Interfering the lower intensities will form lower intensity fringes. Since the fringe intensity starts decreasing at the biprism voltage of 9V and multiple peaks in the phase profile form at 10V, fully overlap of two halves at 8V can be confirmed. Also, the halves start diverging at 9V. Therefore, knowing the biprism deflection angle is required to put the right phase shift in the simulation. The angle of deflection for different biprism voltages are calculated using Eq. 60. The electron wavelength at 200 kV is 2.51×10^{-3}nm and the recorded biprism defocus was ≈ 6 µm. The calculated biprism deflection angle change obtained from the experimental data presented in Fig. 45 and Fig. 47 is plotted versus the biprism voltage in Fig. 48.

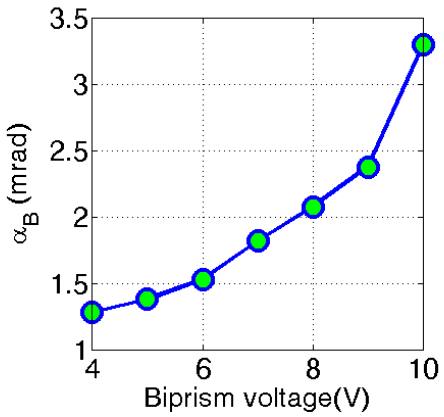

Fig. 48- The biprism deflection angle is directly related to the biprism voltage. The biprism defocus is considered as**6 µm**.

The tilt in the phase profiles, Fig. 45, can be due to the misalignment of the biprism with respect to the split HOLZ line, although the alignment is done in both image mode and diffraction mode. It is previously shown that even small biprism misalignment can cause significant asymmetry in the phase profile (Section 3.1.3). Regardless of the small differences in the phase profiles, the central main broad peak representing the bell-shape atomic displacement is a common feature in Fig. 45(c) to Fig. 45(g). The main broad peak in the reconstructed phase profiles has been observed for the other split HOLZ lines taken in the Si substrate close to the interface either in the DF disk or in the 000 CBED disk. Comparing the simulated phase profiles in Section 3.1.2 with the experimental phase profiles, reveals that the only z-dependent atomic displacement

distribution which produces a broad peak in the center of the phase profile is the bell-shape displacement profile. This confirms the atomic displacement through the thickness of the examined crystal is a cosine bell-shape function defined either in Eq. 40 or Eq.47.

4.4 Data Quantification

In this work several times several specimens were fabricated and the last time a very uniform specimen in terms of thickness was fabricated with the thickness of ≈ 166 nm. At almost a flat specimen (no tilt), the beam was at 100 ZA. It was very easy to reach 004 Kikuchi band. At almost zero tilt ($\alpha \approx 1.4°, \beta \approx 0.4°$) 000 CBED disk with 008 HOLZ line was achieved, Fig. 49. In addition to the split HOLZ lines the broadening and some distortion at the intersection of HOLZ lines can be seen. This is due to the dynamical interaction of electron beam with crystal at these places.

The CBED patterns in Fig. 49 were recorded by the CCD camera with the acquisition time of 5 seconds.

In this specimen the split started at a different distance from the interface comparing with the reported information in Fig. 36. This can be due to some reasons;

1. Different thicknesses. In Fig. 36 the diffraction patterns were taken at a thicker specimen comparing with the diffraction patterns presented in Fig. 49. The specimen was also highly tilted which increases the thickness.
2. Strain relaxation. Due to the strain relaxation in thinner specimens, thicker specimens can hold strain at larger distances from the strained region.
3. Different HOLZ lines. HOLZ lines with different **g** vectors do not show the same sensitivity to the strained region.

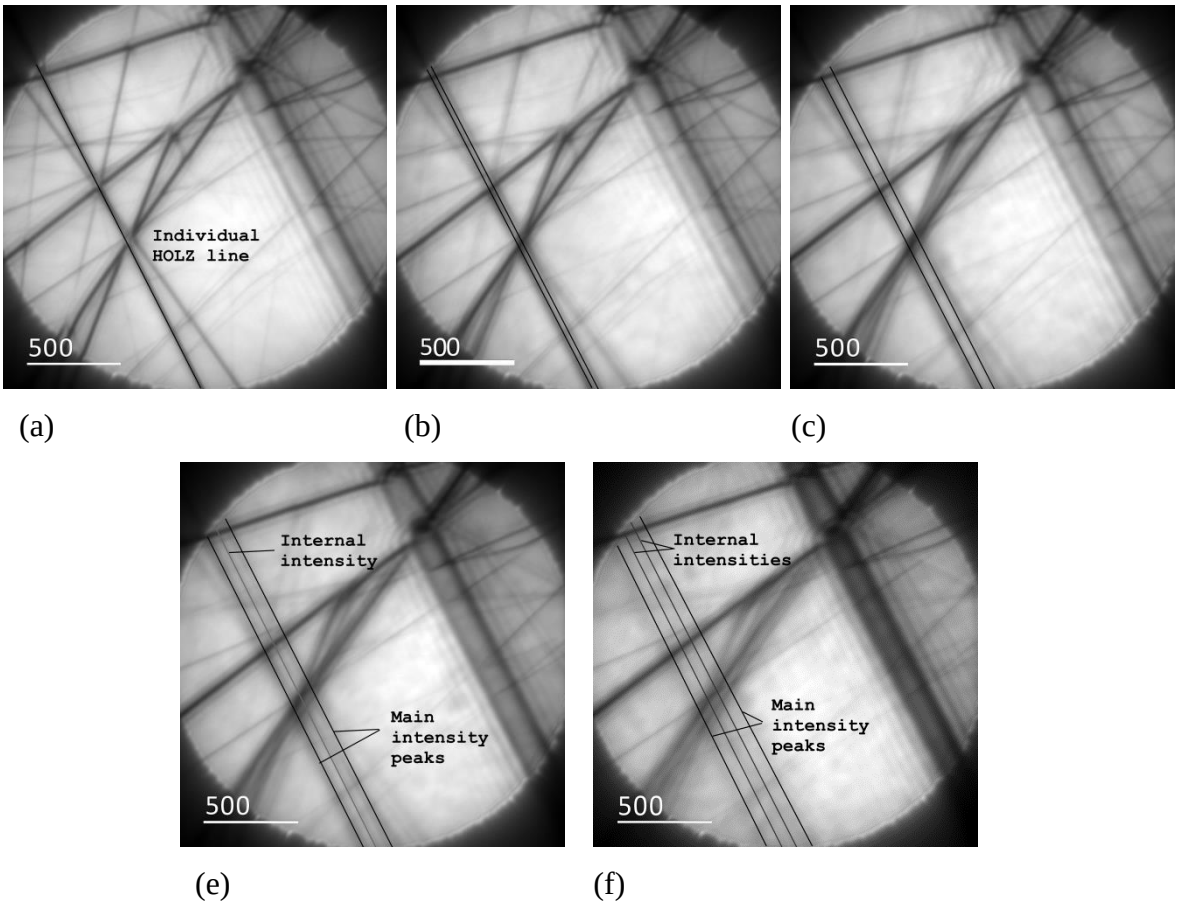

Fig. 49 - The 000 CBED disk obtained along the 004 Kikuchi band showing the HOLZ line taken within the Si substrate at (a) 400±10 nm (no split), at (b) 200±10 nm (begin to split), at (c) 180 ±10 nm, (d) 100 ±10 nm and at (e) 70 ±10 nm (the largest split) away from $Si/Si_{0.8}Ge_{0.2}$ interface [27].

Fig. 50 shows the corresponding excess split HOLZ lines to the deficient HOLZ line in Fig. 49. The DF disk split HOLZ lines have a higher contrast compared to their corresponding ones in BF disk making it easier to follow the trend in the splitting of HOLZ line while moving towards the interface. 008 HOLZ line could be seen clearly in the zoom mode, too. Therefore, the distances from the interface of Si substrate and $Si/Si_{0.8}Ge_{0.2}$ superlattices, the labeled spots in Fig.32(b), are estimated roughly by tracking the HOLZ line split width with respect to the interface in the image mode while moving the probe towards the interface.

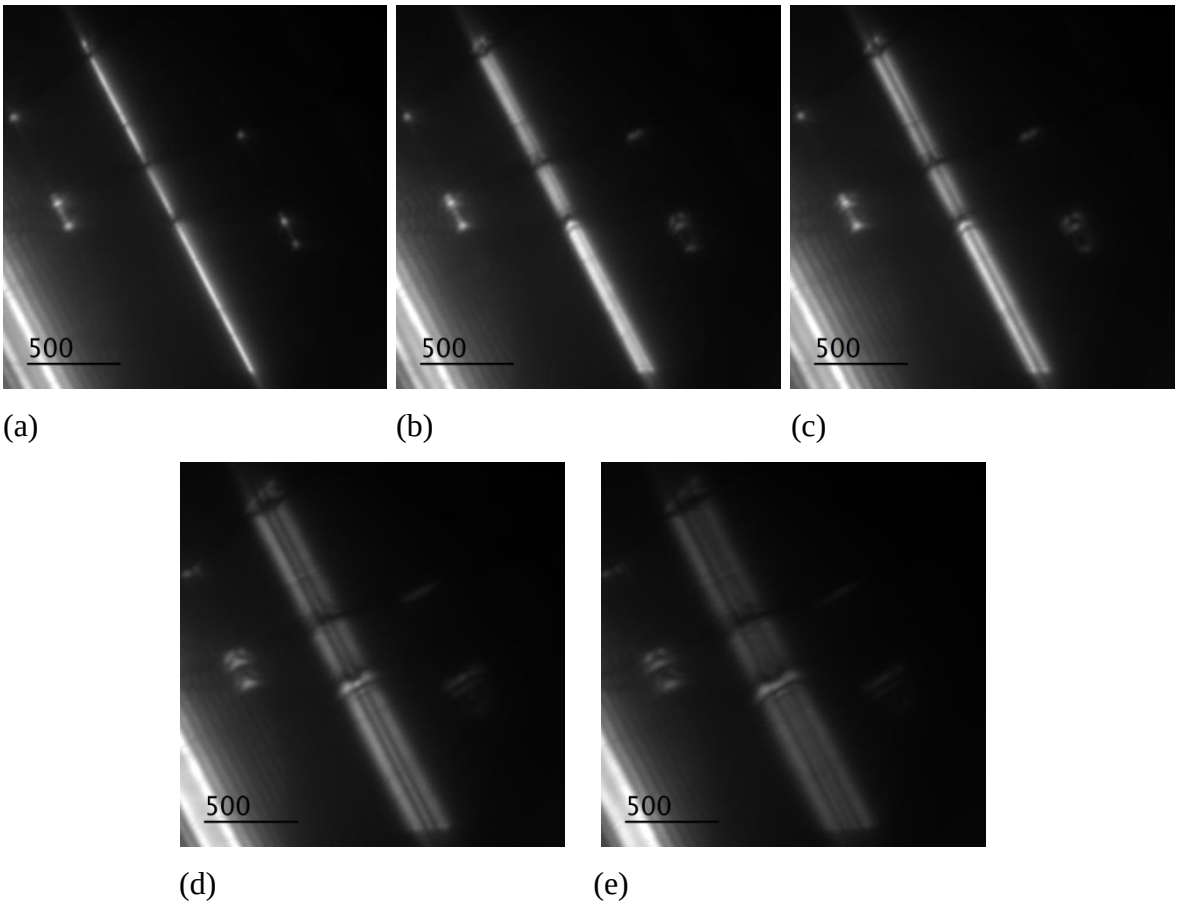

(a) (b) (c)

(d) (e)

Fig. 50- The DF disk 008 split HOLZ line obtained away from Si and $Si_{0.8}Ge_{0.2}$ interface at, (a) 400 $\pm$ 10 nm, at, (b) 200 $\pm$ 10 nm, at, (c) 180 $\pm$ 10 nm, at (d) 100 $\pm$ 10 nm and, at (e) 70 $\pm$ 10 nm showing an increase in the split width approaching the interface [27].

The split width has a linear relationship with the atomic displacement amplitude. Thus, further away from $Si/Si_{0.8}Ge_{0.2}$ interface, the split width is decreased until at a large distance of $\geq$400 nm from the interface a non-split, non-broadened HOLZ line with no dynamical effects can be observed, Fig. 49(a) and Fig. 50(a). The bright band on the bottom left side shows the 004 Kikuchi band. At about 80 nm away from the $Si/Si_{0.8}Ge_{0.2}$ interface (Fig. 49(e) and Fig. 50(e)) the split HOLZ line is wide and symmetric, which is a good condition to self-interfere. The split width and its symmetry importance will be discussed further in Section 4.5.

The next step before interfering two halves of split is to center the aligned biprism within the split. This is easier to be done in the DF disk. Fig. 51, shows the intensity

profiles across the split HOLZ line without and with a biprism inserted in the split having a negative potential to separate the intensity into two halves. There are two high intensity and two low intensity fringes within this split HOLZ line, Fig. 51(a) and Fig. 51(c), the biprism is placed in the center of the split HOLZ line in Fig. 51(b), cannot be seen except for its shadow running the length of the HOLZ line. On either of its sides there are two high intensity peaks, Fig. 51(d), having a reasonably symmetric intensity distribution, $A_{S_1} \cong A_{S_2}$. This is achieved by adjusting iteratively the virtual sources using the biprism defocus and the electron beam cross over position.

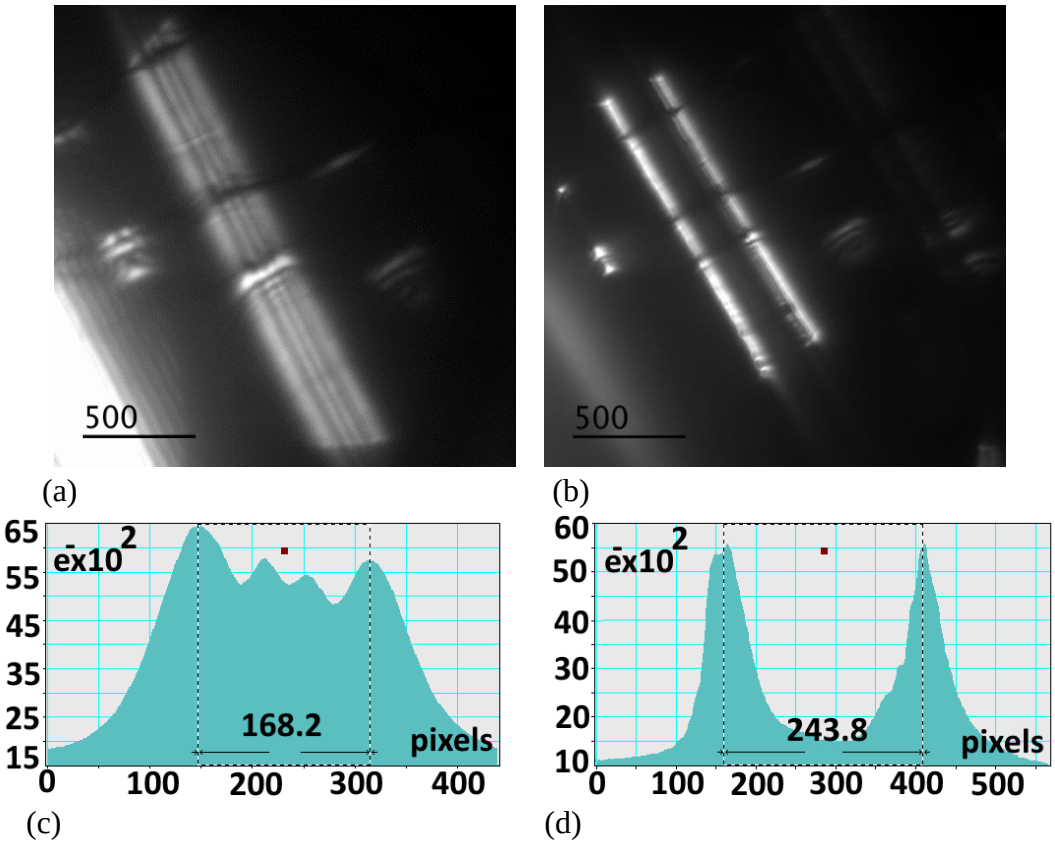

Fig. 51- (a) the DF disk 008 split HOLZ line, (b) the biprism with a negative potential centered within the split HOLZ line for the alignment purposes, (c) the intensity distribution across the split HOLZ line in (a), (d) the intensity profile while the biprism is centered inside the split HOLZ line [27].

Fig. 51(c) shows the split width of ≅168 pixels. A conversion factor of 8.68×10^{-6} rad/pix is used to convert the split in pixels into the angular deflection in radian. Therefore, $\Delta\theta$ which is the angular deflection corresponds to the split HOLZ line is

equivalent to $\approx 1.46 \times 10^{-3}$ rad, Eq. 63. Accordingly both experimental and calculated phase profiles are plotted versus $\Delta\theta$ at the end. $\Delta\theta$ is the deviation of the Bragg angle due to the atomic displacement linearly related to the split width.

$$\Delta\theta = \frac{s}{g} \tag{63}$$

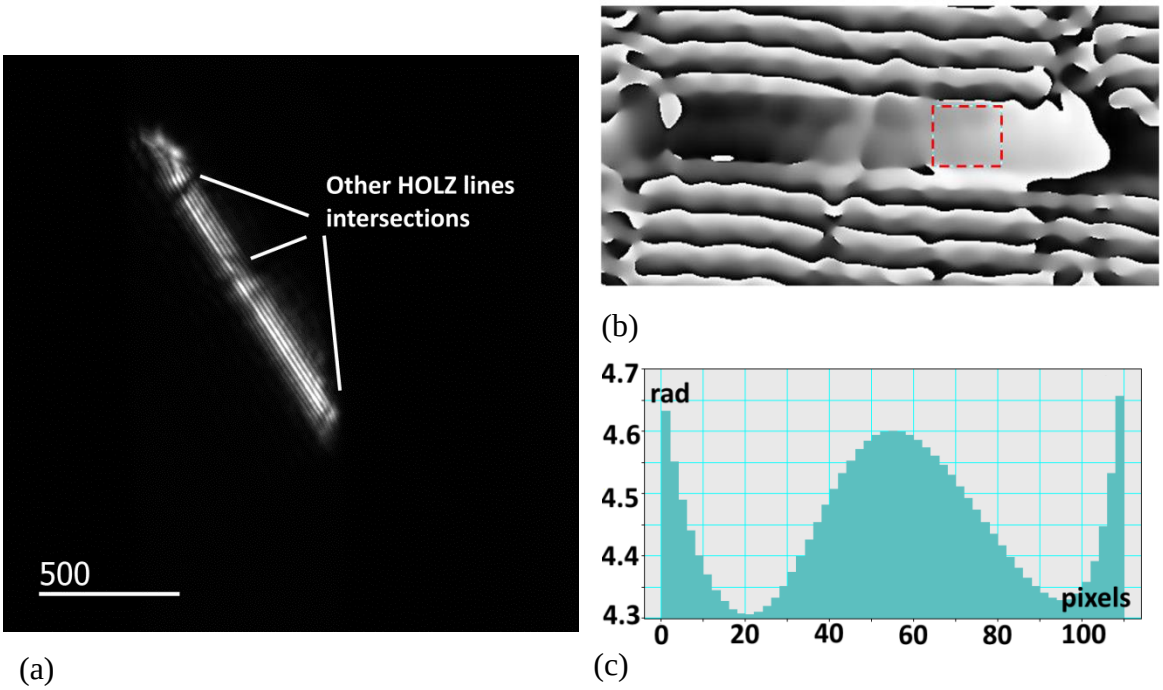

Fig. 52- (a) the interferogram of the self-interfered split HOLZ line showing fine fringes running parallel with the length of the HOLZ line, (b) the reconstructed phase image of (a) tilted horizontally for the presentation, (c) the phase profile passing through its width across the sketched box within the phase image [27].

The phase profile is obtained across the boxed area in Fig. 52(b). It was preferred to avoid extra phase shift due to other HOLZ lines intersections shown in Fig. 52(a). The phase profile in Fig. 52(c) shows a good agreement with a cosine bell-shape displacement profile through the thickness of the crystal. The phase profile in Fig. 52(c) is from the red box on the right side of the phase image. The phase profile from the left side shows the same profile except it is phase shifted by $-\pi$. This is most probably due to the smaller atomic displacement amplitude. Recovering the phase profile along the HOLZ line

including both sides gives the average phase profile along 008 atomic planes. The results is closer to Fig. 52 (c).

Eq. 46 is used to simulate the phase profile and compare it with the experimental phase profile.

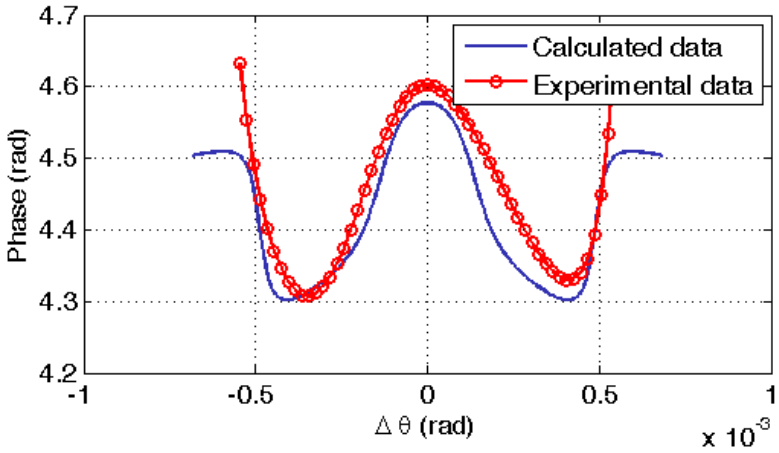

Fig. 53- The calculated phase profile is compared with the experimental phase profile showing a reasonably good fit [27].

Knowing the index of the experimental HOLZ line as 008 and measuring the accurate thickness of the specimen at the ROI helps to fit the profiles at $s = 0$ which is the exact Bragg condition and $\Delta\theta = 0$. Therefore, Eq. 51 is used to fit the central broad peak of the simulated phase profile for 008 at 80 nm distant from $Si_{0.8}Ge_{0.2}/Si$. R=0.0325 nm gives the best fit between simulated profile and the experimental profile. Hence, the reconstructed atomic displacement profile along the z-axis is a bell shape cosine profile which is shown in Fig. 54.

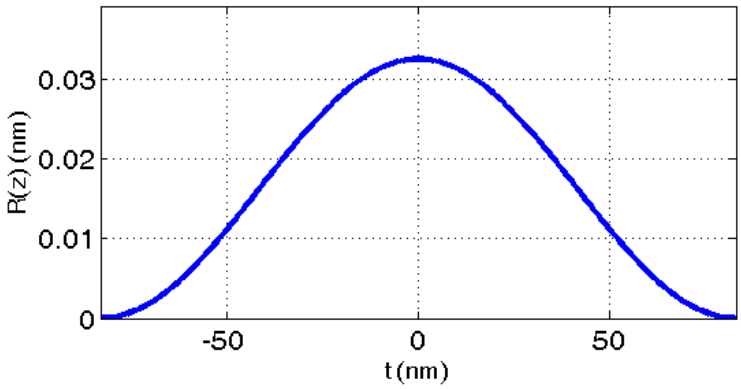

Fig. 54- The atomic displacement profile for 008 atomic plane at 80 nm distance from the interface along the z-axis which is through the thickness of the crystal [27].

The obtained R is the amplitude of atomic displacement for 008. Regarding Saitoh et al. [42] the displacement vector for 008 atomic plane at 80 nm away from the interface of $Si/Si_{0.8}Ge_{0.2}$ superlattices can be defined as **R(**z**)**=0.0325[008].

An experiment is defined as a scientific procedure undertaken to make a discovery, test a hypothesis, or demonstrate a known fact. Therefore, it is a big fraud to claim all the obtained data were perfect and could be quantified using the developed analytical routine. In the following section some examples of the phase profiles which were difficult to interpret are reported.

4.5 Imperfect Data

Some reconstructed phase profiles were hard to interpret and fit with the simulated data. The phase profiles in Fig. 55 are taken from the interference of the same split HOLZ line at Fig. 50. However, they are taken from another specimen in different experimental conditions follows;

1. The specimen used for these profiles showed huge thickness variation, Fig. 34 (b-e). It was very difficult to track the exact thickness at each ROI.
2. Due to the significant inclination angle between the specimen and the copper grid, happened during the specimen fabrication, $\geq$ **17°**, the specimen required a big tilt to bring in the split HOLZ line, more than 10° for both **α** and **β**. This effects on the intensity of HOLZ line, subsequently the phase noise.

Firstly, It was expected to see the same trend in the phase profiles as explained by Fig. 45. It seems the overlap of the peaks has started at the biprism voltage of 7V, although the profiles are tilted in Fig. 55(a) and Fig. 55(b). At the biprism voltage of 8V a "noisy phase" profile with a significant decrease in the phase can be seen. It seems the divergence of the halves starts at the biprism voltage of 10V. Therefore,

1- The trend and the order of the phase profile changes are not quite comparable with the results in Fig. 45,
2- The multiple peaks phase profile in Fig. 55(c) and the big peak with its remarkable height increase in Fig. 55(d) are not justifiable comparing with Fig. 45 and the predicted model.

The most confusing and dissatisfying features observed in the phase profiles are listed as follows:

- Asymmetric and tilted peak(s)
- Multiple peaks which can be referred to as "noisy phase" profiles.

The main investigated reason for such results is the intensity of the primary interfering beams, N in Eq. 62. The intensity profile across the corresponding split HOLZ line self-interfered to obtain the phase profiles in Fig. 55 is presented in Fig. 56. The presented profile shows the number of recorded electrons in the primary interfering beams, $S_1$and S_2, approximately 45-50 times smaller than the interfering beams in Fig. 51(c). According to Eq. 62, the phase noise can be approximately 6-7 times larger. In addition to N, the fringe contrast, V, can also be affected by the amplitude of the interfering beams, Eq. 61.

High intensity and symmetric interfering beams, $A_{S_1} \cong A_{S_2}$, give higher contrast fringes which decreases the phase noise. Fig. 56 shows low intensity asymmetric split HOLZ line.

Also the intensity profile shows multiple intensity peaks in the exterior regions of the main peaks which can possibly be due to the multiple scattering effect. This is because of the higher thickness of the specimen (≥ 200 nm). Therefore, sharper split HOLZ line the same as Fig. 49 and Fig. 50 can give a less noisy phase profiles.

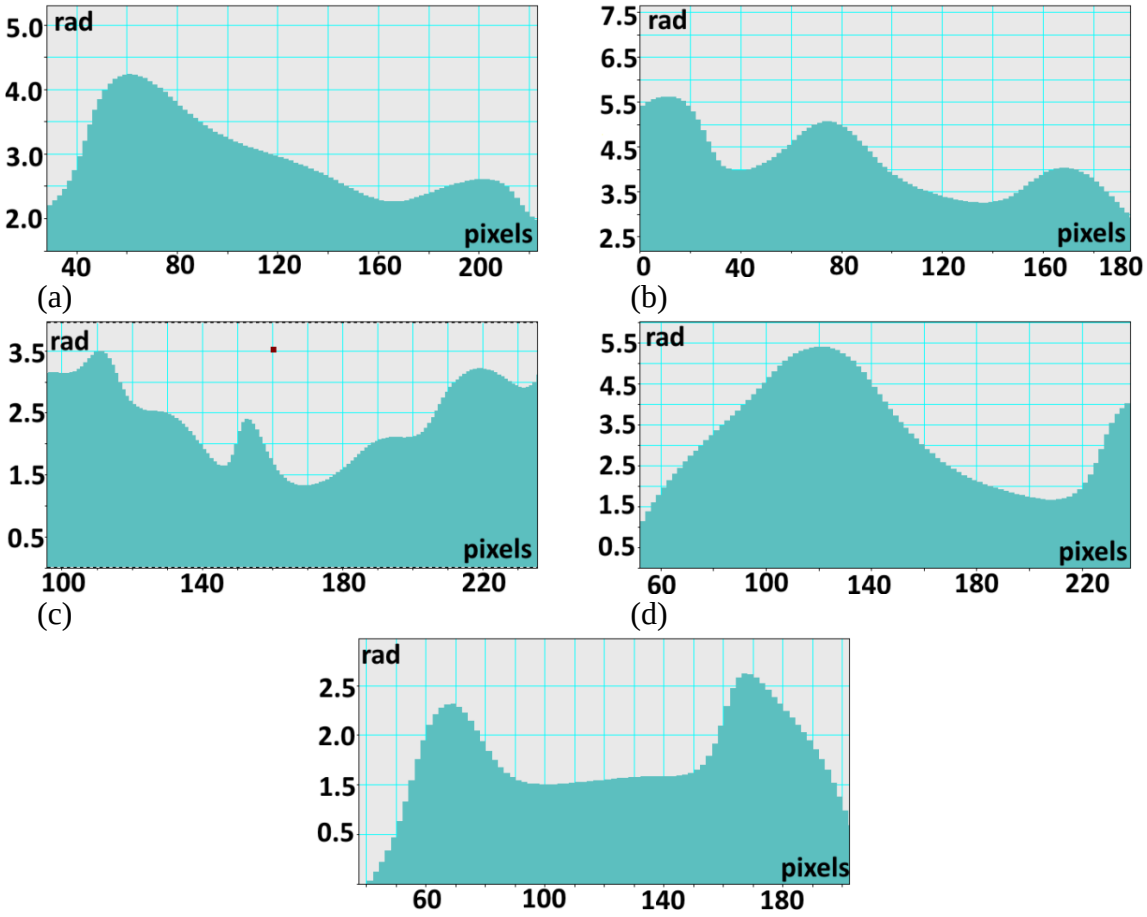

Fig. 55- The reconstructed phase profile taken from 008 split HOLZ line at the biprism voltages of, (a) 6V, (b) 7V, (c) 8V, (d) 9V and, (e) 10V.

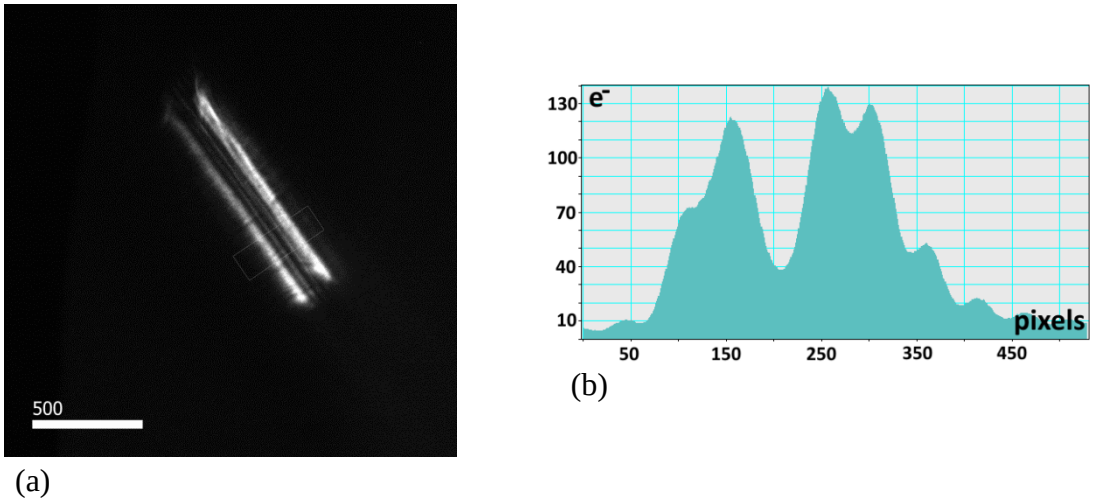

Fig. 56- (a) DF disk 008 split HOLZ line, (b) the intensity profile across the split.

Low intensity HOLZ lines were either taken from a thicker specimen, above 200 nm, or from a highly tilted specimen. Besides adjusting the biprism defocus which was a tricky step highly influenced on the fringe spacing. Finer fringes give higher carrier frequency, q_c. Higher carrier frequency helps with filtering the side band in the reconstruction steps. Higher biprism defocus and larger split width give finer fringes, Eq. 59 and Eq. 60.

Furthermore, the tilted phase profiles are most possibly due to the biprism misalignment. The effect of the biprism misalignment is presented in Section 3.1.3. In Fig. 53, the biprism misalignment is calculated as 22 mrad with respect to the split HOLZ line.

Another possibility of achieving confusing phase profiles was the physical condition of the biprism. The used biprism in this work was not quite clean and there were particles attached to the biprism. While aligning the biprism, one must find the clean area of the biprism to self-interfere the split HOLZ line, however post adjustment of the biprism in the diffraction mode may lead to the biprism movement and bringing the attached particles into the image. This produces extra phase peaks in the phase profile, Fig. 57. Although, reconstructing a reference interferogram helps with misinterpretation due to the biprism imperfection.

Another experimentally finding in the method was sensitivity of the technique to the external noises. All the interpretable data i.e. Fig. 49 and Fig. 50 were taken after working hours in the building. High intensity sharp HOLZ lines, adjusting the biprism defocus and fine fringes interferograms were easier achievable and reproducible in the evening. This is most probably due to the lower vibration of the building during the night time. This is achieved statistically comparing the data taken during the day time and the shorter time usually spent to obtain high contrast fine fringes after the working hours.

In the next chapter the main steps, considerations and limitations of the SIS-HOLZ technique in order to obtain a more reliable and less noisy phase profiles is summarized. Also, some future work for further development of the technique is presented.

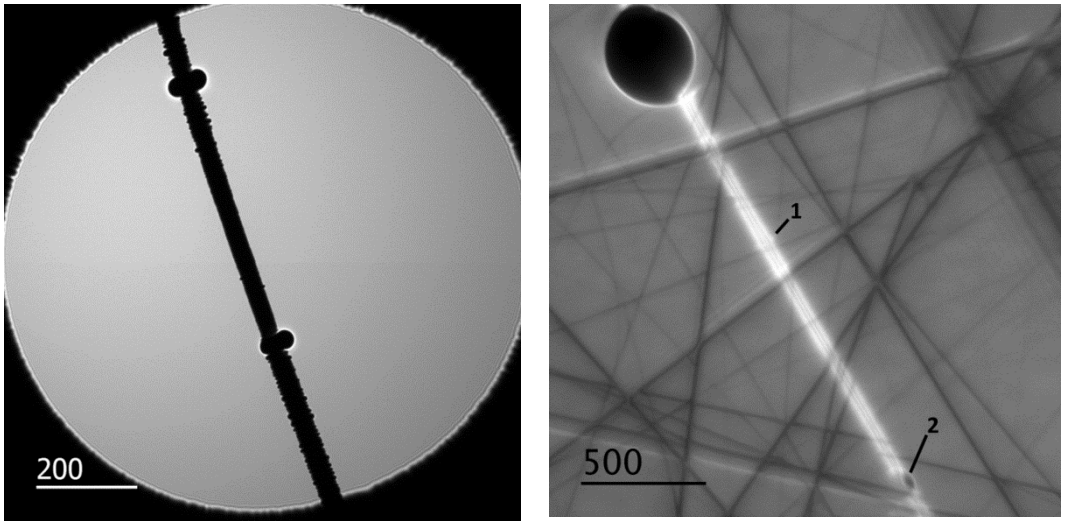

(a) (b)

Fig. 57- There are tiny particles attached to the biprism all along the wire, (a) the biprism image without the specimen. The area in the middle was always chosen to conduct the SIS-HOLZ. The particles in the DF disk are not observable, (b) the biprism with some voltages on. Except the big bulb on the top left side, two smaller particles, 1 and 2, are shown. These are not observable in the DF disk.

Chapter 5

Conclusion and Future Work

5.1 Conclusion

As long as the specimen thickness is $\leq \xi_g/\pi$, the kinematical theory of diffraction, Howie-Whelan equation, can be used to predict the phase profile across the split HOLZ line coming from a specimen with a non-uniform displacement field. Accordingly, the atomic displacement profile can be reconstructed by retrieving the phase profile across the split HOLZ line. The phase across the split HOLZ line was not measureable until the SIS-HOLZ method produced high contrast and high spatial frequency interference fringes of self-interfered split HOLZ line.

The principle steps of this method are listed as follow;

- Focusing the diffraction pattern.
- Tilting the specimen to find a major ZA. Move along a Kikuchi band to find a minor ZA or a less noisy region in the reciprocal space. If the specimen is highly tilted to travel inside the reciprocal space, refocusing the diffraction pattern will be required after each tilt.
- Finding a ROI. This can be done using the Kossel image (A. VIII). The region of interest is a strained area which in this work it was close to the interface of Si and $Si/Si_{0.8}Ge_{0.2}$ superlattices inside the Si substrate, Fig.32(b), below 400 nm and larger than 70 nm away from the interface.
- Adjusting the probe size to obtain high intensity sharp HOLZ lines. This also depends on the specimen thickness and the **g** reflection. In this work sharp and intense HOLZ lines were achieved in the specimen thickness below 200 nm. The best data was obtained for 008 HOLZ line at 166 nm thick.
- Moving towards or away from the ROI to check the 000 CBED HOLZ line split. Some HOLZ lines show no sensitivity to the atomic displacement, some disappear and some split asymmetrically.
- Picking a split HOLZ line and find its corresponding DF disk. To develop the experimental procedure comparing with the predicted phase profiles, in Chapter 3. Symmetric splits were in the area of interest.
- Calling and aligning the biprism. Rotating the biprism in the 000 CBED disk and making it parallel with the split HOLZ line. This step can preferably be done in

the image mode first. Then, some further biprism alignment will be required in the diffraction mode. Clean areas of the biprism must be used to conduct the experiment.

- Adjusting the biprism defocus until the biprism comes into focus. This defocuses the diffraction pattern somewhat. The purpose is to focus the biprism and the split HOLZ line on the same plane, Fig. 11.
- Centering the biprism in the split HOLZ line in the DF disk and interfering the split HOLZ line by varying the biprism voltage. Recording the interference patterns should be done using a GIF camera. Using an energy filter with a slit width of 10-20 eV helps removing the inelastic scattering of electrons which helps with the contrast of the fringes.
- Reconstructing the phase profile.
- Simulating the phase profile with predicted models of atomic displacement.
- Fitting the experimental profile with the corresponding simulated phase profile.
- Reconstructing the atomic displacement profile through the specimen thickness for the examined atomic plane.

The mentioned steps are the main steps in order to conduct the SIS-HOLZ method, although some detailed considerations are required to have high contrast fine fringes in order to minimize the phase noise to avoid misinterpreting the phase profile. The major investigated considerations can be reported as below;

- Specimen fabrication is a very crucial step. For this method some required features for a proper specimen are
  - ✓ Thin enough to obtain high intensity HOLZ lines. Below 171 nm showed the best results in this work, for 008. This depends on the examined **g** reflection.
  - ✓ Uniform thickness is preferable. By changing the thickness the focus condition varies which effects on the biprism defocus.
  - ✓ Ion milling the specimen after the FIB helps with removing the damaged layer in order to obtain a sharp and high intensity diffraction pattern.
- Recording the spot diffraction patterns at the ZAs, and the Kikuchi patterns at the major zone axis is required. This helps with indexing the HOLZ line which is

presented in appendix A. IX. It is required to know the orientation of the specimen with respect to the beam.

- Wider splits with higher intensity are always better to self-interfere. The wider split corresponds to a larger separation of the sources which gives finer fringes since higher voltage is required to shift the beams towards each other (at the same biprism defocus). This helps with filtering the side bands in the reconstruction steps. Also, higher intensity HOLZ lines give higher contrast fringes which decrease the phase noise. Wide split HOLZ lines can be achieved at closer distances to the ROI, however the intensity of the split decreases until they blur, i.e. at the interface and in the superlattices. Therefore, there is always a compromise between choosing a wide enough split and high intensity HOLZ line.
- Reconstruction step is very important. Filtering the side band affects significantly the phase profile. The right filter size is one third of the distance between the side band and the center band, Fig. 31.

- Recording the accurate knowledge of the thickness and the biprism defocus are very important in simulating the phase profile. K_B is the displacement of the interfering beams on the diffraction plane towards each other. The biprism angle of deflection is included in K_B which can be calculated using the fringe spacing. Recording the exact value of the bipirsm defocus significantly matters in the α_B calculation.
  - In the SIS-HOLZ method there is no reference wave but recording a reference hologram is suggested to compare with the SIS-HOLZ interferogram. This is helpful with interpreting the final phase image while comparing the biprism phase image.
  - Initial filtering of the interferogram helps with the background subtraction and denoising the interferogram. This step needs to be done with precaution to avoid producing artifacts, i.e. reducing the fringe contrast.

There are also limits in conducting the experiment or simulating the phase profile which some are reported as below.

- This technique is limited to the regions of interest. By approaching towards the Si and $Si/Si_{0.8}Ge_{0.2}$ superlattice interface, the split HOLZ lines lose their

intensity until they disappear. In this work the best data achieved above 70-120 nm away from the interface while the number of recorded electrons per pixel was $\approx 5 \times 10^3 - 5.5 \times 10^3$ e^-.

- Although R, t and $|\mathbf{g}|$ affect the phase profile, only the atomic displacement profile can change the shape of the phase profile. Hence, this technique needs an accurate mathematical model of the displacement field to predict the phase profile. Finite element method has been suggested to model the atomic displacement in the specimen. In this work the predicted models introduced by Hirsch et al. [20], Vincent et al. [24], Clement et al. [37], Saitoh et al. [42] and Alfonso et al. [43] are studied. In these works the models predict the displacement field at the interface of various lattice mismatched layers, mostly at the interface of Si and $Si/Si_{1-x}Ge_x$.
- This method is very microscope and specimen dependent. i.e., adjusting the biprism defocus, which is an important step, is very sensitive to the diffraction alignment, the power of the lenses and the specimen thickness. The specimen thickness also affects the quality of the diffraction pattern in terms of the intensity. Therefore some reported parameters such as the biprism defocus will be different in other microscopes.
- This method is a point to point measurement. Therefore, with one measurement a map of atomic displacement cannot be achieved. In order to obtain a displacement map, multiple measurements with equal increments is required. Extrapolation of further data points is suggested in order to compensate the constraint of conducting the experiment at a limited ROI.
- The method is very time consuming in terms of both experimental procedure and mathematical analysis, however it is still the first of its kind and insightful.
- Filtering the side band is a very crucial step. Choosing a proper split HOLZ line in terms of the split width and the split HOLZ line intensity effects on the phase noise and maximum spatial frequency. These two parameters are opposite so compromise is always required.

This work focus is on the phase reconstruction across the split HOLZ line in order to retrieve the atomic displacement field through the specimen thickness which is parallel to the electron beam direction. The focus of the work was two folds;

1- The development of an analytical routine to simulate the phase profile using the kinematical theory of diffraction.
2- The experimental methodology.

The SIS-HOLZ line is a novel technique with no predicted phase models across the split HOLZ lines. Thus, it is tried to reduce the number of variables which may effect on the phase profile, i.e. the specimen thickness effect, or the mathematical models of atomic displacement in semiconductor heterostructures, the composition and the crystalline planes. For thicker specimens the simulation needs to be corrected for dynamical scattering, however it highly depends on the index of the HOLZ line. Dynamical scattering effects on the HOLZ line position and intensity. The SIS-HOLZ gives a relative measurement of the phase profile. This means two sides of the split, S_1 and S_2, are interfered. There is no reference beam and the phase difference between S_1 and S_2 comes from the path length difference of the diffracted beam. S_1 and S_2come from the same atomic plane and same ROI. Therefore the composition variation has no effect on individual measurement. So, the path length difference is caused by the z-dependent atomic displacement profile and multiple scattering of the beam. However, since in SIS-HOLZ one **g** reflection is used to conduct each experiment, the multiple scattering effect can be cancelled out from S_1 and S_2 while they are interfered. Therefore, it is assumed that the multiple scattering effects will cause a phase shift to the total phase profile and will not effect on the shape of the profile. This may effect on interpreting the data and fitting the experimental and the simulated profiles with a less accurate R. Correcting multiple scattering effect in this technique especially for thicker specimens may help with developing the precision of the method.

Furthermore, the resolution of the electron holography methods such as DFEH are claimed equivalent to 3Δ, where Δ is the fringe spacing. The SIS-HOLZ method is a diffracted beam interferometry based method. So, the interference happens in the reciprocal space and the resolution of measurement in the unit of nm needs to be evaluated is a different way. However, the angular resolution can be calculated using the

fringe spacing. For the quantified data in Fig. 52 and Fig. 53, the angular resolution is 3.38×10^{-4} rad. Accordingly, the precision of the measurement with respect to the Bragg angle of 008 plane, $\Delta\theta/\theta_B$, in Si is $\approx 2.24 \times 10^{-3}$.

The reported sensitivity is for the experiment presented in this work. Before further development of the method, the resolution of the SIS-HOLZ technique is yet dependent on the carrier frequency of the fringes, $\Delta \propto 1/q_c$. In the diffracted beam interferometry, the fringe spacing varies with the separation of sources and the biprism defocus. Each parameter depends on the experimental condition such as the specimen thickness and the microscope. At this point an accurate measurement of the technique resolution and more experiment is still required.

This work has many potential for the future research and work, although some major future work are suggested for the further development of the SIS-HOLZ method.

5.2 Future Work

1. Dynamical diffraction correction in the simulation routine. Howie-Whelan is accurate enough for a two beam kinematical diffraction condition which requires the specimen thickness under ξ_g/π nm for the studied **g** reflection. For thicker specimens the effect of the multiple scattering needs to be taken into account.
2. Asymmetric split HOLZ lines coming from a uniformly thinned specimen may carry the asymmetric distribution of **R(**z**)** vector along the crystalline plane. This work focused on the symmetric profiles; however the asymmetric profiles need to be interpreted analytically as well. The asymmetric **R**(z) may contribute to the asymmetry of the phase profile.
3. In this work the **g** vector is considered parallel to the displacement vector, **R(**z**)**. In order to understand the effect of the angle between **g** and **R(**z**)**, the analytical routine expressed in Chapter 3 needs to be modified. Since the extra phase factor in the diffracted beam from an imperfect crystal is $\exp(-2\pi i \mathbf{g} \cdot \mathbf{R}(z))$, it is assumed that a shallow angle between **g** and **R**(z) causes a small phase shift to the whole profile. For deeper angles, the experiment is not feasible due to the small width of the split. The biprism defocus adjustment may help with this issue.

4. Measuring or developing a routine to estimate the spatial resolution and the precision of the SIS-HOLZ method.
5. The SIS-HOLZ can be applied to measure the burger vectors, **b**, and the displacement profile around the dislocations. In this study the displacement vector changes to $\mathbf{R} \propto \frac{\mathbf{b}}{2\pi}$.

Bibliography

[1] F. Hue, M. Hytch, H. Bender, F. Houdellier and A. Claverie, "Direct Mapping of Strain in a Strained Silicon Transistor by High-Resolution Electron Microscopy," *Physical review letters*, vol. 100, no. 15, p. 15602, 2008.

[2] J. Bardeen and W. Shockley, "Deformation Potentials and Mobilities in Non-Polar Crystals," *Physical Review*, vol. 80, no. 1, pp. 72-80, 1950.

[3] Y. Sun, S. Thompson and T. Nishida, "Physics of strain effects in semiconductors and metal-oxide-semiconductor field-effect transistors," *Journal of Applied Physics*, vol. 101, no. 10, p. 104503, 2007.

[4] E. Ungersboeck, S. Dhar, G. Karlowatz, V. Sverdlov, H. Kosina and S. Selberherr, "The Effect of General Strain on the Band Structure and Electron Mobility of Silicon," *IEEE Transactions on Electron Devices*, vol. 54, no. 9, pp. 2183-2190, 2007.

[5] K. Mistry, M. Armstrong, C. Auth, S. Cea, T. Coan, T. Ghani, T. Hoffmann, A. Murthy, J. Snadford, R. Shaheed, K. Zawadzki, S. Thompson and M. Bohr, "Delaying Forever: Uniaxial Strained Silicon Transistors in a 90nm CMOS Technology," in *Symposium on VLSI Technology* , Portlan,OR,USA, 2004.

[6] S. H. Oslen, A. G. O'Neil, P. Dobrosz, S. J. Bull, L. S. Driscoll, S. Chattopadhyay and K. S. Kwa, "Study of strain relaxation in Si/SiGe metal-oxide-semiconductor field-effect transistors," *Journal of Applied Physics*, vol. 97, no. 11, p. 114504, 2005.

[7] R. Xu, C. C. Chen, L. Wu, M. C. Scott, W. Theis, C. Ophus, B. Matthias, Y. Yang, H. R. Dakhel, M. R. Sawaya, H. Heinz, L. D. Marks, P. Ercius and J. M. Miao, "Three-dimensional coordinates of individual atoms in materials revealed by electron tomography," *Nature Materials*, vol. 14, no. 11, pp. 1099-1103, 2015.

[8] B. Goris, J. D. Beenhouwer, A. D. BAcker, D. Zanaga, K. J. Batenburg, A. S. Iglesias, L. M. Liz-Marzán, S. V. Aret, S. Bals, J. Sijbers and G. V. Tendeloo, "Measuring Lattice Strain in Three Dimensions through Electron Microscopy," *Nano Letters*, vol. 15, no. 10, p. 6996−7001, 2015.

[9] A. Beche, J. L. Rouviere, J. P. Barnes and D. Cooper, "Strain Measurement at the Nanoscale: Comparison between Convergent Beam Electron Diffraction, High Resolution Imaging and Dark Field Electron Holography," *Ultramicroscopy*, vol. 131, pp. 10-23, 2013.

[10] J. L. Rouviere and E. Sarigiannidou, "Theoretical Discussion on the Geometrical Phase Analysis," *Ultramicroscopy*, vol. 106, no. 1, pp. 1-17, 2005.

[11] C. H. Tung, "Atomic scale characterization for nanoelectronic devices," in *8th*

International Conference on Solid-State and Integrated Circuit Technology Proceedings, 2006.

[12] A. Beche, L. Clement and J. L. Rouviere, "Improved accuracy in nano beam electron diffraction," *Journal of Physics: Conference series* , vol. 209, p. 012063, 2010.

[13] A. Armigliato, S. Frabboni and G. C. Gazzadi, "Electron Diffraction with 10 nm Beam Size for Strain Analysis of Nanodevices," *Applied Physics Letters,* vol. 93, no. 16, pp. 161906(1-3), 2008.

[14] P. Favia, M. B. Gonzales, E. Simoen, P. Verheyen, D. Klenov and H. Bendera , "Nanobeam Diffraction: Technique Evaluation and Strain Measurement on Complementary Metal Oxide Semiconductor Devices," *Journal of The Electrochemical Society,* vol. 158, no. 4, pp. H438-H446, 2011.

[15] A. Beche, J. Rouviere and D. Cooper, "Dark Field Electron Holography for Strain Measurement," *Ultramicroscopy,* vol. 111, no. 3, pp. 2277-238, 2011.

[16] D. Cooper, J. P. Barnes, J. M. Hartmann, A. Beche and J. L. Rouviere, "Dark Field Electron HOlography for Quantitative Strain Measurements with Nanometer-scale Spatial Resolution," *Applied Physics Letters,* vol. 95, no. 5, p. 053501, 2009.

[17] G. Brunetti, E. Bouzy, J. J. Fundenberger, A. Morawiec and A. Tidu, "Determination of lattice parameters from multiple CBED patterns: A statistical approach," *Unltramicroscopy,* vol. 110, no. 4, pp. 269-277, 2010.

[18] T. Soeda, "Stress measuring method and system". United State Patent US 7,342,226 B2, 11 03 2008.

[19] D. B. Williams and C. B. Carter, Transmission Electron Microscopy, Newyork: Springer, 2009.

[20] P. B. Hirsch, A. Howie, R. B. Nicholson, D. W. Pashley and M. J. Whelan, Electron Microscopy of Thin Crystals, London: BUTTERWORTHS, 1965.

[21] K. K. Fung, "Converegent Beam Electron Diffraction study of transverese stacking fault and dislocations," *Ultramicroscopy,* vol. 17, no. 2, pp. 81-86, 1985.

[22] P. E. Champness, "Convergent Beam Electron Diffraction," *Mineralogical Magazine,* vol. 51, no. 359, pp. 33-48, 1987.

[23] K. Saitoh, H. Nakahara and N. Tanaka, "Improvement of the precision of lattice parameter determination by nano-beam electron diffraction," *Microscopy,* vol. 62, no. 5, pp. 533-539, 2013.

[24] R. Vincent, A. R. Preston and M. A. King, "Measurement of strain in silver halide particles by convergent beam electron diffraction," *Unltramicroscopy,* vol. 24, no. 4, pp. 409-420, 1988.

[25] D. Cherns, C. J. Kiely and A. R. Preston, "Electron diffraction studies of strain in epitaxial bicrystals and multilayers," *Ultramicroscopy,* vol. 24, no. 4, pp. 355-369,

1988.

[26] M. Vijayalakshmi, S. Saroja and R. Mythili, "Convergent beam electron diffraction –A novel technique for materials characterisation at sub-microscopic levels," *Sadhana,* vol. 28, no. 3-4, pp. 763-782, 2003.

[27] M. Norouzpour and R. Herring, "Aberration-corrected self-interference of split higher order Laue zone line for measuring the z-dependent strain profile," *Journal of Material Research,* vol. 32, no. 5, pp. 996-1008, 2017.

[28] J. M. Zuo, "Automated lattice parameter measurement from HOLZ lines and their use for the measurement of oxygen content in YBa2Cu3O7-δ from nanometer-sized region," *Ultramicroscopy,* vol. 41, no. 1-3, pp. 211-223, 1992.

[29] S. J. Rozeveld and J. Howe, "Determination of multiple lattice parameters from convergent-beam electron diffraction patterns," *Unltramiscroscopy,* vol. 50, no. 1, pp. 41-56, 1993.

[30] C. Deininger, G. Necker and J. Mayer, "Determination of structure factors, lattice strains and accelerating voltage by energy-filtered convergent beam electron diffraction," *Ultramicroscopy,* vol. 54, no. 1, pp. 15-30, 1994.

[31] R. Wittmann, C. Parzinger and D. Gerthsen, "Quantitative determination of lattice parameters from CBED patterns: accuracy and performance," *Ultramicroscopy,* vol. 70, no. 3, pp. 145-159, 1998.

[32] A. Toda, N. Ikarashi and H. Ono, "Local lattice strain measurements in semiconductor devices by using convergent-beam electron di!raction," *Journal of Crystal Growth,* vol. 210, no. q, pp. 314-345, 2000.

[33] S. Karmer, J. Mayer, C. Witt, A. Weickenmeier and M. Ruhle, "Analysis of local strain in aluminium interconnects by energy filtered CBED," *Ultramicroscopy,* vol. 81, no. 3, pp. 245-262, 2000.

[34] A. Armigliato, R. Balboni, S. Balboni, S. Frabboni, A. Tixier, G. P. Carnevale, P. Colpani, G. Pavia and A. Marmiroli, "TEM/CBED determination of strain in silicon-based submicrometric electronic devices," *Micron,* vol. 31, no. 3, pp. 203-209, 2000.

[35] A. Armigliato, R. Balboni, G. P. Carnevale, G. Pavia, D. Piccolo, S. Frabboni, A. Benedetti and A. G. Cullis, "Application of convergent beam electron diffraction to two-dimensional strain mapping in silicon devices," *Applied Physics Letter,* vol. 82, no. 13, pp. 2172-2174, 2003.

[36] A. Benedetti, H. Bender, C. Toregiani, M. Van Dal and K. Maex, "Nanometer scale characterisation of CoSi2 and NiSi induced strain in Si by convergent beam electron diffraction," *Materials Science and Engineering: B,* vol. 114, pp. 61-66, 2004.

[37] L. Clement, R. Pantel, L. F. Tz. Kwakman and J. L. Rouviere, "Strain measurements by convergent-beam electron diffraction: The importance of stress relaxation in lamella preparations," *Applied Physics Letters,* vol. 85, no. 4, pp. 651-653, 2004.

[38] A. Chuvilin, U. Kaiser, Q. Robillard and H. J. Engelmann, "On the origin of HOLZ lines splitting near interfaces: multislice simulation of CBED patterns," *Journal of Electron Microscopy,* vol. 54, no. 6, pp. 515-517, 2005.

[39] J. L. Rouvie, F. Houdellier, C. Roucau, L. Cle´ ment, J. Rouvie` re and M. Casanove, "Quantitative analysis of HOLZ line splitting in CBED patterns of epitaxially strained layera," *Ultramicroscopy,* vol. 106, no. 10, pp. 951-959, 2006.

[40] A. Benedetti, H. Bender and C. Torregiani, "On the Splitting of High Order Laue Zone Lines in CBED Analysis of Stress in Silicon," *Journal of The Electrochemical Society,* vol. 154, no. 3, pp. H217-H224, 2007.

[41] F. Houldellier, C. Roucau and M. J. Casanove, "Convergent beam electron diffraction for strain determination at the nanoscale," *Microelectronic Engineering,* vol. 84, no. 3, pp. 464-467, 2007.

[42] K. Saitoh, Y. Yasuda, M. Hamabe and N. Tanaka, "Automated characterization of bending and expansion of a lattice of a Si substrate near a SiGe/Si interface by using split HOLZ line patterns," *Journal of Electron Microscopy,* vol. 59, no. 5, pp. 367-378, 2010.

[43] C. Alfonso, L. Alexandre, C. Leroux, G. Jurczak, W. Sailkaly and A. Charai, "HOLZ lines splitting on SiGe/Si relaxed samples: Analytical solutions for the kinematical equation," *Ultramicroscopy,* vol. 110, no. 4, pp. 285-296, 2010.

[44] A. Spessot, R. Frabboni, R. Balboni and A. Armigliato, "Method for determination of the displacement field in patterned nanostructures by TEM/CBED analysis of split high-order Laue zone line profiles.," *Journal of Microscopy,* vol. 226, pp. 140-155, 2007.

[45] P. E. Midgley, "An introduction to off-axis electron holography," *Micron,* vol. 32, no. 2, pp. 167-184, 2001.

[46] A. Tonomura, Electron Holography, Berlin: Springer-Verlag, 1993.

[47] H. Lichte, P. Formanek, A. Lenk, M. Linck, C. Matzeck, H. Lehmann and P. Simon, "Electron Holography: Applications to Materials Questions," *Annual Review of Materials Research,* vol. 37, pp. 539-588, 2007.

[48] M. Hÿtch, F. Houdellier, F. Hüe and E. Snoeck, "Nanoscale holographic interferometry for strain measurements in electronic devices," *Nature,* vol. 453, no. 7198, pp. 1086-1089, 2008.

[49] V. V. Hoang, Y. Cho, J. H. Yoo, S. K. Hong, Y. H. Choi, S. Choi, W. Jung, C. K. Jeong and J. M. Yang, "Strain mapping in a nanoscale-triangular SiGe pattern by dark-field electron holography with medium magnification mode," *Microscopy,* pp. 1-9, 2016.

[50] D. Cooper, J. P. Barnes, J. M. Hartmann, A. Béché and J. L. Rouviere, "Dark field electron holography for quantitative strain measurements with nanometer-scale

spatial resolution," *Applied Physics Letters,* vol. 95, no. 5, p. 053501, 2009.

[51] A. Béché, J. L. Rouvière, J. P. Barnes and D. Cooper, "Dark field electron holography for strain measurement," *Ultramicroscopy,* vol. 111, no. 3, pp. 227-238, 2011.

[52] E. Javon, A. Lubk, R. Cours, S. Reboh, N. Cherkashin, F. Houdellier, C. Gatel and M. J. Hÿtch, "Dynamical effects in strain measurements by dark-field electron holography.," *Ultramicroscopy,* vol. 147, pp. 70-85, 2014.

[53] A. Lubk, E. Javon, N. Cherkashin, S. Reboh, C. Gatel and M. J. Hÿtch, "Dynamic scattering theory for dark-field electron holography of 3D strain fields.," *Ultramicroscopy,* vol. 136, pp. 42-49, 2014.

[54] R. Herring, M. Norouzpour, K. Saitoh, N. Tanaka and T. Tanji, "Determination of three-dimensional strain state in crystals using self-interfered split HOLZ lines," *Ultramicroscopy,* vol. 156, pp. 37-40, 2015.

[55] M. Norouzpour and M. Herring, "Strain Measurement through the Thickness of Crystal using DBI," *Microscopy and Microanalysis,* vol. 21, no. S3, pp. 1965-1966, 2015.

[56] R. Herring, G. Pozzi, T. Tanji and A. Tonomura, "Interferometry using convergent electron diffracted beams plus an electron biprism (CBED + EBI)," *Ultramicroscopy,* vol. 60, no. 1, pp. 153-169, 1995.

[57] E. Volkl , L. F. Allard and D. C. Joy, Introduction to Electron Holography, New York: Kluwer Academic/Plenum Publishers, 2013.

[58] R. Herring, "Electron beam coherence measurements using diffracted beam interferometry/holography.," *Journal of Electron Microscopy,* vol. 58, no. 3, pp. 213-221, 2009.

[59] R. Herring, "Energy-filtered diffracted beam holography," *Ultramicroscopy,* vol. 104, no. 3-4, pp. 261-270, 2005.

[60] R. Herring, "Planar diffracted-beam interferometry/holog raphy," *Ultramicrosopy,* vol. 108, no. 7, pp. 688-697, 2008.

[61] R. Herring, K. Saitoh, N. Tanaka and T. Tanji, "Coherent electron interference from amorphous TEM specimens.," *Microscopy,* vol. 61, no. 1, pp. 17-23, 2012.

[62] W. D. Deelman, L. F. Edge and C. A. Jackson, "Metamorphic materials for quantum computing," *MRS Bulletin,* vol. 41, no. 03, pp. 224-230, 2016.

[63] T. Yamazaki, A. Kashiwagi, K. Kuramochi, M. Ohtsuka, I. Hashimoto and K. Watanabe, "Quantitative and easy estimation of a crystal bending effect using low-order CBED patterns," *Journal of electron microscopy,* vol. 57, no. 6, pp. 181-187, 2008.

[64] M. Norouzpour, R. Herring and R. Rakhsha, "Self-interference of Split HOLZ Line

(SIS-HOLZ) for Measuring the Z-dependent Strain Profile: Theoretical Discussion," *Journal of Micron,* vol. 97, pp. 68-77, 2017.

[65] O. Matteucci, G. F. Missiroli and G. Pozzi, "Electron holography of long-range electrostatic fields," *Advances in Imaging and Electron Physics,* vol. 99, pp. 171-240, 1997.

[66] J. Li, T. Malis and S. Dionne, "Recent advances in FIB–TEM specimen preparation techniques," *Material Characterization,* vol. 57, no. 1, pp. 64-70, 2006.

[67] L. Alexandre, K. Rousseau, C. Alfonso, W. Saikaly, L. Fares, C. Grosjean and A. Charaı, "Optimized FIB silicon samples suitable for lattice parameters measurements by convergent beam electron diffraction," *Micron,* vol. 39, no. 3, pp. 294-301, 2008.

[68] J. C. H. Spence, High Resolution Electron Microscopy, United Kingdom: Oxford University Press, 2013.

[69] J. W. Edington, Electron diffraction in the electron microscope, London: The Macmillan Press LTD, 1975.

[70] R. Herring, G. Pozzi, T. Tanji and A. Tonomura, "Interferometry using convergent electron diffracted beams plus an electron biprism (cbed+ ebi)," *Ultramicroscopy,* vol. 60(1), pp. 153-169, 1995.

[71] P. B. Hirsch, A. Howie, R. B. Nicholson, D. Pashley and M. J. Whelan, Electron Microscopy of Thin Crystals, London: Butterworths, 1965.

[72] V. B. Ozdol, C. Gammer, X. G. Jin, P. Ercius, C. Ophus, J. Ciston and A. M. Minor, "Strain mapping at nanometer resolution using advanced nano-beam electron diffraction," *Applied Physics Letters,* vol. 106, no. 25, p. 253107, 2015.

Appendix

A. I- Ewald's Sphere

The Ewald's sphere is a geometric construct used in electron diffraction (or X-ray diffraction). It demonstrates the relationship between:

- The wave vector of the incident and the diffracted beam
- The diffraction angle for a given reflection
- The reciprocal lattice of the crystal

The reciprocal lattice is a three dimension array of points, each associate with a reciprocal lattice rod, relrod for short, which is centered on a point, C in Fig A. 1. Each point on the Ewald's sphere corresponds to an atomic plane in crystal.

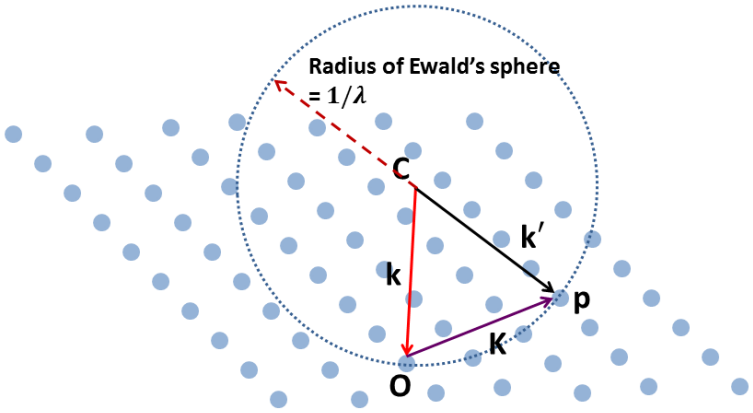

Fig A. 1- The Ewald's sphere of reflection intersecting a non-cubic array of reciprocal lattice points. Vector CO represents k, the wave vector of the incident beam. k′ is any radius vector. The radius of the Ewald sphere is inversely related to the electron wavelength **[20, 68]**.

This sphere is represented in two dimensions by a circle. The key point is that when the sphere cuts through the reciprocal lattice point the Bragg condition is satisfied and the corresponding maxima can be seen on the diffraction plane. If any point in the reciprocal lattice intersects the surface of the sphere, the sets of planes corresponding that point

must satisfy the Bragg equation and hence the planes will diffract strongly. The position of the spots changes while we tilt the specimen.

A. II- Kinematical and Dynamical Theory of Diffraction

In general, the analysis of the intensity of diffracted beams in TEM is not easy because a beam which is diffracted will be re-diffracted. This repeated diffraction is called "dynamical diffraction". Unlike dynamical theory of diffraction, in kinematical diffraction, there is no attenuation of the incident wave in the crystal so that the incident wave has the same amplitude at each scattering point. This is equivalent to neglecting any interaction between the incident wave in the crystal and the scattered waves. Each scattered wave travels through the crystal without being re-scattered by other scattering points. There is no absorption of either the incident or the scattered waves in the crystal.

As it is shown in Fig A. 2 dynamical diffraction depends on the thickness of the specimen. Φ_0 and Φ_g represent the amplitudes of the transmitted beam and the diffracted beam respectively. In two beam condition there is only one strong diffracted beam and other diffracted beams and scattered beams are so weak to effect on Φ_0 and Φ_g.

Thus, their contribution is ignored. At any given position in the specimen, the change in the amplitude (subsequently the intensity) of both, the direct beam and the diffracted beam, depends on the amplitude of both beams. Therefore, the math is quite straightforward. It comprises of only two equations to express the amplitude of the direct beam and the diffracted beam.

The Howie-Whelan equation is pair of equations, Eq. A.1, which say only $\boldsymbol{\Phi_0}$ **and** $\boldsymbol{\Phi_g}$ are dynamically coupled. Here 'dynamically" means only that the amplitudes of the diffracted beam and direct beam are constantly changing depend upon each other, which is dynamic **[19]**.

$$\frac{d\Phi_g}{dz} = \frac{\pi i}{\xi_g}\Phi_0 \exp(-2\pi i s z) + \frac{\pi i}{\xi_0}\Phi_g$$
$$\frac{d\Phi_0}{dz} = \frac{\pi i}{\xi_0}\Phi_0 + \frac{\pi i}{\xi_g}\Phi_g \exp(2\pi i s z) \qquad \text{A.1}$$

ξ_0 is a characteristic length for forward scattering, i.e., scattering from any beam into itself, while ξ_g corresponds to scattering through and angle corresponding a diffraction vector, **g**. The expression of the intensity of the diffracted beam while s=0 (exact Bragg condition) is very simple. It is expressed by "sinc" function [19].

$$|\Phi_g|^2 = \sin^2(\frac{\pi t}{\xi_g})$$
$$|\Phi_0|^2 = 1 - \sin^2(\frac{\pi t}{\xi_g}) \qquad \text{A.2}$$

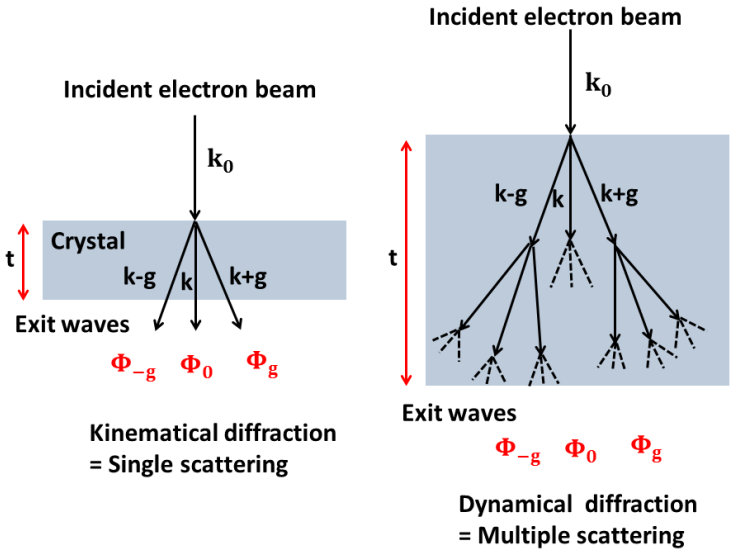

Fig A. 2- Kinematical diffraction corresponds to single scattering of electron while dynamical diffraction considers multiple scattering.

Unlike kinematical theory of diffraction, the dynamical diffraction is rather mathematical. In this theory, the exit wave s considered as the sum of all the beams passing through crystal. This theory is based on the periodic inner potential of crystal. Dynamical diffraction process in a periodic crystal can be fully described by Bloch waves. Bloch waves are generally different due to the different potential energy inside the periodic crystal. So they have different kinetic energy and wave vectors. In dynamical theory the exit wave is the sum of all the Bloch waves with different wave vectors. Bloch waves are explained fully in Ref. [19] the following references:

1. Aschfort, NW and Mermin, ND 1976 *Solid states physics* W.B. Saunders Co. Philadelphia PA. Chapter 8.
2. Howie, A1971 in Electron Microscopy in Materials Science 275-305 Ed. U Valdré Academic Press New York.

A. III – Structure Factor, F(θ)

This factor is introduced with term F_g in this work. f_θ is the measurement of the amplitude of an electron wave while it is scattered by a single atom and $|f_\theta|^2$ is proportional to the scattered intensity. f_θ highly depends on the electron wavelength, λ, the angle of scattering, θ, and the atomic number, Z. The structure factor $F(\theta)$ is the measure of the amplitude of the scattered beam from a unit cell of a crystal, instead of an isolated atom. So $F(\theta)$ can be defined as the sum of f_θ terms from all i individual atoms in the unit cell with atomic coordination of x_i, y_i, z_i multiplied by a phase factor. The phase factor takes into account of the phase difference between the scattered waves from atoms on different but parallel atomic planes with the same Miller indices (hkl). So the structure factor is [19];

$$F(\theta) = \sum_{i}^{\infty} f_i \exp(2\pi i(hx_i + ky_i + lz_i)) \qquad (A.3)$$

So the structure factor depends strongly on the type of atom, f_θ, the position of the atom, x_i, y_i, z_i in the cell (x, y, z) and the specific atomic plane (Miller index),(hkl).

A. IV – Selected Area Diffraction (SAD) versus Convergent Beam Electron Diffracted (CBED)

Generally, the objective lens in the TEM takes the electrons coming from the exit surface of the specimen and disperses them to create a DP on the BFP and recombines them to form an image on the image plane, Fig A. 3.

Hence, to see the DP we have to adjust the imaging system lenses so that the BFP of the objective lens acts as an object plane for the intermediate lens. Then the DP is projected onto the CCD camera or viewing screen as shown in Fig A. 4(A). In the diffraction mode the intermediate lens choose the BFP as its object.

To see the image instead of DP on the viewing screen, you need to readjust the intermediate lens so that it picks the image plane of the objective lens as its object. Then an image is projected onto the screen or a CCD camera. As it is shown the specimen is subjected to a parallel beam of electrons. The SAD pattern is made of sharp diffraction spots each corresponds to a crystalline lattice plane, (hkl).

In a basic principle of TEM operation when you want to look at SAD diffraction pattern, you put the SAD aperture into the image plane of the objective lens

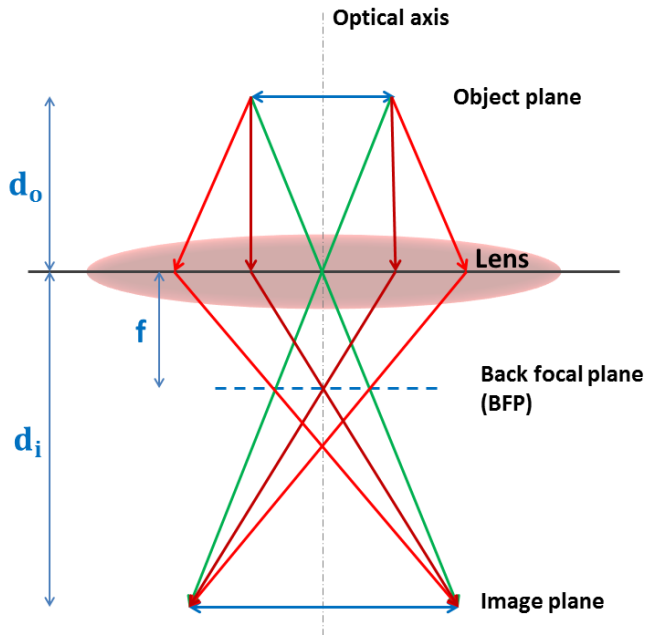

Fig A. 3- A ray diagram showing an object is symmetrically positioned around the optical axis. All rays from a point in the object at a distance $\mathbf{d_0}$ from the lens are gathered and converged by the lens on the image plane at distance **d** from the lens. All the parallel rays coming from the object are focused on the back focal plane (BFP) at distance **f** from the lens **[19]**.

SAD diffraction pattern is often displayed on the viewing screen at a fixed magnification so it is possible to recognize the difference in the magnitude of the g vectors. From a SAD diffraction pattern usually the crystalline symmetry, unit cell parameters, subsequently the crystal structure and the crystallographic orientation between two crystals. The diameter of electron beam impinges on the specimen in SAD

method is $1 - 10$ µm while in CBED technique instead the size of the incident electron beam easily goes to $1 - 100$ nm, in fact all the way down to a unit cell [19].

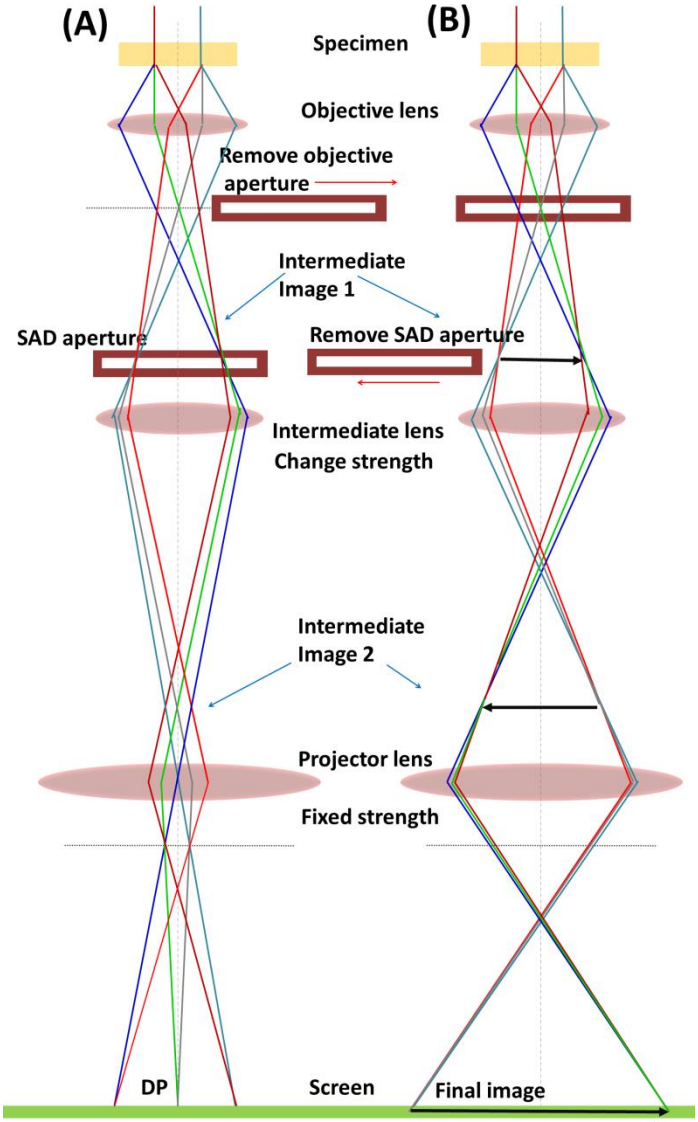

Fig A. 4- A simplified diagram showing two basic operations of TEM imaging system involves; the diffraction mode, at (A), and the imaging mode, at (B). The distance between the intermediate lens and the specimen is fixed **[19]**.

Thus, the spatial resolution of the measurement develops significantly, however there are two main drawbacks in CBED; generating contamination therefore localized stress due to the focused probe and heating or damaging the ROI. Unlike SAD, the convergent beam in CBED gives rise to a pattern of disks of intensity, Fig A. 5.

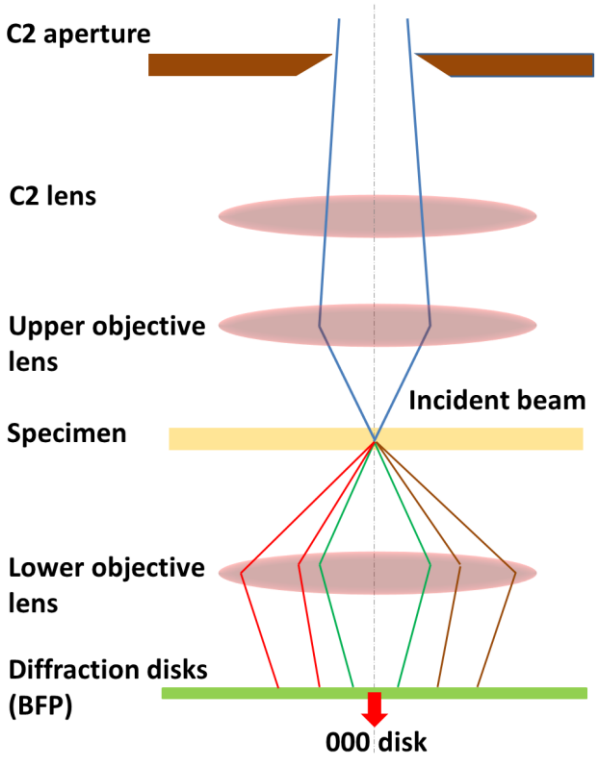

Fig A. 5- Ray diagram showing how a CBED pattern can form. The C2 aperture and lens aperture and the upper objective lens focuses the beam at the specimen therefore a very small area of the specimen is illuminated, compared with SAD parallel beam.

Since CBED patterns come from a rather small area of the specimen, you can certainly see high contrast details which cannot be taken by SAD.

A. V – Fraunhofer Diffraction and Fresnel Diffraction

Fraunhofer diffraction happens when a plane wave passes through an aperture causing only the size of the aperture image to change due to the far-field location of observation plane. Since a wave emitted by a point becomes planner at large distances, this diffraction is known as the far field diffraction. Unlike Fraunhofer diffraction, the Fresnel diffraction happens when a wave passes through an aperture and diffracts in the near field, causing any diffraction pattern observed differ in size and shape, depending on the distance between the aperture and the projection. When the distance is increased, outgoing diffracted waves become planar and Fraunhofer diffraction occurs.

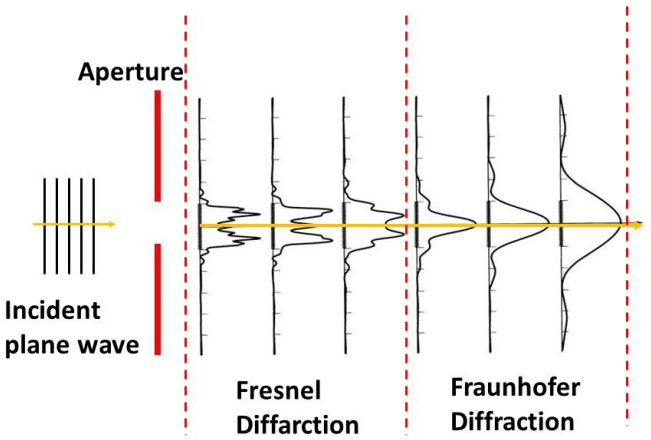

Fig A. 6– The intensity profiles in near field diffraction compared with far field diffraction intensity profiles.

In the Fraunhofer region the beam spreads to a width much greater than that of the aperture and the intensity profile looks like a Gaussian function, while in Fresnel region the beam width remains comparable with the aperture size with narrower fringes, Fig A. 6.

A. VI- Failed Specimens

Fig A. 7 shows two images of some failed specimens which were ion milled. The images were taken with Hitachi HF-3300V STEHM (Scanning Transmission Electron Holography Microscope). The failure in the specimen fabrication can be due to;

- The gallium beam instability or a poor beam alignment
- The specimen movement under the beam due to its poor attachment to the copper grid.
- Over ion milling the specimen.

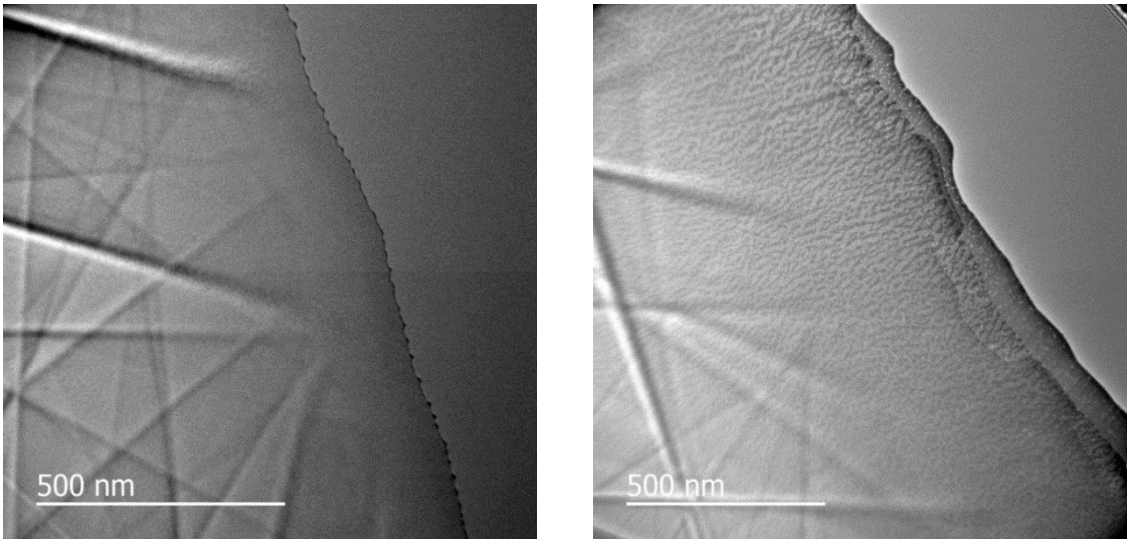

(a) (b)

Fig A. 7- (a) the superlattices, Si cap layer and the tungsten protective layer on the top surface of the specimen are totally milled, (b) the thickness variation and the surface contamination are observable.

As shown in Fig A. 7, HOLZ lines can be seen in the image mode as well. They are blurred closer to the surface of the specimen which can be due to thickness variation.

A. VII Mean Free Path

Electrons which lost energy in the specimen (inelastically scattered electrons) suffer a wavelength change and contribute to an out of focus background in the images. The overall effect of blurred background is to reduce the contrast of the electric image contrast. The contrast improvement results when the inelastic image contribution is removed from an image by an energy-selecting electron microscope. The inelastic background degrades the resolution. By energy filtering only the scattered electrons which lose little energy and are considered as elastically scattered electrons can be recorded leading to higher contrast and resolution images.

In crystals the inelastical scattering occurs owing to the processes of phonon excitation, plasmon excitation, and single-electron excitation. Since this phenomenon is very thickness dependent, by knowing the exact thickness of the specimen the intensity of the inelastic scattering can be computed. Mean free path, λ, is the average distance that

the electron travels between the scattering events. This distance is important because if we know it, we can find out how thin the specimen should be to ignore multiple scattering, making it easier to interpret the images and spectrums. Typical values of λ at TEM voltages are of the order of tens of nm. The inverse of the total cross section for scattering can be expressed as the mean free path.

$$\lambda = \frac{t}{p} = \frac{N_0 \sigma_{atom} (\rho t)}{A} \quad (A.4)$$

where p is the probability of scattering as the specimen travels through a specimen thickness t. There are computational resources to calculate mean free path at TEM voltages for various materials.

In Eq. 1 N_0 is Avogadro's number (n units of atoms mol^{-1}), A is the atomic weight of the scattering atoms in the specimen ($\mathrm{Kg\,mol}^{-1}$) which has density of ρ ($\mathrm{kg\,m}^{-3}$) [19, 68].

A. VIII- Kossel Pattern

There are 5 parameters you need to control while forming a CBED pattern.

- The angle of convergence, α
- The camera length, L
- The beam size (the probe diameter)
- The specimen thickness
- The focus of the pattern (under focus or over focus)

Depending on the angle of convergence the size of the diffraction disks vary as shown in Fig A. 8.

At small angles of α the patterns of non-overlapping disks is called Kossel-Molenstedt (K-M) pattern. By increasing the angle the disks start overlapping until at a very high angle of convergence which is called Kossel pattern. In this pattern the individual diffraction maxima are no longer discernible. Kossel patterns are very useful particularly at small camera length. Since, they display an extensive area of reciprocal space. A defocused image of the specimen also can be seen in the Kossel disks.

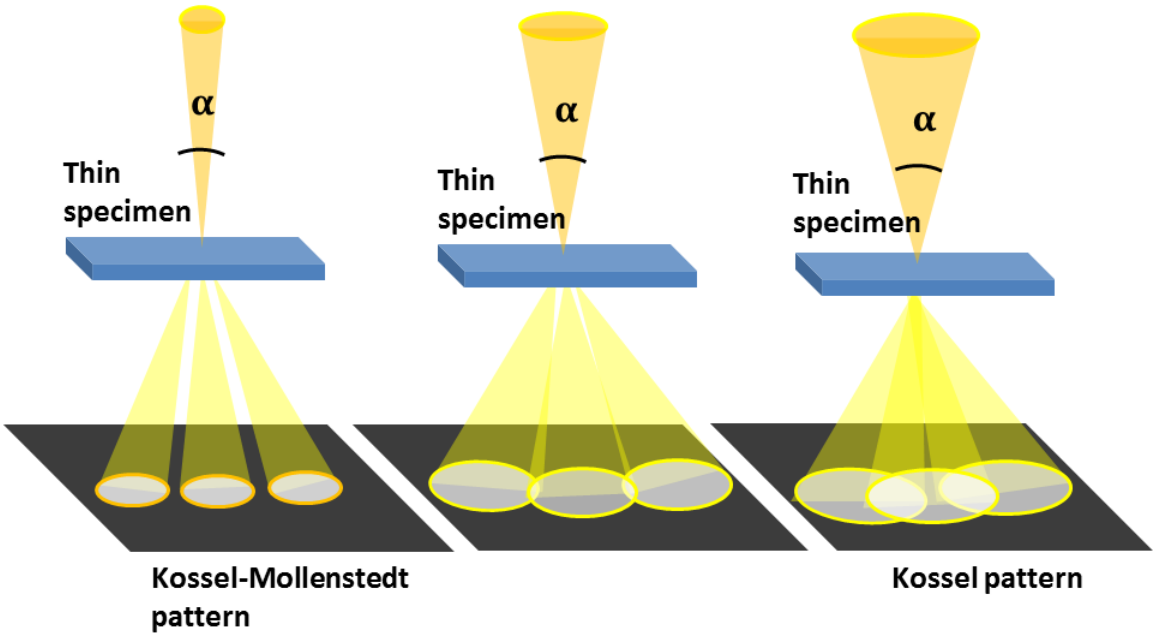

Fig A. 8- Ray diagrams showing how increasing the probe size causes CBED pattern to change from individual small disks (K-M pattern) into overlap disks (Kossel pattern) **[19]**.

A. IX- Indexing HOLZ line

In order to index HOLZ lines we need to know how to index single crystal DPs. There is a fundamental relationship in DPs which converts real space to reciprocal space **[20, 69]**;

$$RD = L\lambda \qquad (A.5)$$

where R is the distance between the direct beam and a specific diffraction beam, or simply it is the diameter of the diffraction ring. R is has the length unit and it is measured in the DP so the unit is nm. R is actually related to the spacing between atomic planes in the crystal, d. L is the camera length and λ is the wavelength of the accelerating voltage. Since Lλ is a constant factor for various values of R we will have;

$$R_1 d_1 = R_2 d_2 = R_3 d_3 = \cdots \qquad (A.6)$$

Only certain values of d associate with diffraction spots and if you know the lattice parameter of the crystal you can index the spot DPs. In order to index a HOLZ pattern, first you need to record a pattern with small L and small α to get the first order

Laue zone (FOLZ) pattern (Fig A. 9) and index it the same as it is explained above. FOLZ spots are HOLZ layers and each has an excess line in the central CBED disk. Each HOLZ line is perpendicular to its **g** vector coming from 000 CBED disk to the corresponding FOLZ reflection. Fig A. 9 shows FOLZ rings taken at 012 and 011 ZAs in Si substrate. As it is explained in Section 4.3.3 Kikuchi patterns and ZAs can help traveling through the reciprocal space. For instance Fig A. 10 shows 012 and 011 diffraction patterns in the stereographic triangle of a diamond cubic crystal (i.e. Si). In order to move from 012 to 011 ZAs more than 15° tilt is required. These patterns are taken from two different specimens since the maximum tilt in the accessible DT holder was 15°.

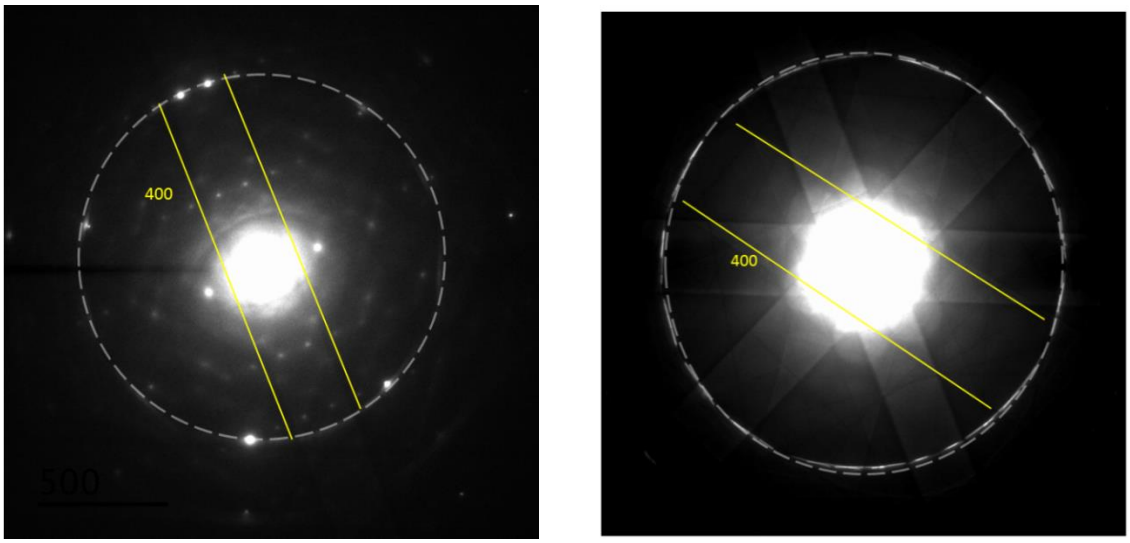

(a) (b)

Fig A. 9- FOLZ rings taken from Si substrate at, (a) 012 ZA, (b) 011 ZA

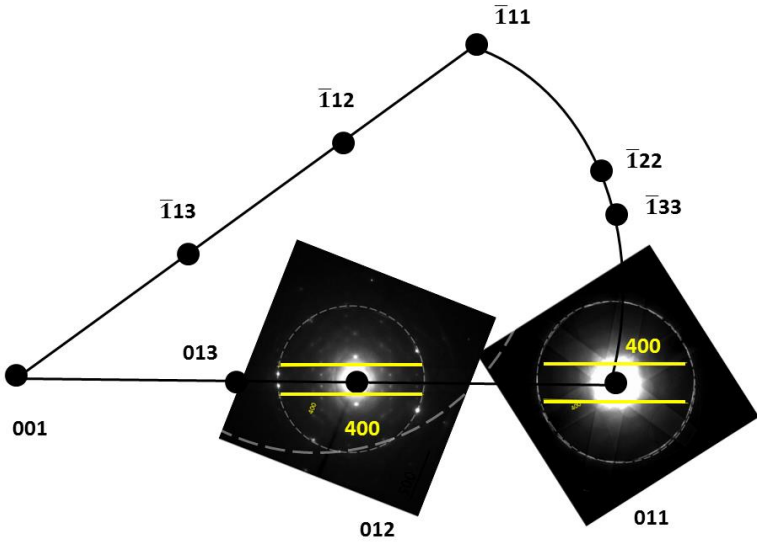

Fig A. 10- The stereographic triangle in a diamond cubic crystal showing how different ZAs can be connected to each other. The tilt from 012 to 011 ZA is ≅ **18° [69]**.

In Fig A. 11, the blue circles show the allowed FOLZ reflections intersected by Ewald sphere. These intensities can be seen as the FOLZ ring around the direct beam (the red circle) on the diffraction plane. By opening the probe or larger angle of convergence, α, and larger camera length, L, the direct beam can be seen as a big disk showing the HOLZ line i.e. A, B and C in figure below. Each HOLZ reflection on the FOLZ ring has its corresponding HOLZ in the direct beam. There should be a parallel deficient HOLZ line in FOLZ disk.

You may also see HOLZ lines coming from second order Laue zone (SOLZ) ring or even third- order Laue zone ring. These patterns are very high order lines and very sensitive to the lattice parameter change. Indexing HOLZ line is not as easy as explained and most of the time needs association of computer simulation for a direct indexing of HOLZ pattern.

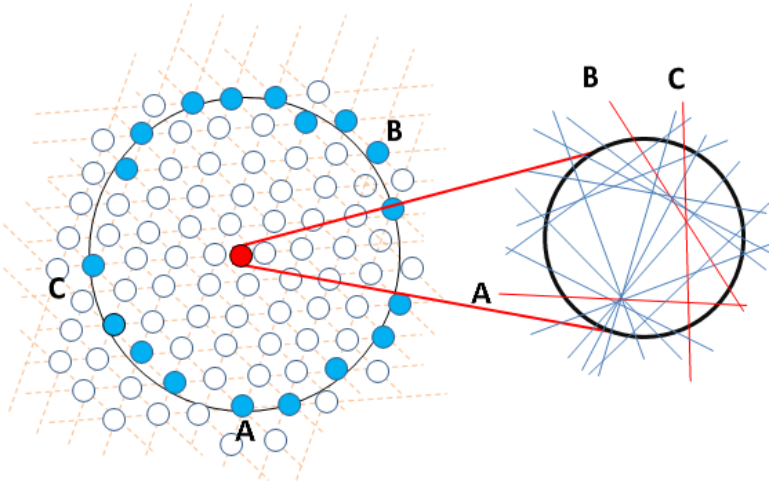

Fig A. 11- How to relate deficient HOLZ reflections on the FOLZ ring (i.e. A, B and C) to HOLZ maxima in 000 CBED disk. The filled blue spots show the allowed HOLZ reflections on the FOLZ ring **[19]**.